# UNSTEADY BIOMIXING AND HEAT TRANSFER IN MICROCHANNELS

By

**Peter Mueller**

A dissertation submitted in partial fulfillment of the

requirements for the degree of

Doctor of Philosophy

(Mathematics)

at the

**UNIVERSITY OF WISCONSIN – MADISON**

2016

Date of final oral examination: May 16, 2016

The dissertation is approved by the following members of the Final Oral Committee:

Jean-Luc Thiffeault, Professor, Mathematics

Saverio Spagnolie, Assistant Professor, Mathematics

Mike Graham, Professor, Chemical and Biological Engineering

Sam Stechmann, Associate Professor, Mathematics

Marko Budišić, Visiting Assistant Professor, Mathematics

# Abstract

We study the drift caused by time-dependent microswimmers, such as the microscopic algae *Chlamydomonas reinhardtii*, which swims by rapidly beating two frontal flagella. Previous studies of drift and transport by microswimmers have neglected the time-dependence of their swimming. We explore three different modeling choices including one that yields a persistent atmosphere in a time-dependent flow. We analyze individual particle paths and their displacements in a region around the swimmer. In our final model, the propulsion mechanism brings particles close to the swimmer's body while also reducing the resonance time near a no-slip surface. Comparing our results to a steady swimmer helps determine the importance of time-dependence. Later we switch topics to optimize the heat transfer in a microchannel. The geometry of a channel as well as the flow play crucial roles. We solve for the flow that minimizes the heat flux out of the channel, one way to measure the heat transfer.

# Acknowledgments

I would like to begin by expressing my deepest gratitude to my Ph.D. advisor, Jean-Luc Thiffeault. His years of patience, guidance, and support have gotten me out of his hair in five years. I am most impressed by his level of humility and his generosity to make extra appointments to work on coding together and have engaging discussions. I also thank Paulo Arratia, Marko Budišić, Mike Graham, Will Mitchell, and Saverio Spagnolie for their valuable discussions about research. I would like to acknowledge my advisor and the rest of my committee members: Saverio Spagnolie, Mike Graham, Sam Stechmann, and Marko Budišić who, together with my advisor, served as my thesis committee.

My experiences from undergrad have had a big impact on my career. Beginning with Duane Krueger (my chemistry lab instructor, golf partner, and close friend) whose guidance got me to where I am today. My first bosses, Peyton Owens III and Todd Helmer, who were two of the people in charge of the McNamara Academic Center for the University of Minnesota athletes. The workplace environment and tutoring their wonderful students served as a constant reminder of just how much I enjoyed tutoring and working with people, an activity I have continued throughout my years as a graduate student, which has greatly increased the amount of joy in my life. And last, but not least, my undergraduate mentor, Willard Miller, Jr., who first exposed me to the joys of mathematical research. I expand this section to include Amir Assadi for our engaging conversations on mathematical modeling as well as introducing me to the duties of inviting Willard as a speaker to Wisconsin.

I am indebted to my fellow graduate students for keeping me sane during graduate

school, including (but not limited to) the many entertaining outings with my cohort, beginning with our very first summer. As well as the Physical Applied Math seminar group for engaging talks, memorable laughs, valuable feedback, and tasty food at holiday parties.

I would like to extend my thanks to Mitsubishi Electric Research Laboratories for allowing me to experience life outside of academia, and the Midwest, for a summer. My supervisor, Piyush Grover, was very helpful along every step of the research process. I am also grateful for the engaging conversations had at our weekly social which was made possible by: Marissa Deegan (who also organized larger social outings, which was a big help to being in a new place), Elizabeth Philips (who handled the majority of the HR responsibilities), and Musau Dibinga (who handled the logistics of working at MERL). This opportunity helped finalize my decision to work in industry, and was made possible by Jean-Luc in numerous ways.

My graduate school attendance was supported by the University's Advanced Opportunities Fellowship, the Math Department's semesters of TA support, and the many semesters as Jean-Luc's RA, awarded by the Division of Mathematical Sciences of the US National Science Foundation (under grant DMS-1109315). I was able to survive graduate school thanks to the administrative and academic support from the 2nd Floor staff; and was able to thrive thanks to all of the computing help from both the department and the Center for High Throughput Computing (without whom I could not have gotten close to any of the intense numerical results we obtained).

Finally, I would like to thank my family and friends for their support throughout my life; most of all, my Mom, who is primarily responsible for my gifts and talents in life, except for my math skills which are from my older sister, Lara. My Dad for always

supporting me; my sister, Eva, with her many shared interests; and my sister, Rosa, who is probably the only person able to help fill the void left by our Mother's passing. My lifelong friend, Eric Heistad, for always being there for me. One of my closest friends, Keith Dsouza, who was sitting across the table from me at a coffee shop the moment this document entered existence. Our shared idea to work together on a regular basis has allowed me to make actual progress on this document. Uri Andrews, whose friendly debates and racquetball games kept me challenged and allowed us both an escape from our math-filled lives. I am also grateful for the love and encouragement of my girlfriend, Jentina, who is responsible for this document existing much earlier than it would have otherwise.

# Contents

# List of Figures

# List of Tables

# Chapter 1

# Introduction and Background

Most microorganisms depend on a well-mixed environment for their supply of nutrients. The nutrients typically have very slow rates of diffusion, so some amount of mechanical stirring is needed to enhance mixing. This stirring is often caused by external factors such as winds, tides, or gravity waves in the ocean, or circulation in blood vessels. However, the motion of the organisms themselves can assist this process. The stirring and mixing of an environment caused by swimming organisms is called *biogenic mixing*, or *biomixing* for short.

Biomixing has been investigated for several years with the aid of experimental observations [31, 36, 37, 39, 40, 42, 47, 55] as well as theoretical models and numerical simulations [30, 38, 43, 46, 67, 78, 83]. The importance of biomixing remains unclear in relation to mixing caused by winds, waves, molecular diffusion, and other factors [10, 13, 23, 28, 66, 72, 76, 79]. It is thus important to understand the detailed manner in which biomixing arises in order to gauge its possible impact.

At higher Reynolds numbers (when inertial effects are comparably larger than viscous dampening), mixing can be assisted by turbulence [47] or the ability to transport momentum. Microscopic swimmers (or microswimmers) normally have very small Reynolds numbers. In this regime (known as Stokes flow), viscous dissipation dominates over inertial effects. Additionally, the Scallop theorem [60] applies at small Reynolds numbers;

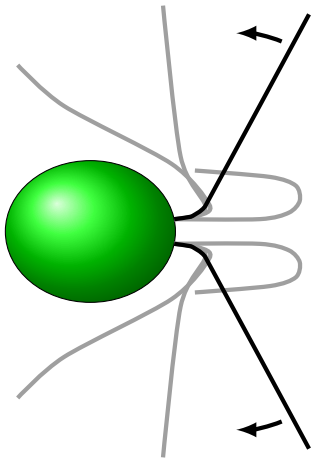

Figure 1: Diagram of *C. reinhardtii*, with a pair of oscillating, anterior flagella.

thus locomotion requires a more tailored approach in the Stokes regime. In this regime, microswimmers produce long-range velocity fields as they move, which allows tracers or nutrients to diffuse more rapidly. This is amplified by the abundance of microorganisms in bodies of water.

Microswimmers are generally grouped into two categories — pushers and pullers — based on the positioning of their propulsion mechanism. *Escherichia coli* (a pusher) has a rotating helical filament located on its posterior end, while *Chlamydomonas reinhardtii* (or *C. reinhardtii* for short, a puller) has a pair of anterior flagella that move similar to that of a breast-stroke (see Fig. 1). At high volume fractions of swimmers, pushers align with each other creating mixing effects at larger scales [6, 14, 26, 50, 68, 69, 70, 71, 77]. Additionally, the same dynamics that cause the alignment of pushers, also lead to attractions with surfaces as seen in [4, 9, 15, 41, 65, 81]. Pullers, on the other hand, do not align side-by-side and thus high densities of pullers are less interesting.

Recent experiments have shown enhanced tracer diffusion at low volume fractions

for pushers, pullers, and self-propelled particles [31, 40, 42, 51, 52, 71, 82]. Both simulations and theoretical arguments [30, 46, 63, 67, 78, 83] support this finding. Particles often trace out loop-like trajectories when a swimmer moves by (resulting in reduced net-displacements). These trajectories can be broken by stagnation points near the swimmer [46] and finite swimming paths [63, 76]. Some microorganisms exhibit run-and-tumble behavior to break up infinite paths; for example, *E. coli* does this to traverse biochemical gradients. Other swimmers experience rotational diffusion or other environmental effects.

In order to explain enhanced tracer diffusion, the *drift* caused by a swimmer must be analyzed [11, 17, 45, 49, 63]. Katija and Dabiri [37] and Thiffeault and Childress [76] proposed that the enhanced diffusivity is the result of each fluid particle interacting with many swimmers, and thus experiencing multiple drifts. Leptos et al. [42] highlight that the unsteadiness of the flow contributes to the complex dynamics.

The vast majority of papers on swimmer suspensions use flows that are steady in the frame of the swimmers to simplify the problem. This paper explores the effect of time-dependence on the displacement of tracer particles. We use the probabilistic model formulated by Thiffeault and Childress [76] and Lin et al. [46] to analyze the fluid transport of an unsteady swimmer. This model has been recently tested in numerical simulations [35, 53] and shown to hold in more complex setups [61, 62].

**Thesis Overview**

In the remainder of Chapter 1, we define some terminology and describe previous results and models used to study biomixing.

Chapter 2 focuses on some of our earlier swimmer modeling choices and preliminary results. One of our goals is to determine how important time-dependence is to biomixing.

We make sure to include time-dependence as a constant facet throughout our model variations. One model in particular creates a fictitious *atmosphere*, a volume of fluid that follows the swimmer around. The main benefit of an atmosphere is it transports particles, within it, much further than particles outside of it; thus, not only increasing fluid transport, but also separating regions of particles, increasing mixing.

In Chapter 3 we discuss our ultimate model choice and share our main results. Our final model accurately represents the boundary conditions of the swimmer's body (no-slip surface) while simplifying the propulsion mechanism to make our model axially symmetric. We analyze the results of numerical simulations, including: particle paths and displacements.

Then we enlist some asymptotic techniques to address the dynamical limits near and far from the swimmer in Chapter 4. Nearby we analyze the interactions between particles, the swimmer's body, and the flagella. While far away, the time-dependence becomes much less important.

Chapter 5 combines the results from the first few chapters in order to address the distribution of particle displacements and other measurements of mixing.

We switch gears for Chapter 6 to talk about some separate work done as an intern at Mitsubishi Electric Research Laboratories with Dr. Grover. The focus of this work is to optimize the heat transfer within curved microchannels. One application of this research could be to cool off computer processors by pumping liquid coolant through microchannels near areas of intense heat.

Lastly, in Chapter 7 we discuss some of our results and mention some possible options for future work.

## 1.1 Terminology

Here we explain some of the more frequently used terms and definitions throughout this document, beginning with the chapters on biomixing and ending with heat transfer.

### 1.1.1 Stokes Flow

The classic Navier-Stokes equations are derived from conservation of mass and momentum arguments. These equations are often non-dimensionalized in the following manner:

$$\mathrm{Re}\left(\mathrm{St}^{-1}\boldsymbol{u}_t + \boldsymbol{u}\cdot\nabla\boldsymbol{u}\right) = -\nabla p + \mu\nabla^2\boldsymbol{u},$$

where the Reynolds and Strouhal numbers are

$$\mathrm{Re} = \frac{\rho RU}{\mu}\,, \qquad \mathrm{St} = \frac{TU}{R}\,,$$

respectively. Here $R$ is the radius of the swimmer (a length scale), $U$ is the swimmer's mean swimming speed (a velocity scale), and $T$ is the period of swimming oscillations (a time scale). For small Reynolds numbers and moderate Strouhal numbers, the Stokes equations

$$-\nabla p + \mu\nabla^2\boldsymbol{u} = 0$$

serve as a good approximation to the fluid dynamics.

#### Scallop Theorem

The Stokes equations are invariant under time-reversibility. This yields many interesting results such as: a pair of sedimenting particles will not drift apart or come together, and a scallop in Stokes flow will not make forward progress. The latter is referred to as the

Scallop Theorem, [60]. When a scallop closes its mouth, it is propelled in the opposite direction; during the opening of its mouth, it reverts back to its original position due to this reversibility condition (a key reason that scallops are not found swimming at low Reynolds numbers).

This reversibility poses a challenge for microscopic swimmers (microswimmers) which is overcome either by a swimming stroke, consisting of a non-symmetric power and recovery portion (such as *C. reinhardtii*, which we study in this paper), or some other symmetry breaking behavior (such as the rotational chirality in *E. coli*'s flagella). The power stroke refers to the period when the swimmer makes the most forward progress and the recovery stroke is necessary to reset the swimmer's propulsion mechanism, sometimes causing backtracking. This "inefficiency" of forward movement followed by backward movement is often necessary to overcome the Scallop Theorem.

**Singularities of Stokes Flow**

Lots of swimmer models are created using singular solutions to the Stokes equations. The two main building blocks are the Stokeslet and the source dipole, where the Stokeslet is derived from a delta forcing term,

$$-\nabla p + \mu \nabla^2 \boldsymbol{u} = -\boldsymbol{f}\, \delta(\boldsymbol{r}), \qquad \nabla \cdot \boldsymbol{u} = 0,$$

and the source dipole is the limit of a source and sink term approaching each other with the source/sink being derived from

$$-\nabla p + \mu \nabla^2 \boldsymbol{u} = 0, \qquad \nabla \cdot \boldsymbol{u} = M\, \delta(\boldsymbol{r}).$$

For example, the flow field of a translating rigid sphere consists of an ambient flow, a source dipole, and a Stokeslet, with the two singularities being located at the center of

the sphere.

**Faxén's Law**

Faxén's Law [19] allows one to compute the velocity of a sphere due to external forces and velocity fields or to compute the force on the sphere due to its velocity and external velocity fields:

$$\boldsymbol{F} = 6\pi\mu R\left[\left(1+\tfrac{1}{6}R^2\nabla^2\right)\boldsymbol{u}(\boldsymbol{r})\big|_{\boldsymbol{r}=\boldsymbol{r}_0} - (\boldsymbol{U}-\boldsymbol{u}^\infty)\right],$$

where $\boldsymbol{F}$ is the force on the sphere, $\mu$ is the dynamic viscosity of the fluid, $R$ is the radius of the sphere, $\boldsymbol{u}$ is the external velocity field, $\boldsymbol{r}_0$ is the center of the sphere, $\boldsymbol{U}$ is the velocity of the sphere, and $\boldsymbol{u}^\infty$ is the ambient background flow. We use this in Chapter 3 when we model the swimmer's body by a rigid sphere.

### 1.1.2 Fluid Transport

Here we brush up on some common terms used to quantify fluid transport or mixing.

**Forms of Drift**

Stokes drift is the act of fluid particles being displaced by wave motion. Darwin drift, which we focus on in our research, deals with fluid particles being advected by a passing swimmer [11, 45, 49]. Within each of these categories, some people study Lagrangian drift, which computes particle displacements by following individual particles in the fluid (this requires integration of particle paths which we do for the bulk of the fluid). Others study the Eulerian drift which computes displacements by integrating the velocity field at a fixed point. The former is often more complicated while the latter fails to capture

spatial dependence, but can still capture time-dependence of the flow. We use Eulerian drift for particles very far from the swimmer where the velocity field remains fairly constant in space.

### Atmosphere

The term "atmosphere" in fluid dynamics refers to a volume of fluid that follows a swimmer around and seems to have gotten its name from the atmosphere that follows Earth around as we orbit the sun. Atmospheres are most easily found in steady flows, but can persist through varying levels of time-dependence [64]. They can be detected by use of Poincaré maps or lobe dynamics. Lobe dynamics involve complex interactions between stable and unstable manifolds of the fluid. These manifolds serve as boundaries of the fluid and thus can isolate regions of particles from other regions, sometimes referred to as lobes. These lobes can often stretch, fold, and intersect with each other over time, enhancing mixing. Additionally, fluid particles trapped within atmospheres can be transported large distances.

### Effective Diffusivity

As particles are displaced by a swimmer, they can be thought of as diffusing out into the fluid. An effective diffusivity can be computed in a similar manner to the thermal diffusion caused by Brownian motion, using the second moment of particle displacements:

$$2d\kappa t = \langle \Delta^2 \rangle,$$

where $d$ is the dimension of the system, $\kappa$ is the diffusivity of the particles (referred to as an enhanced diffusivity when purely looking at particle advection or as effective

diffusivity when incorporating thermal noise), and $\langle \cdot \rangle$ is an ensemble averaging.

## 1.2 Microchannel Flows

Depending on the channel geometry or the flow rate, fluid can behave and develop differently down the channel. The following terms vary slightly throughout the literature, but for the most part are defined as follows. In the simplest case, the flow is called steady if there is only spatial dependence of the velocity field and no time-dependence. Nearly identical is the condition referred to as "fully-developed" flow in which there is usually no time-dependence, but the only constraint is that the velocity field has matured from the initial conditions (either a flow starting at rest or differential geometry near the channel's inlet). To clarify, most simulations neglect the first portion of the channel as they are usually manufactured with a section of straight pipe to allow different inlet conditions, and then the more complex geometries enter in. This initial region is often called the "transition region" and afterwards we have fully-developed flow. Other terms such as "transient" or "turbulent" flows refer to increasing levels of complexity or time-dependence, which we will not deal with as we focus on laminar flows in Chapter 6.

# Chapter 2

# Unsteady Stokeslet Models of a Microswimmer

*C. reinhardtii* has a near-spherical body and a pair of anterior flagella that it uses for locomotion (see Fig. 1). *C. reinhardtii*'s size (4 $\mu$m radius) and speed (100 $\mu$m/s) give a Reynolds number of about $4 \times 10^{-4}$ in water. The asymmetric motion of its flagella enables it to swim in the Stokes regime. Even with a large swimming stroke frequency of 50 Hz, the steady Stokes equations serve as a good approximation to the fluid dynamics.

In this chapter we walk through some of our preliminary swimming model choices and the results they produced. We begin with a three-Stokeslet model, similar to the three sphere model used in Friedrich and Jülicher [21]. Later we reduce this model down to two Stokeslets in order to make our swimmer axially symmetric. Axial symmetry allows us to reduce the dimensionality of our swimmer, and thus also its surroundings, down from three to two. This makes gathering results, such as displacements of particles located anywhere in space, much easier.

## 2.1 The Three-Stokeslet Swimmer

In the work of Friedrich and Jülicher [21], *C. reinhardtii*'s flagella are modeled by a pair of spheres that move in counter-rotating circular paths; the body of the organism is represented by a third sphere. The authors find that spheres of constant size, moving at a constant angular velocity, produce a net forward movement due to the difference in hydrodynamic interactions during the power and recovery strokes. Additionally, they find that the spheres will synchronize if out of phase purely based on hydrodynamic effects (before this paper, it was unclear if this was only possible due to some inner workings of the organism). Our first model borrows from this three sphere idea.

### 2.1.1 Model Formulation

The experimental results of Leptos et al. [42] were the original motivation for our research as well as many others. Their results show enhanced diffusivity of tracer particles and suggest that this may be caused the unsteadiness of the swimming behavior. Additionally, Drescher et al. [16] reveals the similarity between the actual flow model of *C. reinhardtii* and a three-Stokeslet representation of the swimmer (one for each flagellum and one for the swimmer's body). We combined these ideas, along with [21], to create a time-dependent model involving three Stokeslets with the two representing the flagella moving in counter-rotating elliptical paths (these Stokeslets are represented as spheres in Fig. 2 for visual clarity).

The first consequence of using Stokeslets instead of spheres (as in [21]) is that our swimmer no longer makes natural forward progress, since the hydrodynamic interactions between spheres does not translate well (if at all) to singularities. We overcome this by

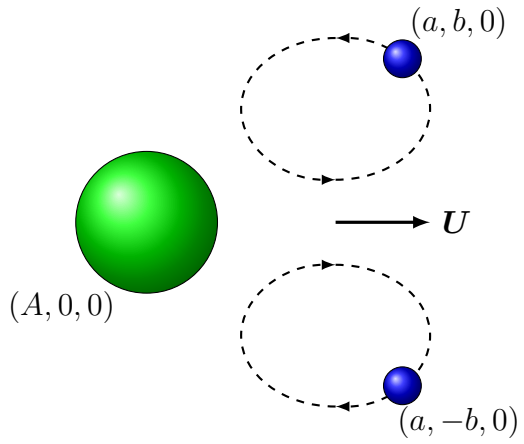


Figure 2: The three-Stokeslet swimmer model representative of *C. reinhardtii*. The smaller, counter-rotating spheres take the place of the anterior flagella.

adding time-dependence to the strengths of the Stokeslets. This is also representative of the changing shape of the actual flagella during *C. reinhardtii*'s swimming stroke. The strength of the flagellar Stokeslets are largest during the power stroke (when the flagella are most outstretched) and smallest during the recovery stroke (when the flagella are brought closer to the body). Up next we see that these power/recovery stroke dynamics completely determine the swimming speed of our swimmer model.

We orient the swimmer along the $x$-axis and place a Stokeslet (with strength $F = \|\boldsymbol{F}\|$) representing the body of the swimmer at $(A, 0, 0)$ and two symmetric flagellar Stokeslets (with strength $f = \|\boldsymbol{f}_{\pm}\|$) off the $x$ axis with centers at $(a, \pm b, 0)$. The resultant velocity field of our three-Stokeslet model is

$$\boldsymbol{u}(\boldsymbol{r}) = \boldsymbol{F} \cdot \mathbb{G}(\boldsymbol{r} - A\,\hat{\boldsymbol{x}}) + \boldsymbol{f}_{+} \cdot \mathbb{G}(\boldsymbol{r} - a\,\hat{\boldsymbol{x}} - b\,\hat{\boldsymbol{y}}) + \boldsymbol{f}_{-} \cdot \mathbb{G}(\boldsymbol{r} - a\,\hat{\boldsymbol{x}} + b\,\hat{\boldsymbol{y}}). \tag{2.1}$$

Recall $\mathbb{G}(\boldsymbol{r})$ is the Oseen tensor,

$$\mathbb{G}(\boldsymbol{r}) = \frac{1}{8\pi\mu\|\boldsymbol{r}\|}\left(\mathbb{I} + \frac{\boldsymbol{r}\,\boldsymbol{r}}{\|\boldsymbol{r}\|^2}\right),$$

with $\boldsymbol{u}_0 = \boldsymbol{f}_0 \cdot \mathbb{G}(\boldsymbol{r})$ satisfying the modified Stokes equation:

$$-\nabla p + \mu \nabla^2 \boldsymbol{u}_0 = -\boldsymbol{f}_0 \delta(\boldsymbol{r}), \qquad \nabla \cdot \boldsymbol{u}_0 = 0.$$

*C. reinhardtii* is (practically) neutrally buoyant so we impose force balance on our swimmer:

$$F + 2f_x = 0, \tag{2.2}$$

where $\boldsymbol{f}_\pm \coloneqq f_x \hat{\boldsymbol{x}} \pm f_y \hat{\boldsymbol{y}}$ and the $y$-component is satisfied by symmetry.

Now consider our three-Stokeslet swimmer in a frame moving at constant velocity $U\hat{\boldsymbol{x}}$, so there is an apparent flow $-U\hat{\boldsymbol{x}}$, where $U$ is the mean swimming speed. While we choose not to use spheres, as in [21], it may be helpful to relate the strengths of the Stokeslets to the drag coefficient of a sphere in Stokes flow [3]. We define $R$ as the radius of the swimmer's body and $r(t)$ as the effective radius of the flagellar Stokeslets, this yields

$$\boldsymbol{F}(t) = 6\pi\mu R(U + \dot{A}(t))\hat{\boldsymbol{x}}, \qquad \boldsymbol{f}_\pm(t) = 6\pi\mu\, r(t)((U + \dot{a}(t))\hat{\boldsymbol{x}} \pm \dot{b}(t)\hat{\boldsymbol{y}}), \tag{2.3}$$

where the dot represents a derivative with respect to time. The swimmer should not drift out of the comoving frame which results in the following constraints:

$$\langle \dot{A} \rangle = \langle \dot{a} \rangle = 0, \qquad \langle \dot{b} \rangle = 0, \tag{2.4}$$

where $\langle \cdot \rangle$ denotes the average over a time period $\tau = 2\pi/\Omega$. From (2.2) and (2.3), we have

$$R(U + \dot{A}(t)) = -2r(t)(U + \dot{a}(t)), \tag{2.5}$$

which upon time-averaging and using (2.4) gives

$$RU = -2U\langle r \rangle - 2\langle r\dot{a} \rangle.$$

Thus the mean swimming velocity is

$$U = -2\langle r\dot{a}\rangle/(R + 2\langle r\rangle). \tag{2.6}$$

The prescribed functions are $\dot{a}(t)$ and $r(t)$; $U$ is then obtained from (2.6) and $\dot{A}(t)$ from (2.5). Correlations between $\dot{a}(t)$ and $r(t)$ are entirely responsible for the swimmer moving forward.

The simplest time-dependence we can put is to have the flagella move harmonically along elliptical paths:

$$a(t) = a_0 + a_1 \cos \Omega t, \qquad b(t) = b_0 + b_1 \sin \Omega t, \qquad r(t) = r_0 + r_1 \sin(\Omega t + \phi),$$

which gives the mean swimming velocity

$$U = \frac{\Omega\, a_1 r_1 \cos\phi}{R + 2r_0}.$$

The phase $\phi = 0$ yields the fastest mean swimming velocity: it corresponds to the flagellar Stokeslet being strongest during the power stroke, and weakest in the recovery stroke. We thus set $\phi = 0$ for simplicity and obtain

$$\begin{aligned}\dot{A}(t) &= -U - 2r(t)(U + \dot{a}(t))/R \\ &= \frac{\Omega\, a_1 r_1}{R}\left\{2\left(\frac{r_0}{r_1} - \frac{r_1}{R + 2r_0}\right)\sin \Omega t - \cos 2\Omega t\right\}\end{aligned}$$

from (2.5), which can be integrated to find $A(t) = \int^t \dot{A}\,\mathrm{d}t$. We choose the integration constant such that $\langle A\rangle = 0$, so that the swimmer's body oscillates about the origin in the comoving frame:

$$A(t) = -\frac{a_1 r_1}{2R}\left\{4\left(\frac{r_0}{r_1} - \frac{r_1}{R + 2r_0}\right)\cos \Omega t + \sin 2\Omega t\right\}.$$

The flow field of our model is then fully determined by picking a set of parameters for: $a_0, a_1, b_0, b_1, r_0, r_1, \Omega$. Before running any numerics we derive a far-field approximation of our flow field.

### 2.1.2 Far-Field Velocity

Zooming out from our swimmer has the same behavior as taking the limit of three Stokeslets approaching each other (which is what a far away particle sees). Because of (2.2), the far-field form of (2.1) is

$$\boldsymbol{u}(\boldsymbol{r},t) \sim ((a-A)F\,\hat{\boldsymbol{x}}\hat{\boldsymbol{x}} - 2bf_y\,\hat{\boldsymbol{y}}\hat{\boldsymbol{y}}) : \mathbb{S}(\boldsymbol{r}), \qquad \|\boldsymbol{r}\| \to \infty, \tag{2.7}$$

where $\mathbb{S}(\boldsymbol{r})$ is the stresslet

$$\mathbb{S} := \frac{1}{8\pi\mu}\left(\mathbb{I} - 3\frac{\boldsymbol{r}\boldsymbol{r}}{\|\boldsymbol{r}\|^2}\right)\frac{\boldsymbol{r}}{\|\boldsymbol{r}\|^3}.$$

From (2.7) and (2.3), we define the normalized stresslet coefficients

$$\beta_{xx}(t) = \tfrac{4}{3}\frac{(a-A)F}{8\pi\mu U} = (a-A)R(1+\dot{A}/U)$$

and

$$\beta_{yy}(t) = -\tfrac{4}{3}\frac{2bf_y}{8\pi\mu U} = -2rb\dot{b}/U,$$

which have units of squared length. With these, the far-field velocity is

$$\boldsymbol{u}(\boldsymbol{r},t) \approx \tfrac{3}{4}U\,(\beta_{xx}(t)\,\hat{\boldsymbol{x}}\hat{\boldsymbol{x}} + \beta_{yy}(t)\,\hat{\boldsymbol{y}}\hat{\boldsymbol{y}}) : \left(\mathbb{I} - 3\frac{\boldsymbol{r}\boldsymbol{r}}{\|\boldsymbol{r}\|^2}\right)\frac{\boldsymbol{r}}{\|\boldsymbol{r}\|^3}.$$

The Fourier series for these stresslet coefficients involve harmonics up to $\sin 4\Omega t$:

$$\begin{aligned}
\beta_{xx}(t) = {} & a_0 R \\
& + \frac{2a_0}{r_1}\left(r_0\,(R+2r_0) - r_1^2\right)\sin\Omega t + \frac{a_1\,(R^3 + 3R^2 r_0 - 3Rr_1^2 - 4r_0^3 + 2r_0 r_1^2)}{2R(R+2r_0)}\cos\Omega t \\
& + \frac{a_1}{2Rr_1}\left(2r_0(R+2r_0)^2 - r_1^2(R+8r_0) + \frac{4r_1^4}{R+2r_0}\right)\sin 2\Omega t - a_0(R+2r_0)\cos 2\Omega t \\
& \qquad - \frac{a_1}{2R}\left((R+2r_0)(R+3r_0) - 3r_1^2\right)\cos 3\Omega t - \frac{a_1 r_1}{4R}(R+2r_0)\sin 4\Omega t.
\end{aligned}$$

and

$$\frac{2U}{b_1\Omega}\,\beta_{yy}(t) = -(4b_0r_0 + b_1r_1)\cos\Omega t - 2(b_1r_0 + b_0r_1)\sin 2\Omega t + b_1r_1\cos 3\Omega t.$$

These Fourier series will allow us to well approximate particle paths far from the swimmer without needing to integrate

$$\dot{\boldsymbol{x}} = \boldsymbol{u}(\boldsymbol{x}, t),$$

where $\boldsymbol{x}$ represents the position of a particle.

We will save the remainder of this far-field derivation for Chapter 4 after exploring some modeling choices. We decide to first combine the two flagellar Stokeslets into a single flagellar Stokeslet whose position stays along the swimming axis (the $x$-axis in Fig. 2). While this new two-Stokeslet model looks even less like *C. reinhardtii*, our original model was not too accurate to begin with. Our main goal is to study the effect of time-dependence on particle displacements and thus also mixing, which this new model will still do. The huge benefit is that the two-Stokeslet swimmer has axial symmetry which makes collecting data, such as particle paths and displacements, much easier.

## 2.2 Two-Stokeslet Swimmer

Our model (pictured in Fig. 3) is further simplified from our three-Stokeslet model. It only contains two Stokeslets, one for the drag due to the body and a second representing the combined propulsion of the two flagella. To achieve locomotion we again allow the strength of the flagellar Stokeslet to vary, to represent the asymmetric drag in the power and recovery strokes.

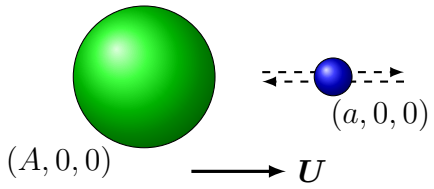


Figure 3: The two-Stokeslet swimmer model, swimming to the right. The oscillating sphere replaces the anterior flagella of *C. reinhardtii*.

| notation | description |
|---|---|
| $R$ | swimmer body radius |
| $r(t)$ | swimmer flagellum radius |
| $(a(t), 0, 0)$ | position of flagellar Stokeslet |
| $(A(t), 0, 0)$ | position of body Stokeslet |
| $\Omega$ | flagellar angular frequency |
| $\tau = 2\pi/\Omega$ | period of flagellar cycle |
| $\boldsymbol{U} = (U, 0, 0)$ | swimmer mean velocity |
| $f(t)$ | force on fluid due to flagellar Stokeslet |
| $F(t)$ | force on fluid due to body Stokeslet |
| $\boldsymbol{r} = (x, y, z)$ | spatial coordinates; particle position vector |

Table 1: Notation for two-Stokeslet swimmer model.

### 2.2.1 Swimming Dynamics and Force Balance

The swimmer moves at a mean swimming speed $U$ along the $x$-axis. In the comoving frame the body Stokeslet is located at $(A(t), 0, 0)$ and the flagellar Stokeslet is located at $(a(t), 0, 0)$. The forces on the fluid are

$$F(t)\hat{\boldsymbol{x}} = 6\pi\mu R\,(U + \dot{A}(t))\hat{\boldsymbol{x}}, \qquad f(t)\hat{\boldsymbol{x}} = 6\pi\mu\, r(t)(U + \dot{a}(t))\hat{\boldsymbol{x}}, \tag{2.8}$$

for the body and flagellar Stokeslets, respectively, where $\mu$ is the dynamic viscosity of the fluid. We again assign $R$ to the radius of *C. reinhardtii* and $r$ as an effective radius of the flagella. See Table 1 for a collection of these variables and what they mean.

A neutrally buoyant swimmer in the Stokes flow regime leads to no net force on the

fluid:

$$F(t) + f(t) = 0. \tag{2.9}$$

In a comoving frame traveling at the mean swimming velocity $U$, the positions of the Stokeslets must be periodic:

$$\langle \dot{A} \rangle = \langle \dot{a} \rangle = 0. \tag{2.10}$$

From (2.8) and (2.9), we have

$$R(U + \dot{A}(t)) = -r(t)(U + \dot{a}(t)), \tag{2.11}$$

which upon time-averaging and using (2.10) gives

$$RU = -U\langle r \rangle - \langle r\dot{a} \rangle,$$

and so the mean swimming velocity is

$$U = -\langle r\dot{a} \rangle / (R + \langle r \rangle). \tag{2.12}$$

Similar to the previous model, correlations between $\dot{a}(t)$ and $r(t)$ are entirely responsible for the swimmer moving forward.

The simplest time-dependence we can put is

$$a(t) = a_0 + a_1 \cos \Omega t, \qquad r(t) = r_0 + r_1 \sin \Omega t. \tag{2.13}$$

These being out of phase optimizes the swimmer's power and recovery strokes, thus maximizing the swimming speed. These prescribed functions, along with (2.12), give the mean swimming speed

$$U = \frac{\Omega\, a_1 r_1}{2(R + r_0)}. \tag{2.14}$$

From (2.11) we obtain

$$\begin{aligned}\dot{A}(t) &= -U - r(t)(U + \dot{a}(t))/R \\ &= \frac{\Omega\, a_1 r_1}{2R}\left\{\left(\frac{2r_0}{r_1} - \frac{r_1}{R + r_0}\right)\sin\Omega t - \cos 2\Omega t\right\}\end{aligned}$$

which again can be integrated to find $A(t)$.

### 2.2.2 Parameters for *C. reinhardtii*

We select the parameters of our model according to [21, 24, 42]. We take an average swimming velocity of $U = 100$ $\mu$m/s, an effective spherical body radius of $R = 4$ $\mu$m. The number of flagellar beats/strokes per second, $f_b = 50$ Hz (or $\Omega = 100\pi$ rad/s). The two flagella are represented by a single Stokeslet with effective radius $r(t)$, with time-dependence as in Eq. (2.13). This radius takes on a sinusoidal relationship with average value $r_0 = 2$ $\mu$m and amplitude given by $r_1 = 0.4$ $\mu$m (derived by adopting the drag coefficients on a slender rod and converting to the drag coefficient on a sphere).

The above quantities were averaged out from the following sets of data. From Leptos et al. [42]: body radius, $R \approx 5$ $\mu$m; flagellar length, 10-12 $\mu$m; beat frequency, $f_b = 1/\tau \approx$ 50 Hz; swimming speed $U = 100$ $\mu$m/s. From Guasto et al. [24]: body radius, $R \approx 3.5$ $\mu$m; mean frequency, $f_b = 53 \pm 5$ Hz (period $T = 18.9$ ms); mean swimming speed, $U = 134$ $\mu$m/s. From Friedrich and Jülicher [21]: period, $\tau \approx 15$ ms; flagellar length, $L = 12$ $\mu$m; body semiaxes 3.7 $\mu$m and 5 $\mu$m; flagellar radius (circular cross section) $r = 0.1$ $\mu$m; resistive force coefficients of a slender rod, $\zeta_\parallel = 2\pi\eta/[\ln(2L/r) - 3/2]$, $\zeta_\perp = 4\pi\eta/[\ln(2L/r) - 3/2]$; $\eta L^3/\kappa = 100$. We used videos and other experimental results from the above references to estimate what portions of the flagella are perpendicular or parallel to the flow. Then we combine this with the slender rod coefficients to make a

| notation | value range | dimensionless | description |
|---|---|---|---|
| $U$ | 100 $\mu$m/s | 1 | swimming speed |
| $R$ | 4 $\mu$m | 1 | body radius |
| $f_b$ | 50 Hz | 2 | flagellar beat frequency |
| $\Omega$ | $100\pi$ rad/s | $4\pi$ | flagellar frequency |
| $r_0$ | 2 $\mu$m | 0.5 | average effective flagellar radius |
| $r_1$ | 0.4 $\mu$m | 0.1 | flagellum's radial oscillation |
| $a_0$ | 6.5 $\mu$m | 1.625 | average position of flagellar Stokeslet |
| $a_1$ | 9.549 $\mu$m | 2.387 | oscillation amplitude of flagellar position |

Table 2: Physical parameters of *Chlamydomonas reinhardtii*. In dimensionless form; length scale is 4 $\mu$m and the time scale is 1/25 s.

guess for $r(t)$.

The average position of the flagellar Stokeslet ($a_0$) is a free parameter, since it does not affect the speed of the swimmer (2.14). However, it does impact the entrainment of particles. The oscillation strength of the flagellar Stokeslet's position ($a_1$) is quite the opposite of a free parameter. Due to the force balance imposed by the swimmer and all of the other parameters already chosen, $a_1$ is explicitly determined by (2.14); it is approximately 9.5 $\mu$m. This seems reasonable but is difficult to justify as portions of the flagella move at different speeds. Along these same lines, $a_0$ is difficult to determine, but we will start with assuming $a_0 = 6.5$ $\mu$m. We experiment with these parameters to study how each of them affect the flow field and entrainment, and to determine appropriate parameter sets for *C. reinhardtii* and other swimmers.

We introduce scalings to non-dimensionalize our system, yielding a swimmer with unit body radius and unit swimming speed. This results in a length scale of $L = 4$ $\mu$m and a time scale of $T = 1/25$ s. A collection of these parameters, and their non-dimensionalized values, can be found in Table 2.

**Alternative Parameter Set**

While analyzing our initial choice of parameters, we thought the distance between the Stokeslets fluctuated too much. We investigate this by creating an additional parameter set with a smaller $a_1$ (previously $a_1 \approx 2.4$), now we tried halving that. Keeping all other parameters fixed forces $r_1$ to double.

### 2.2.3 Numerical Integration for a Single Swimmer

With our parameter sets determined and the swimming dynamics set, we are ready to gather some results. We assume idealized fluid particles whose position $\boldsymbol{r}(t)$ obeys

$$\dot{\boldsymbol{r}} = \boldsymbol{u}(\boldsymbol{r}, t)$$

where $\boldsymbol{u}(\boldsymbol{r}, t)$ is the velocity of the fluid. We begin by numerically finding some particle paths by integrating the flow field along trajectories.

**Regularized Stokeslets**

We speed up the numerics by regularizing the Stokeslets in order to remove singularities from the flow. The idea of regularized Stokeslets was first introduced by Cortez (see [7, 8]). We pick the regularization from the analytic model in Hernandez-Ortiz et al. [27]. The linearity of the Stokes equation allows us to fully determine the velocity field of the swimmer in the comoving frame by a sum of the two regularized Stokeslets (ambient flow not included)

$$\boldsymbol{u}(\boldsymbol{r}) = F\hat{\boldsymbol{x}} \cdot \mathbb{G}^{\xi}(\boldsymbol{r} - A\,\hat{\boldsymbol{x}}) + f\hat{\boldsymbol{x}} \cdot \mathbb{G}^{\xi}(\boldsymbol{r} - a\,\hat{\boldsymbol{x}}),$$

where $\xi$ is a measurement of the regularization. Here $\mathbb{G}^{\xi}(\boldsymbol{r})$ is the regularized Oseen tensor,

$$\mathbb{G}^{\xi}(\boldsymbol{r}) = \frac{1}{8\pi\mu\|\boldsymbol{r}\|}\left(\mathbb{I} + \frac{\boldsymbol{r}\,\boldsymbol{r}}{\|\boldsymbol{r}\|^2}\right)\operatorname{erf}\left(\xi\|\boldsymbol{r}\|\right) + \frac{1}{8\pi\mu}\left(\mathbb{I} - \frac{\boldsymbol{r}\,\boldsymbol{r}}{\|\boldsymbol{r}\|^2}\right)\frac{2\xi}{\sqrt{\pi}}\mathrm{e}^{-\xi^2\|\boldsymbol{r}\|^2}, \tag{2.15}$$

where the coefficient of the error function above is the standard Oseen tensor. Then the velocity field of a regularized Stokeslet, $\boldsymbol{u}_0 = \boldsymbol{f}_0 \cdot \mathbb{G}^{\xi}$, satisfies Stokes equation with a regularized delta function

$$-\nabla p + \mu\nabla^2\boldsymbol{u}_0 = -\boldsymbol{f}_0\delta^{\xi}(\boldsymbol{r}), \qquad \nabla\cdot\boldsymbol{u}_0 = 0.$$

where

$$\delta^{\xi}(\boldsymbol{r}) = \frac{\xi^3}{\pi^{3/2}}\left(\tfrac{5}{2} - \xi^2\|\boldsymbol{r}\|^2\right)\mathrm{e}^{-\xi^2\|\boldsymbol{r}\|^2}$$

is the suitably chosen regularized delta function [27].

In the limit $\xi \to \infty$, we recover the non-regularized Stokeslet. We can think of $1/\xi$ as the characteristic width of the regularized delta function. We choose the characteristic width to be one-fifth of the effective radius for each Stokeslet ($1/\xi = \frac{1}{5}R$ and $1/\xi = \frac{1}{5}r(t)$ for the body and flagellar Stokeslets, respectively).

With the regularization, the singularity is now removable. We can thus Taylor expand near the removable singularity

$$\mathbb{G}^{\xi}(\boldsymbol{r}) = \frac{1}{2\pi\mu}\frac{\xi}{\sqrt{\pi}}\mathbb{I} - \frac{1}{6\pi\mu}\frac{\xi^3}{\sqrt{\pi}}\left(2\mathbb{I}\|\boldsymbol{r}\|^2 - \boldsymbol{r}\,\boldsymbol{r}\right) + O\left(\|\boldsymbol{r}\|^4\right)$$

and apply this approximation for small values of $\|\boldsymbol{r}\|$. The parameter sets determine everything else about the velocity field. We now analyze particles in this flow field.

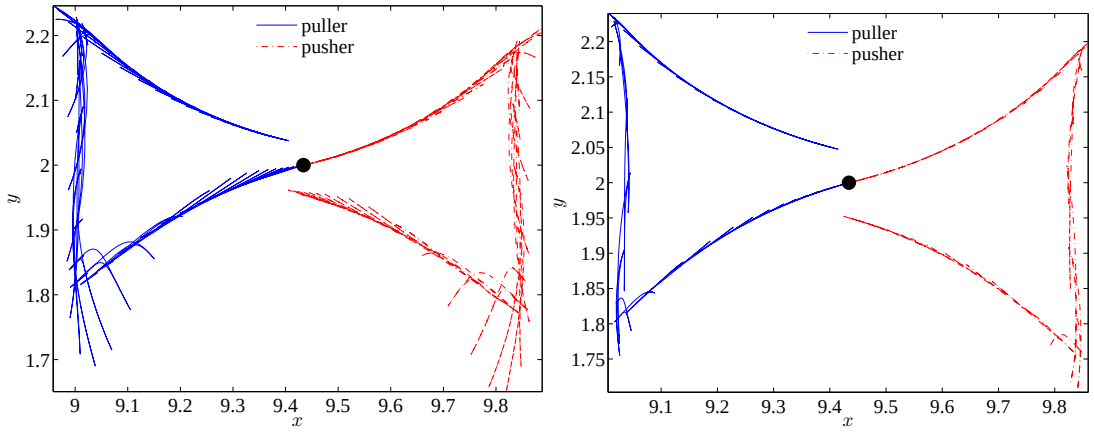


Figure 4: Each plot shows a pair of particle paths starting from the same location; pullers have $a_0 = 13/8$, pushers have $a_0 = -13/8$. Marker added at initial particle position: $(\lambda/2, 2, 0)$, where $\lambda = 40U\tau$. Note that the particle paths are continuous, the cusp-like appearance is purely caused by the fast flagellar oscillations. Left: Main parameter set. Right: Alternative parameter set.

### Particle Paths

We notice loop-like trajectories for particles that see the swimmer pass by them, a result commonly found with steady swimmers [46, 63, 76]. The loop-like trajectories cause the net displacement to be much smaller than the distance traveled by the particle, as seen in Fig. 4 by the distance between where the trajectories end and where they begin (marker added at start of each path).

The loop-like behavior is broken for particles that are located near the start or end of the swimmer's path, resulting in larger displacements; see Fig. 5 for a few examples. This applies to swimmers with finite path lengths, a trait expressed by *E. coli*'s run-and-tumble dynamics; as well as organisms with curved trajectories [61] or ones in bounded domains [62].

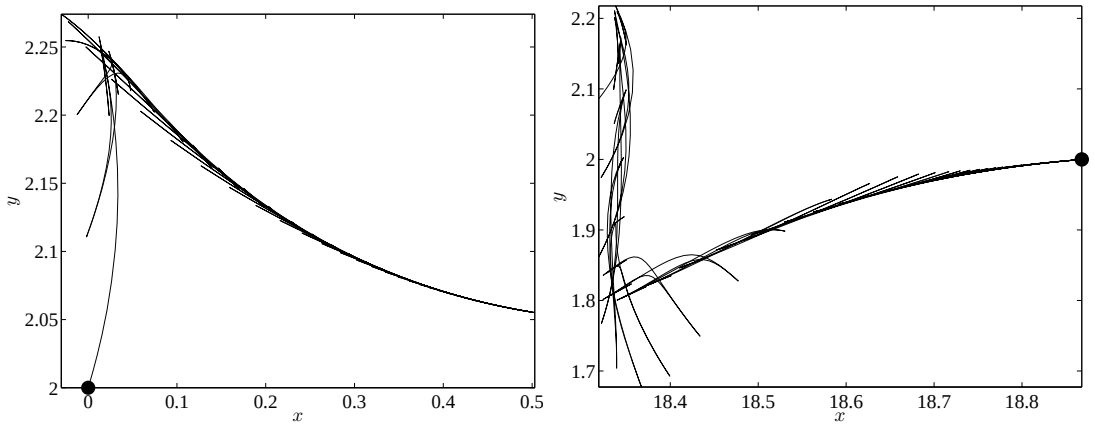


Figure 5: Main parameter set, pullers only. Left: Particle path starting at $(0, 2, 0)$, near where the swimmer starts (the origin). Right: Particle path starting at $(40U\tau, 2, 0)$, near the swimmer's stopping point after 40 periods.

### 2.2.4 Near-Field Displacements and Atmospheres

Our goal is to quantify particle displacements caused by the swimmer's motion and analyze the different ways that particles get displaced. The swimmer can entrain particles inside what is called an atmosphere: a region of fluid that follows the swimmer around, a term coined in relation to the atmosphere of the Earth that remains around it as we move around the sun. The particles can also be pushed aside by the swimmer, or they can come close to the swimmer and follow it for a finite amount of time but not be infinitely entrained.

#### Particle Displacement

Using the *C. reinhardtii* parameters derived earlier and the chosen regularization of the Stokeslet, we study displacements of particles near the swimmer by integrating an initial mesh of particles (again we assume the particles follow the fluid flow). After integrating the mesh of particles, we can then calculate and plot the net displacement of all particles;

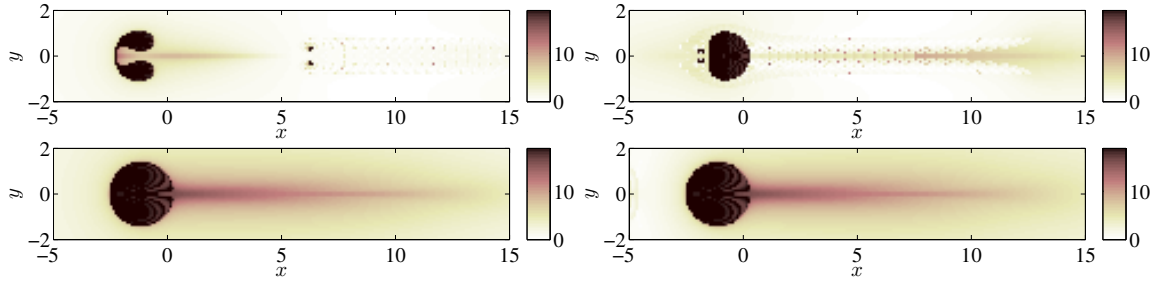


Figure 6: Particle displacement as a function of initial particle position for the main parameter set. Swimmer has traveled for 20 periods (approximately 18 units). Moderate example of a puller (top-left, $a_0 = 4$) and a pusher (top-right, $a_0 = -4$). Extreme example of a puller (bottom-left, $a_0 = 25$) and a pusher (bottom-right, $a_0 = -25$).

see Fig. 6 for a few examples.

These figures show a clear atmospheric region in the left-half side of each image. The shape and dynamics of the atmosphere change with varying parameters. The only difference in the images is the parameter $a_0$ (the time-averaged separation between the Stokeslets). With larger separations we see little to no interactions between the Stokeslets; all that matters is the flow field near the main Stokeslet (atmosphere) as well as the stresslet strength determined by the Stokeslet pair (this is supported by nearly identical images for $a_0 = 25$ and $a_0 = -25$).

The other thing to note is the faint stripes appearing on the right-half side the first image ($a_0 = 4$). They first appear around the initial location of the flagellar Stokeslet and repeat after every full period (spacing is equal to $U \cdot \tau$, the distance traveled by the swimmer in one period). The stripes seem to be created due to a combined effort of both Stokeslets. This shows up for other positive values of $a_0$, but is not captured for $a_0 = 25$, due to being out of the field of view. We also plot some similar results for the alternative parameter set, see Fig. 7.

These "faint stripes" can be explained as follows. As the flagellar Stokeslet oscillates,

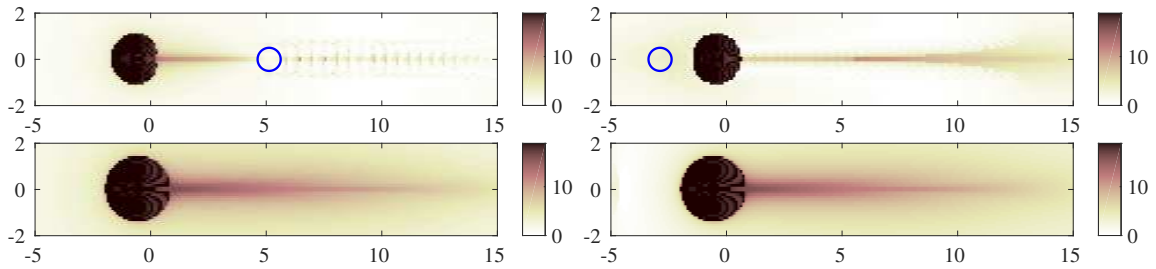


Figure 7: Secondary parameter set particle displacement as a function of initial particle position. Swimmer has traveled for 20 periods (approximately 18 units). Moderate example of a puller (top-left, $a_0 = 4$) and a pusher (top-right, $a_0 = -4$). Extreme example of a puller (bottom-left, $a_0 = 25$) and a pusher (bottom-right, $a_0 = -25$). Circle indicates initial location of flagellar Stokeslet.

it isolates a small region of particles into a temporary, secondary atmosphere. This small region of particles remains closer to the swimming axis which allows them to be displaced larger distances by the primary atmosphere (either by entrainment or due to being pushed by the primary atmosphere). The remaining particles that do not stay close to the axis, and instead pass around the swimmer, do not receive such a large displacement from the body Stokeslet; these exhibit loop-like trajectories.

There are a few things to take note from Fig. 7. First of all, the shape of the atmospheres is different from those in Fig. 6. This means the parameters $a_1$ and $r_1$ have some impact on the atmosphere. However, varying $a_0$ for the alternative parameter set (Fig. 7) has little effect on the shape of the atmosphere. This is most likely a result of the Stokeslets staying more separated over time as $a_1$ is smaller in the alternative parameter set.

A not so surprising feature is that the particles are displaced differently around the swimmer depending on if the propulsion mechanism (flagellar Stokeslet) is in front of the swimmer like *C. reinhardtii* (a puller), or behind the swimmer (a pusher). Granted,

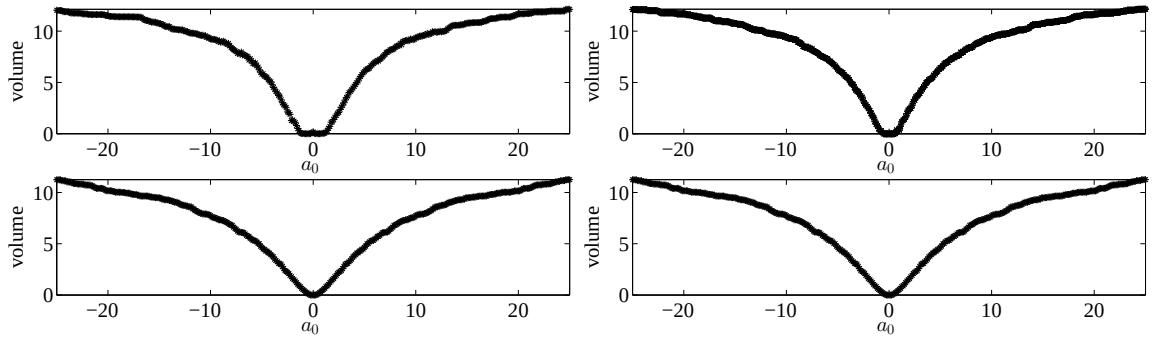


Figure 8: Volume of atmosphere as a function of parameter $a_0$ for the main parameter set (left) and the alternative parameter set (right). The top row is the unsteady case, while the bottom row is the steady case (note the steady case is identical for both parameter sets; this is the result of time-averaging).

we are focusing on the case $a_0 > 0$ (pullers, like *C. reinhardtii*) in this paper, but it is worth seeing the comparison within Figs. 6 and 7.

**Atmospheric Volume**

In Fig. 8 we vary the free parameter $a_0$, the average separation between the two Stokeslets (see Section 2.2). As $a_0$ increases in magnitude, the atmospheric volume levels off and approaches the volume of the closed streamline around a single steady Stokeslet in an ambient flow. We validate this by analyzing the atmospheric volume for a steady version of our two-Stokeslet swimmer (by averaging the dynamics). The flagellar Stokeslet provides a negligible volume in either case due to the wild fluctuations of its dynamics.

### 2.2.5 Far-Field Asymptotics

At moderate to large distances from the swimmer, our two-Stokeslet model can be well approximated by a stresslet (similar to the pair of differently orientated stresslets for

the three-Stokeslet model). The velocity in the comoving frame is given by

$$\boldsymbol{u}_{\text{comov}}(\boldsymbol{r}) = -U\hat{\boldsymbol{x}} + \tfrac{3}{4}U\beta\left(1 - 3\,\frac{xx}{\|\boldsymbol{r}\|^2}\right)\frac{\boldsymbol{r}}{\|\boldsymbol{r}\|^3}, \tag{2.16}$$

where

$$\beta = \frac{(a-A)F}{6\pi\mu U},$$

so that the stresslet is moving at the mean swimming speed $U$ in the $\hat{\boldsymbol{x}}$ direction, with a resulting apparent flow in the $-\hat{\boldsymbol{x}}$ direction. The streamfunction in the comoving frame is

$$\psi_{\text{comov}}(\rho, x) = -\tfrac{1}{2}U\rho^2 - \tfrac{3}{4}U\beta\,\frac{x\rho^2}{\|\boldsymbol{r}\|^3},$$

with

$$u_\rho = -\rho^{-1}\partial_x\psi, \qquad u_x = \rho^{-1}\,\partial_\rho\psi.$$

Figure 9 shows the streamline pattern in the comoving frame (for $\frac{3}{4}\beta = 1$), which suggests the presence of an atmosphere: a closed streamline in the comoving frame. We can find the equation for the atmosphere by solving $\psi_{\text{comov}} = 0$,

$$-\tfrac{1}{2} - \tfrac{3}{4}\beta\,\frac{x}{(\rho^2 + x^2)^{3/2}} = 0,$$

so that

$$\rho^2_{\text{atm}}(x) = -x\left(x + (\tfrac{3}{2}\beta)^{2/3}(-1/x)^{1/3}\right).$$

Note that $\rho_{\text{atm}}(0) = \rho_{\text{atm}}(-\operatorname{sign}(\beta)\sqrt{\frac{3}{2}|\beta|}) = 0$, which means the atmosphere extends from $x = 0$ to $x = -\operatorname{sign}(\beta)\sqrt{\frac{3}{2}|\beta|}$. The atmosphere is plotted as a thick line in Fig. 9.

We also have an explicit expression for the volume of the atmosphere, for instance for $\beta > 0$:

$$V_{\text{atm}} = \int_{-\sqrt{2\beta}}^{0} \pi\rho^2_{\text{atm}}(x)\,\mathrm{d}x = \tfrac{1}{5}\sqrt{6}\pi|\beta\,|^{3/2},$$

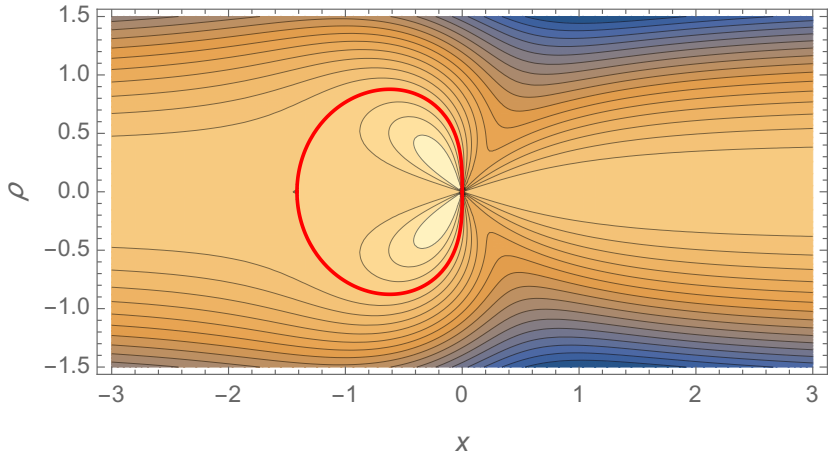


Figure 9: The streamlines in the comoving frame for the moving stresslet (Eq. (2.16)). The thick line shows the 'atmosphere' (closed streamline in the comoving frame).

where the final expression is also valid for $\beta < 0$. The volume is useful for computing the transport due to particles trapped in the atmosphere.

### 2.2.6 Modeling Remarks

We originally wanted to explore the relationship between the swimming parameters and the volume of the atmosphere. But after looking at some of the results above, we realized these atmospheres did not represent any realistic atmosphere that may exist for *C. reinhardtii*. This is due to the near-field of the swimmer not being accurately represented by our current model, for both the two-Stokeslet case and the stresslet approximation. In the next chapter we develop a model that is still simple and has axial symmetry, but whose flow field accurately resembles a swimmer with a no-slip surface on its body.

# Chapter 3

# Unsteady Microswimmer with a No-Slip Body

We begin this chapter by deriving a flow field for *C. reinhardtii* that represents its body by a rigid sphere. This requires the use of Faxén's Law [19] to accurately derive the drag force. We additionally need higher order singular solutions of Stokes flow to create an accurate image system within the sphere (this is required to cancel the flagellar Stokeslet's velocity at the surface of the sphere). Complex interactions between the flagellar Stokeslet and the sphere increase the difficulty in analyzing the large and rare displacements of particles that come near the swimmer.

## 3.1 Dumbbell Model Derivation

A dumbbell model usually refers to any two-body system. This definition would normally include our two-Stokeslet model, however, we will only be referring to the following model as the dumbbell model for clarity. The following derivation will seem very similar to the previous two models. The body of the swimmer is now represented by a rigid sphere, while the net propulsion of the flagella is still modeled by a single Stokeslet; this system has an analytic solution which we will discuss later. To achieve locomotion we again

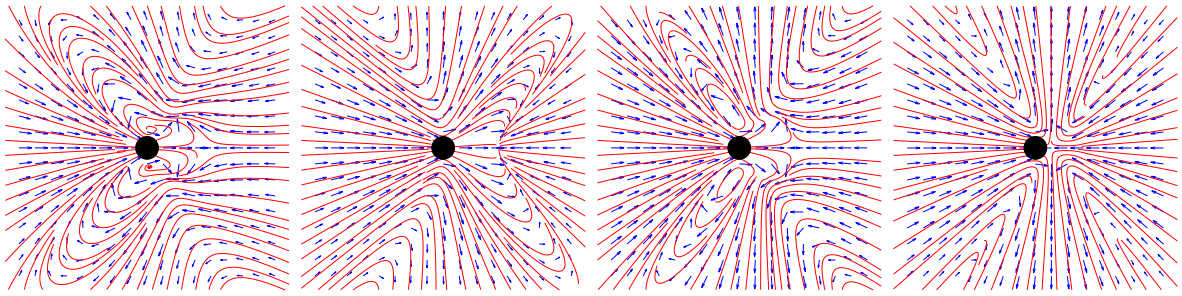

(a) (b) (c) (d)

Figure 10: Time-averaged velocity fields of our three-Stokeslet model, similar to that of [16] for: (a) the in-plane cross section ($xy$-plane containing the flagella; compare to [24, Fig. 2(a)]), (b) out of plane cross section ($xz$-plane), and (c) the azimuthally averaged flow. (d) Time-averaged velocity field of our dumbbell model.

allow the strength of the flagellar Stokeslet to vary.

Figure 10 compares the streamlines of our axially-symmetric model to our early three-Stokeslet model that matches experimental results [16, 24] for *C. reinhardtii*, which lacks this symmetry. We note that the azimuthally averaged flow looks most like the flow in the plane containing the flagella (in-plane), but it is likely that particle advection is not dominated by one cross section of a 3-dimensional flow. Regardless, from the point of view of drift, our main interest is seeing the interplay of a solid no-slip surface and moving flagella, so it is crucial to get the surface right, but less important to represent the flagella accurately. The actual flagella separate and partially wrap around the swimmer, which cannot occur in a dumbbell model; but we do match the swimmer's size, velocity, and physical oscillations.

### 3.1.1 Swimming Dynamics

The swimmer moves at a mean swimming speed $U$ along the $x$-axis. In the comoving frame the body sphere is located at $(A(t), 0, 0)$, with fixed radius $R$ (Fig. 11). The

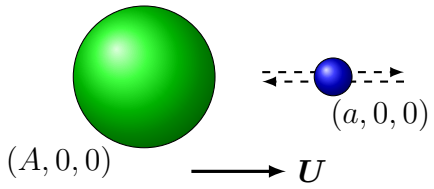


Figure 11: The dumbbell model (the body is now represented by a solid sphere, instead of a Stokeslet as in Section 2.2), swimming to the right.

| notation | description |
|---|---|
| $R$ | swimmer body radius |
| $r(t)$ | effective flagellar Stokeslet radius |
| $(a(t), 0, 0)$ | position of flagellar Stokeslet in comoving frame |
| $(A(t), 0, 0)$ | position of swimmer's body in comoving frame |
| $\Omega$ | flagellar angular frequency |
| $\tau = 2\pi/\Omega$ | period of flagellar cycle |
| $\boldsymbol{U} = (U, 0, 0)$ | swimmer mean velocity |
| $f(t)$ | force on fluid due to flagellar Stokeslet |
| $F(t)$ | force on swimmer's body due to flow |
| $\beta(t)$ | stresslet coefficient; see Section 4.2 |
| $\lambda(t)$ | swimming path length ($= Ut$) |
| $\boldsymbol{r} = (x, y, z)$ | spatial coordinates; particle position vector |

Table 3: Notation for dumbbell swimmer model.

flagellar Stokeslet is located at $(a(t), 0, 0)$, with effective radius $r(t)$. By axial symmetry, the drag on the sphere has the form $\boldsymbol{F} = (F, 0, 0)$. Faxén's Law for the drag on the body sphere [25] gives

$$F = 6\pi\mu R \left(1 + \tfrac{1}{6}R^2\nabla^2\right) u_{\text{flag}}(\boldsymbol{r})|_{\boldsymbol{r}=(A,0,0)} - 6\pi\mu R \left(U + \dot{A}\right), \tag{3.1}$$

where $\mu$ is the dynamic viscosity of the fluid and $u_{\text{flag}}(\boldsymbol{r}) = \boldsymbol{u}_{\text{flag}}(\boldsymbol{r})\cdot\hat{\boldsymbol{x}}$ is the $x$-component of the velocity due to the flagellar Stokeslet. Table 3 lists the variables and their meaning.

A neutrally buoyant swimmer in the Stokes regime leads to no net force on the fluid;

hence, $F = f$, where $F$ is the force on the sphere and

$$f = 6\pi\mu r\,(U + \dot{a}) \tag{3.2}$$

is the force due to the flagellar Stokeslet. Combining (3.1) and (3.2) gives us a differential equation relating the position of the swimmer's body $A(t)$ and of the flagellar Stokeslet $a(t)$:

$$\dot{A} = -U + \left[\left(1 + \tfrac{1}{6}R^2\nabla^2\right) u_{\text{flag}}(\boldsymbol{r})\right]_{\boldsymbol{r}=(A,0,0)} - (U + \dot{a})\, r/R. \tag{3.3}$$

In order to solve (3.3) for $A(t)$, given $a(t)$, we must impose some additional constraints. In a comoving frame traveling at the mean swimming speed $U$, the time-averaged velocities of the spheres must vanish:

$$\langle \dot{A} \rangle = \langle \dot{a} \rangle = 0, \tag{3.4}$$

where $\langle \cdot \rangle$ denotes the average over a time period $\tau = 2\pi/\Omega$. The simplest time-dependence we can put on the flagellar Stokeslet is

$$a(t) = A(0) + a_0 + a_1 \cos \Omega t, \qquad r(t) = r_0 + r_1 \sin \Omega t. \tag{3.5}$$

These are out of phase to mimic the swimmer's power and recovery strokes. Note that $\langle \dot{a} \rangle = 0$ since it is assumed periodic. We've also defined $a(t)$ relative to $A(0)$, since (3.3) is invariant under a shift of $a(t)$ and $A(t)$ by the same constant.

A few observations on the strategy for solving for $A(t)$ are in order. Equation (3.3) with the constraints (3.4) form a nonlinear eigenvalue problem for $A(t)$ and the mean swimming speed $U$ (the eigenvalue). Only in very special cases will an analytic solution emerge, so we proceed numerically. We use a shooting method: we start with a guess for $U$, then integrate (3.3) until time $\tau$, with initial condition $A(0) = 0$. We then

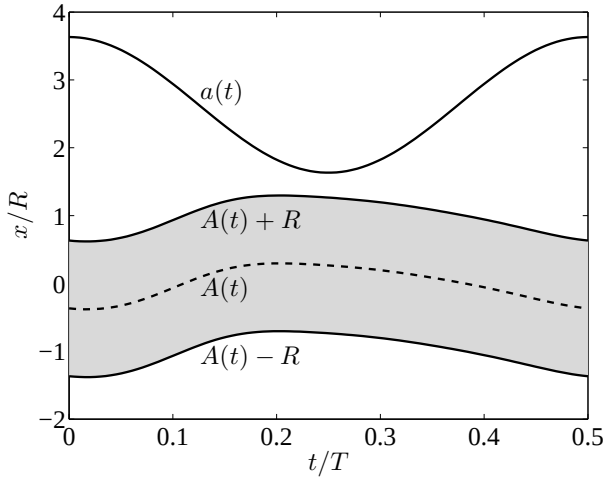


Figure 12: The position of the body sphere center $A(t)$ and the flagellar Stokeslet $a(t)$, also showing the extent of the body. These are in the comoving frame during one full period ($\tau = 0.5T$), plotted along the non-dimensionalized axes using the scales in Table 4.

iterate by varying $U$ until $A(0) = A(\tau)$ (using Matlab's `fzero`). The choice $A(0) = 0$ is arbitrary, and it proves more convenient to subtract the average of $A$ from $a(t)$ and $A(t)$ to make $\langle A \rangle = 0$. See Fig. 12 for a plot of $A(t)$ and $a(t)$ over one full period in the comoving frame, using the physical parameters listed in Table 4 and described below.

### Parameters for C. reinhardtii

We select the parameters of our model according to [21, 24, 42] (and references therein). We take an effective spherical body radius of $R = 4$ $\mu$m, and the number of flagellar beats/strokes per second, $f_b = 50$ Hz (or $\Omega = 100\pi$ rad/s). The flagella are represented by a single Stokeslet located at $a(t)$ with effective radius $r(t)$, with time-dependence as in (3.5). We pick the free variables $a_0, a_1, r_0, r_1$ in order to yield a mean swimming velocity close to 100 $\mu$m/s, while also trying to match the oscillating drag due to the beating flagella. We introduce a length scale $L = 4$ $\mu$m and a time scale $T = 1/25$ s to

| notation | value | dimensionless | description |
|---|---|---|---|
| $U$ | 98 $\mu$m/s | 0.98 | swimming speed |
| $R$ | 4 $\mu$m | 1 | body radius |
| $f_b$ | 50 Hz | 2 | flagellar beat frequency |
| $\tau$ | $1/f_b$ | $1/2$ | period of flagellar cycle |
| $\Omega$ | $2\pi f_b$ | $4\pi$ | flagellar angular frequency |
| $r_0$ | 3.2 $\mu$m | 0.8 | average effective flagellar radius |
| $r_1$ | 2 $\mu$m | 0.5 | flagellum's radial oscillation |
| $a_0$ | 12 $\mu$m | 3 | relative position of flagellar Stokeslet |
| $a_1$ | 4 $\mu$m | 1 | oscillation amplitude of flagellar position |

Table 4: Physical parameters of *C. reinhardtii*, non-dimensionalized using a length scale, $R = 4$ $\mu$m, and time scale, $T = 1/25$ s.

non-dimensionalize our system, yielding a swimmer with unit body radius and with a stroke period of one-half. These parameters and and their non-dimensionalized values are collected in Table 4.

### 3.1.2 Flow Field and Image System

The velocity field due to a translating sphere involves a Stokeslet and a source dipole:

$$\boldsymbol{u}_{\text{sphere}}(\boldsymbol{r}) = 6\pi\mu R\left(U + \dot{A}\right)\hat{\boldsymbol{x}} \cdot \left(1 + \tfrac{1}{6}R^2\nabla^2\right)\mathbb{G}(\boldsymbol{r}^*),$$

where $\boldsymbol{r}^* = \boldsymbol{r} - A\hat{\boldsymbol{x}}$ and $\mathbb{G}(\boldsymbol{r})$ is the Oseen tensor

$$\mathbb{G}(\boldsymbol{r}) = \frac{1}{8\pi\mu\|\boldsymbol{r}\|}\left(\mathbb{I} + \frac{\boldsymbol{r}\boldsymbol{r}}{\|\boldsymbol{r}\|^2}\right).$$

The velocity due to the flagellar Stokeslet is

$$\boldsymbol{u}_{\text{flag}}(\boldsymbol{r}) = f\hat{\boldsymbol{x}} \cdot \mathbb{G}(\boldsymbol{r} - a\,\hat{\boldsymbol{x}}).$$

If we add the flagellar Stokeslet, we need to include images inside the sphere to preserve the no-slip boundary condition, as described by Oseen [56]. Here we use the simplified

form for a sphere and Stokeslet that are axisymmetrically aligned along the direction of motion [22, 48]:

$$\boldsymbol{u}_{\text{image}}(\boldsymbol{r}) = -\tfrac{1}{2}\left(3c_\alpha - c_\alpha^3\right) f\hat{\boldsymbol{x}} \cdot \mathbb{G}(\boldsymbol{r} - \boldsymbol{\alpha}^*) + R\left(c_\alpha^2 - c_\alpha^4\right)(f\hat{\boldsymbol{x}}\hat{\boldsymbol{x}} \cdot \nabla) \cdot \mathbb{G}(\boldsymbol{r} - \boldsymbol{\alpha}^*) - \tfrac{1}{4}R^2 c_\alpha \left(1 - c_\alpha^2\right)^2 f\hat{\boldsymbol{x}} \cdot \nabla^2 \mathbb{G}(\boldsymbol{r} - \boldsymbol{\alpha}^*),$$

where $c_\alpha = R/\alpha$, $\alpha = a - A$ is the separation between the flagellar Stokeslet and the center of the swimmer's body, and $\boldsymbol{\alpha}^* = (R^2/\alpha + A)\,\hat{\boldsymbol{x}}$ is the location of the image singularities in the comoving frame.

Lastly we add an ambient flow in the comoving frame to get the full velocity field of our model:

$$\boldsymbol{u}_{\text{comov}}(\boldsymbol{r}) = -U\hat{\boldsymbol{x}} + \boldsymbol{u}_{\text{flag}}(\boldsymbol{r}) + \boldsymbol{u}_{\text{sphere}}(\boldsymbol{r}) + \boldsymbol{u}_{\text{image}}(\boldsymbol{r}). \tag{3.6}$$

This is related to the velocity field in the lab (fixed) frame by

$$\boldsymbol{u}_{\text{lab}}(\boldsymbol{r}) = \boldsymbol{u}_{\text{comov}}(\boldsymbol{r} - Ut\,\hat{\boldsymbol{x}}) + U\hat{\boldsymbol{x}}. \tag{3.7}$$

Recall that many of the parameters, such as those defined in (3.5), will have a time-dependence that we did not indicate explicitly in the velocity fields above.

### 3.1.3 Regularization of the Flagellar Stokeslet

One of the main motivations of using our final dumbbell model is to account for the rigid no-slip surface of the body, since it can lead to stickiness of fluid particles [76]. To simplify the model as much as possible, we used a point-singularity representation for the flagellum. Since we want to simulate the advection of particles by our swimmer, it is wise to regularize the flagellum in order to avoid infinite velocities inside the fluid. We again use the regularization from the analytic model in Hernandez-Ortiz et al. [27].

The flow field of the regularized flagellar Stokeslet in the comoving frame is

$$\boldsymbol{u}_{\text{flag}}(\boldsymbol{r}) = f\hat{\boldsymbol{x}} \cdot \mathbb{G}^{\xi}(\boldsymbol{r} - a\,\hat{\boldsymbol{x}}).$$

Recall the regularized Oseen tensor used in our earlier model, (2.15). This time we choose the regularization scale to be $\xi^{-1} = \frac{1}{4}r_0$, a value smaller than the minimum effective flagellar radius, $r(t)$. This is small enough to ensure that the solution for $A(t)$ is essentially unaffected by the regularization.

## 3.2 Numerical Integration for a Single Swimmer

As the swimmer moves, it displaces fluid particles. The net nonzero displacement of fluid particles after the swimmer has passed is often referred to as *Darwin drift* [11, 45, 49], to distinguish it from Stokes drift due to wave motion. Here we will use the more precise word 'displacement' when referring to particle drift. The particle displacements are obtained by computing the fluid particle trajectories, and in this section we do so using numerical integration. In Sections 4.1 and 4.2 we will derive features of the particle displacements using asymptotic analysis.

We assume idealized fluid particles whose position $\boldsymbol{r}$ obeys

$$\dot{\boldsymbol{r}} = \boldsymbol{u}(\boldsymbol{r}, t), \qquad \boldsymbol{r}_0 = (x_0, y_0, 0), \tag{3.8}$$

where we set $z_0 = 0$ without loss of generality by exploiting the axial symmetry. In the lab (fixed) frame we use (3.7) on the right-hand side of (3.8) and include the time-dependence of all the parameters. In the following sections we examine particle *paths*, as given by $\boldsymbol{r}(t)$, and particle *displacements*,

$$\Delta_{\lambda}(x_0, y_0) = \|\boldsymbol{r} - \boldsymbol{r}_0\|, \qquad \lambda = Ut,$$

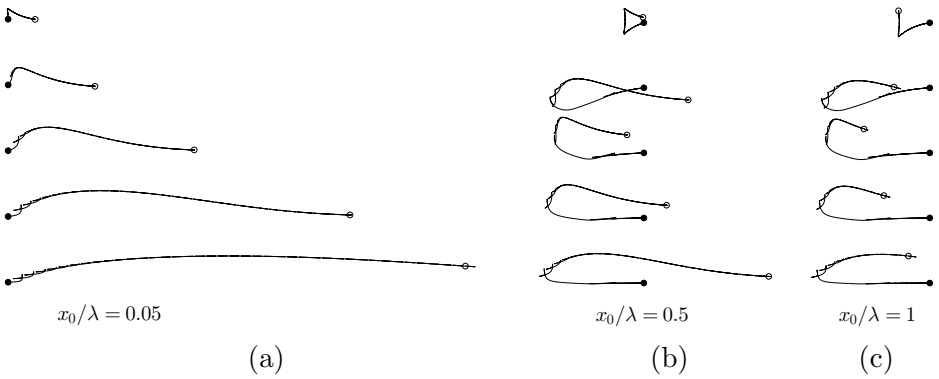


Figure 13: Particle trajectories in the lab frame starting at $(x_0, y_0, 0)$ with the swimmer's body centered at $(A(0), 0, 0)$, which travels a net distance of $\lambda = 40\,U\tau$. From top to bottom, $\log(y_0/R) = 1, 0, -1, -2, -3$. The trajectories are offset vertically for clarity. The initial position of the particles is marked by solid dots and the final position by hollow dots. The apparent 'roughness' of the paths is due to the time-dependent swimming motion.

where $\lambda$ is the swimmer's path length. It is well-known that particles can have paths that undergo large excursions, and yet have relatively small displacements [11, 49]. At moderate and far distances from the swimmer, this near-closure is generic for potential and viscous flows [17]. We integrate (3.8) numerically with Matlab's `ode45`, using the non-dimensionalized values in Table 4.

### 3.2.1 Particle paths

We first discuss the particle paths in detail, before turning to the net displacements in Section 3.2.2. Figure 13(b) shows the classic loop-like trajectories for distant particles as the swimmer passes by them, a result commonly found with steady swimmers [11, 17, 46, 49, 63, 76]. The loop-like behavior is broken for particles close to the start or end of the swimmer's path (Fig. 13(a,c)), as pointed out in [46].

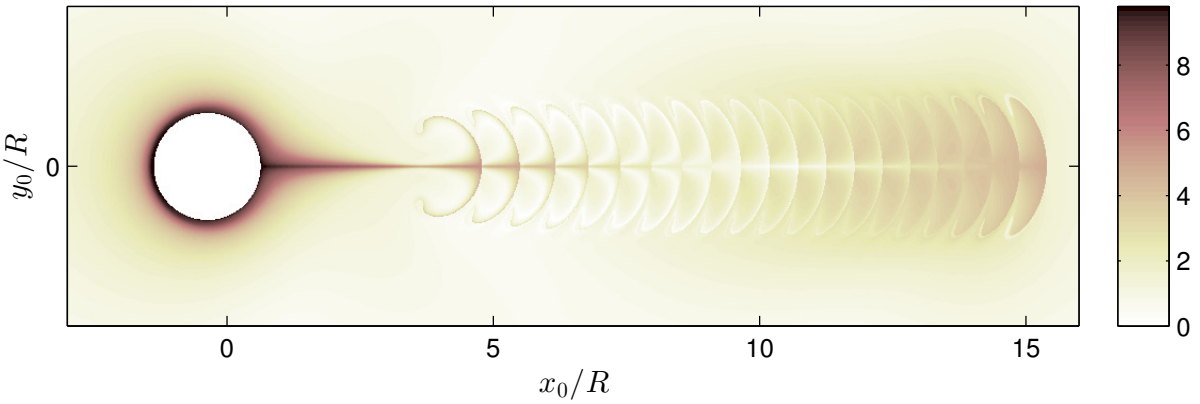


Figure 14: Plot of particle displacements, $\Delta_\lambda(x_0, y_0)/R$, as a function of initial particle position $(x_0, y_0, 0)$ for a swimmer starting at $(A(0), 0, 0)$ and swimming for 20 periods (or a net distance of $\lambda \approx 9.8R$). The white disk is the initial position of the swimmer's body.

### 3.2.2 Particle displacements

An immediate next step is to study the net displacement of each particle path. We begin by integrating an initial mesh of particles (again we assume idealized particles that follow the fluid flow). After integrating the particles, we can then calculate and plot their net displacement (Fig. 14). We recover the open trajectories (and thus larger displacements) of particles located near the start and end of the finite swimming path as mentioned in the previous section. We also see large displacements for particles that are in the path of the no-slip surface of the swimmer's body; this can be seen by the streak of large displacements along the swimming axis, immediately ahead of the sphere.

A sequence of faint stripes can also be seen in the right half of Fig. 14. They first appear near the initial location of the flagellar Stokeslet and repeat almost periodically. The spacing between stripes is roughly equal to $U\tau$, the distance traveled by the swimmer in one period. The leftmost stripe occurs at the first maximum excursion of the flagellar

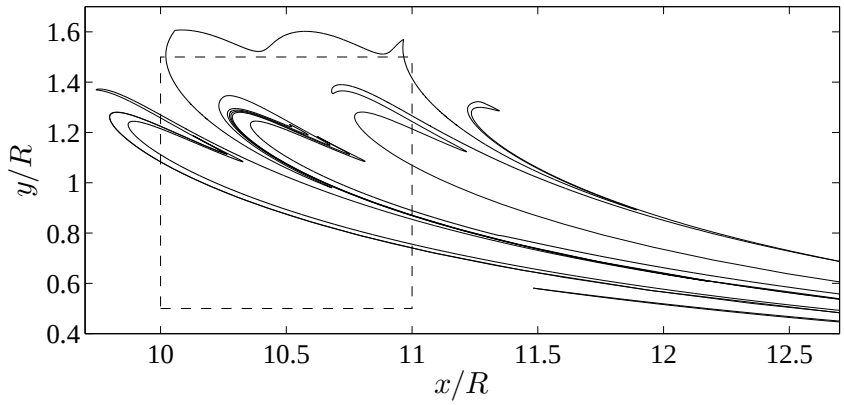


Figure 15: The swimmer starts centered at the origin and swims for 100 periods (a distance of about $49R$), passing through the an initial square of fluid particles (dashed) and deforming it (solid). The time dependence creates characteristic lobe structures.

Stokeslet from the the swimmer's body (see Fig. 12).

It is also instructive to examine how material lines of fluid particles are displaced by the swimmer. In Fig. 15 we take an initial square of fluid particles (dashed), located ahead of the swimmer. The solid lines then show the eventual fate of that square as its constituent particles are displaced. Notice the large amount of stretching and folding that creates 'lobes,' typically associated with mixing [2, 57, 80]. Here we have a transient process, which is more appropriately analyzed using methods from transient chaos in open flows [59, 74]. We do not carry out such analysis here; instead we will discuss mixing in terms of the statistics of particle displacements (Chapter 5).

# Chapter 4

# Velocity Field Asymptotics

For the remaining chapters on biomixing we focus on our dumbbell model with a no-slip, rigid spherical body. At the present moment we will analyze some of the limiting behaviors of our velocity field. The time-dependence near the swimmer leads to some interesting results, whereas the far-field barely notices the unsteady nature of our model.

## 4.1 Near-Field Asymptotics

The trajectories with the largest displacements commonly occur near the swimmer. In particular, particles directly in the path of the swimmer (small $y_0$) are displaced the most. In an inviscid fluid, or for squirmers, the largest displacements typically scale as $\log y_0$, since the largest displacements arise from particles that remain in the vicinity of stagnation points at the leading and trailing edges of the body. For no-slip spheres, the largest displacements scale as $1/y_0$ [18], this time due to particles that remain near the no-slip rigid surface. For our time-dependent swimmer, the situation is more complicated, since particles near the no-slip body of the swimmer are still affected by the time-dependent flagellar Stokeslet. We now model these particles in order to find the largest particle displacements.

### 4.1.1 Flow Near the Swimmer's Body

In a frame moving with the swimmer's body, the velocity field is very small near the no-slip surface. A particle near that surface in the upper-half $x$–$y$ plane has a coordinate vector of the form $\boldsymbol{r} = (A(t) + (R + \delta r)\cos\theta)\hat{\boldsymbol{x}} + (R + \delta r)\sin\theta\,\hat{\boldsymbol{y}}$, where $\delta r$ is small and $0 \le \theta \le \pi$. The 'leading edge' has $\theta = 0$, and the 'trailing edge' has $\theta = \pi$. We Taylor expand for small $\delta r$ and find the tangential velocity

$$u_\theta(\delta r, \theta, t) = \tfrac{3}{2}\frac{\delta r}{R}\sin\theta\left\{(U + \dot{A}) - \tfrac{3}{2}\frac{r\,(R^2 - \alpha^2)^2(U + \dot{a})}{(R^2 + \alpha^2 - 2R\alpha\cos\theta)^{5/2}}\right\} + O((\delta r)^2) \tag{4.1}$$

where $\alpha(t) = a(t) - A(t)$. The term proportional to $U + \dot{A}$ is the same as for a no-slip sphere in a flow with that speed. Using the force balance condition (3.3) to eliminate $\dot{a}$ in (4.1), we find after some work

$$u_\theta(\delta r, \theta, t) = \tfrac{3}{2}(U + \dot{A})\frac{\delta r}{R}\sin\theta\left\{1 + W(\alpha, \theta)\right\}. \tag{4.2}$$

where we dropped terms of order $(\delta r)^2$ and defined

$$W(\alpha, \theta) \coloneqq \frac{3R(R + \alpha)^2\alpha^3}{(R + 2\alpha)(R^2 + \alpha^2 - 2R\alpha\cos\theta)^{5/2}}\,.$$

At leading order, the corresponding radial velocity component is second-order in $\delta r$:

$$u_r(\delta r, \theta, t) \approx -\tfrac{3}{2}\,(U + \dot{A})\,\frac{(\delta r)^2}{R^2}\,\cos\theta\left\{1 + W(\alpha, \theta) + \tfrac{1}{2}\tan\theta\,\partial_\theta W(\alpha, \theta)\right\}. \tag{4.3}$$

Given the velocity components (4.2) and (4.3), is it possible for the flow near the boundary to exhibit a 'bubble' or recirculation region, that is, a separating streamline (in a frame oscillating with the body) other than at $\theta = 0$ or $\pi$? No, since this would require the two terms in the braces in (4.2) to cancel for some $\theta = \theta_{\text{sep}}$, but $W(\alpha, \theta) > 0$ since $\alpha = a - A > R > 0$ to avoid collision between the flagellar Stokeslet and body.

Hence, there is no such 'bubble.' It is notable that the nonexistence of the recirculation region is tied to the force-free condition. The lack of a recirculation region means that a particle initially very close to the $x$ axis (small $y_0$) in the swimmer's path will crawl along the entire length of the swimmer's body.

### 4.1.2 Two-Time Expansion

The polar coordinates of a fluid particle near the swimmer's body satisfy

$$\dot{\delta r} = u_r(\delta r, \theta, t), \qquad \dot{\theta} = u_\theta(\delta r, \theta, t)/R, \tag{4.4}$$

where $u_\theta$ is given by (4.2) and $u_r$ by (4.3). Because both $u_r$ and $u_\theta$ vanish at $\delta r = 0$, a particle near the boundary moves very little at each period $\tau$ with respect to the swimmer's body. This slow motion is captured by a slow time $T$ and the expansions

$$\partial_t \to \partial_t + \varepsilon\, \partial_T, \quad \theta = \theta_0 + \varepsilon\, \theta_1 + \ldots, \quad \delta r = \varepsilon\, (\delta r_1 + \varepsilon\, \delta r_2 + \ldots), \tag{4.5}$$

where $\varepsilon$ is a small parameter proportional to how close the particle is to the body. All the quantities now a priori depend on the two times $t$ and $T$. We now insert the expansions (4.5) into (4.4), use the leading-order dependence of $u_r$ and $u_\theta$ with $\delta r$, and equate powers of $\varepsilon$. At leading order in $\varepsilon$ this gives

$$\partial_t \delta r_1 = 0, \qquad \partial_t \theta_0 = 0,$$

so that $\delta r_1(t, T) = \delta r_1(T)$ and $\theta_0(t, T) = \theta_0(T)$. At the next order, we obtain

$$\partial_T \delta r_1 + \partial_t \delta r_2 = u_r(\delta r_1, \theta_0, t), \qquad \partial_T \theta_0 + \partial_t \theta_1 = u_\theta(\delta r_1, \theta_0, t)/R. \tag{4.6}$$

We average (4.6) over one period in $t$ and impose periodicity of $\delta r_2$ and $\theta_1$, so that $\langle \partial_t \delta r_2 \rangle = \langle \partial_t \theta_1 \rangle = 0$:

$$\partial_T \delta r_1(T) = \langle u_r(\delta r_1(T), \theta_0(T), \cdot) \rangle, \qquad \partial_T \theta_0(T) = \langle u_\theta(\delta r_1(T), \theta_0(T), \cdot) \rangle / R. \tag{4.7}$$

The '$\cdot$' argument indicates that we are averaging only with respect to the last slot, holding $\delta r$ and $\theta$ fixed (see (4.9) below). These are 'slow' equations that capture a particle's drift near the boundary, using a period-averaged velocity. To simplify the notation, we now drop the subscripts and use $t$ for $T$ in (4.7):

$$\dot{\delta r} = \langle u_r(\delta r, \theta, \cdot)\rangle, \qquad \dot{\theta} = \langle u_\theta(\delta r, \theta, \cdot)\rangle / R, \tag{4.8}$$

with

$$\langle u_r(\delta r, \theta, \cdot)\rangle = \frac{1}{\tau}\int_0^\tau u_r(\delta r, \theta, s)\,\mathrm{d}s, \qquad \langle u_\theta(\delta r, \theta, \cdot)\rangle = \frac{1}{\tau}\int_0^\tau u_\theta(\delta r, \theta, s)\,\mathrm{d}s. \tag{4.9}$$

The particle displacement equations (4.8) are time-averaged in the sense that they now only depend on $t$ through the change in $\delta r(t)$ and $\theta(t)$.

Let's evaluate $\langle u_\theta\rangle$. From (4.2), we have

$$\langle u_\theta(\delta r, \theta, \cdot)\rangle = \tfrac{3}{2}\frac{U}{R}\,\delta r\,\sin\theta\,\{1 + \mathcal{W}(\theta)\}\,, \tag{4.10}$$

where

$$\mathcal{W}(\theta) := \frac{1}{\tau}\int_0^\tau (1 + \dot{A}(s)/U)\,W(\alpha(s), \theta)\,\mathrm{d}s. \tag{4.11}$$

The integral (4.11) is straightforward to evaluate numerically. In Fig. 16 we compare the averaged velocity (4.10) (solid line) to an isolated no-slip sphere ($\mathcal{W} \equiv 0$, dashed line) for our reference parameter values. The averaged velocity is much larger on the front side of the swimmer (right) due to the effect of the flagellar Stokeslet. As we shall see below, this implies, paradoxically, that fluid particles are displaced *less* in the fixed lab frame, since their residence time in the boundary region is shorter than for an isolated no-slip sphere (see Section 4.1.4). Put another way, the swimmer's body is less 'sticky' than an isolated no-slip sphere. (This difference is partially mitigated by particles coming closer to the swimmer's body than for a no-slip sphere, see (4.12).)

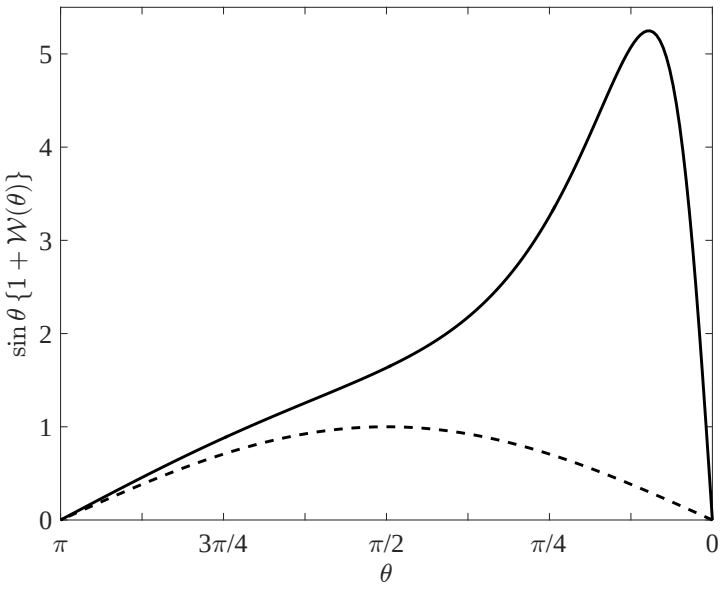


Figure 16: The averaged tangential speed (4.10), after dropping the lead coefficient. The dashed line is for an isolated rigid sphere ($\mathcal{W} \equiv 0$) moving at the same speed. The front of the swimmer is to the right.

### 4.1.3 Averaged Streamline

For an axisymmetric flow, we can define a streamfunction $\psi(r, \theta)$ such that

$$u_r(r,\theta) = \frac{1}{r^2 \sin\theta}\,\frac{\partial\psi}{\partial\theta}\,, \qquad u_\theta(r,\theta) = -\frac{1}{r\sin\theta}\,\frac{\partial\psi}{\partial r}\,.$$

Using this with $r = R + \delta r$ we can find a streamfunction for the averaged flow (4.10):

$$\psi(R+\delta r,\theta) = -\tfrac{3}{4}\,U\,(\delta r)^2 \sin^2\theta\,\{1+\mathcal{W}(\theta)\} + O(\delta r^3),$$

valid in the vicinity of the swimmer's body to leading order in $\delta r$. The streamfunction far from the swimmer is

$$\psi_\infty(r,\theta) = -\tfrac{1}{2}Ur^2\sin^2\theta = -\tfrac{1}{2}Uy^2, \qquad r \gg R,$$

which corresponds to the steady flow from the right. The equation for the 'average streamline' where a particle ends up at $y_1$ after the swimmer has passed is then obtained

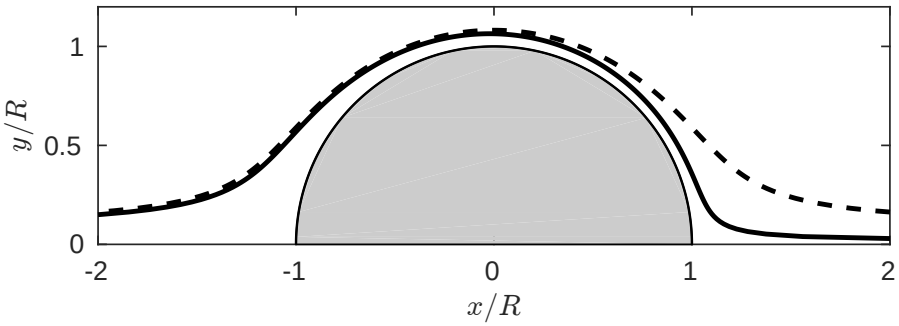


Figure 17: The averaged streamline (4.12) (solid line) is closer to the swimmer's body than for an isolated no-slip sphere ($\mathcal{W} \equiv 0$, dashed) moving at the same speed. The streamline is closest to the body at the front of the swimmer (right side).

by setting $\psi(R+\delta r, \theta) = \psi_\infty(y_1) = -\frac{1}{2}Uy_1^2$, which gives

$$\tfrac{3}{2}\,(\delta r)^2 \sin^2\theta\,\{1+\mathcal{W}(\theta)\} = y_1^2.$$

We then solve this for $\delta r(\theta)$:

$$\delta r(\theta) = \sqrt{\tfrac{2}{3}}\,\frac{y_1}{\sin\theta}\,\{1+\mathcal{W}(\theta)\}^{-1/2}. \tag{4.12}$$

With $\mathcal{W} \equiv 0$ we recover the streamline for an isolated no-slip sphere in a constant flow (see Fig. 17). The term $\mathcal{W}(\theta)$ is positive, so the swimmer's averaged streamline is always closer to the body than for the equivalent isolated no-slip sphere. The difference between a streamline for the isolated no-slip sphere and for the swimmer is most pronounced at $\theta = 0$, as expected since this is the side of the flagellar Stokeslet.

In a steady flow, a particle that starts at $y_0$ far ahead of the swimmer returns to $y_0$ after the swimmer has passed. Because of the time dependence, the streamfunction can change value. We can estimate this change from (4.12):

$$\frac{y_1}{y_0} \approx \frac{[(R+\delta r(\theta))\sin\theta]_{\theta=\pi}}{[(R+\delta r(\theta))\sin\theta]_{\theta=0}} = \sqrt{\frac{1+\mathcal{W}(0)}{1+\mathcal{W}(\pi)}} \approx 5.33. \tag{4.13}$$

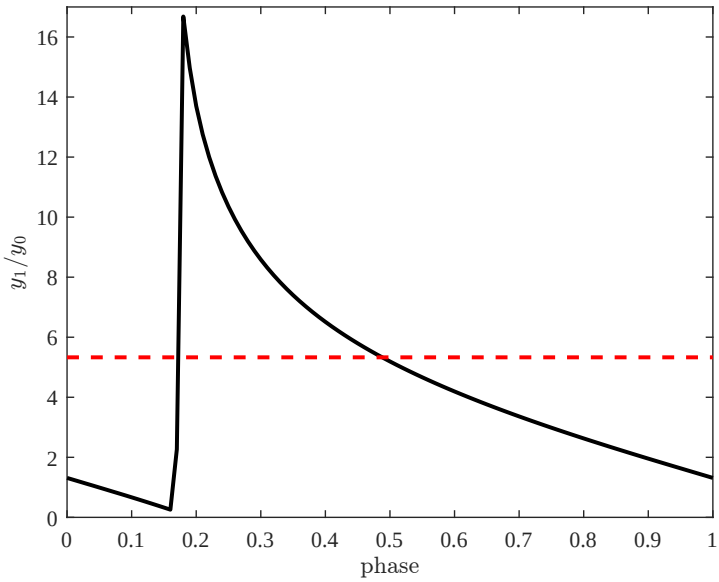


Figure 18: Ratio of final to initial $y$ value, representing the jump in streamline due to the time dependence. The phase is expressed as a fraction of the period $\tau$. The dashed line is the time-averaged expression (4.13).

However, this is at best a rough approximation, since it involves taking $\delta r$ to infinity when it should be small, as well as being based on the time-averaged velocity. Figure 18 shows that the ratio of the final to initial $y$ depends on the phase of the flagellar Stokeslet. The value 5.33 from (4.13) (dashed line) does sit roughly in the middle. The jump is due to streamlines being stretched, folded, and then compressed against the body due to the flagellar Stokeslet (the cause of the folds in Fig. 15). This is followed by varying degrees of shear based on how far different portions of the streamlines end up being from the swimmer's body. This effect can be seen by either varying the initial particle position or by changing the initial flagellar phase while keeping everything else constant.

### 4.1.4 Net Displacement

For large $\lambda$, the largest displacement values will involve particles that travel with the swimmer for a long distance, i.e., particles that stay near the swimmer's body. The displacement in the $y$ direction is then negligible. The residence time near the swimmer's body is

$$T_{\text{res}} = \int_0^T \mathrm{d}t = R \int_0^\pi \frac{\mathrm{d}\theta}{\langle u_\theta(\delta r(\theta), \theta, \cdot)\rangle}.$$

We insert into this the velocity (4.10) to get

$$T_{\text{res}} = R \int_0^\pi \left( \tfrac{3}{2} \frac{U}{R} \, \delta r(\theta) \sin\theta \, \{1 + \mathcal{W}(\theta)\} \right)^{-1} \mathrm{d}\theta$$

and then use the streamline (4.12) to find the net displacement

$$\Delta_\lambda(y_1) = U T_{\text{res}} = \sqrt{\tfrac{2}{3}} \, \frac{R^2}{y_1} \int_0^\pi \{1 + \mathcal{W}(\theta)\}^{-1/2} \, \mathrm{d}\theta. \tag{4.14}$$

This is independent of $x$ since we assume the swimmer moves a long enough distance so that the particle crawls along the full length of the body.

We can evaluate the integral (4.14) numerically to find

$$\Delta_\lambda(y_1) = C R^2 / y_1, \qquad C \approx 1.72919. \tag{4.15}$$

The corresponding coefficient for an isolated no-slip sphere is $\sqrt{2/3}\,\pi \approx 2.56510$, so the swimmer's net displacement is about 67% of an equivalent sphere. This asymptotic expression is compared to numerical simulations for a particular initial flagellar phase in Fig. 19, showing excellent agreement in the $y_1$ match (which remains practically constant over different swimming phases). The $y_0$ data is more sensitive to the swimming phase due to the interaction that occurs with the flagellar Stokeslet on this side of the swimmer. These results provide an additional dichotomy between a puller and a pusher. A pusher

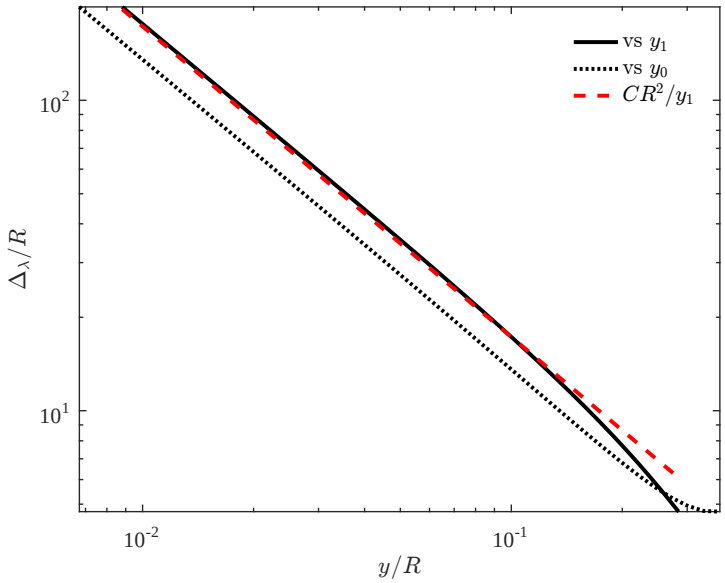


Figure 19: Net particle displacement $\Delta_\lambda$ as a function of the the initial ($y_0$, dotted) and final ($y_1$, solid) distances from the swimming axis. The particle starts far ahead of the swimmer and ends far behind. The dashed line is the asymptotic form (4.15), which agrees with the displacement as a function of the final position $y_1$. It is worth noting that the dotted line is very sensitive to the initial swimming phase, whereas the solid line is not.

can be created by reversing time, and thus also the swimming direction, of our present model. The time-dependence of particle displacements is nearly negligible for a pusher due to the majority of the residence time occuring at the edge of the pusher's body that is furthest from the flagellar Stokeslet. Lastly, note that Fig. 19 predicts very large displacements for small $y$, but in practice these will be capped by the swimming path length $\lambda$.

## 4.2 Far-Field Asymptotics

As we zoom out from our swimmer and look in the far-field, the effect of the singularities in the flow field of Section 3.1.2 cancel out, as we required for our neutrally buoyant swimmer. The net velocity field due to the Stokeslet singularities in (3.6) is then well approximated by a stresslet singularity (with a source term for mass conservation),

$$\boldsymbol{u}_{\text{stress}}(\boldsymbol{r}) = \tfrac{3}{4}U\beta\left(1 - \frac{3x^2}{\|\boldsymbol{r}\|^2}\right)\frac{\boldsymbol{r}}{\|\boldsymbol{r}\|^3} + O(\|\boldsymbol{r}\|^{-3}), \qquad \|\boldsymbol{r}\|/\alpha \gg 1, \tag{4.16}$$

where

$$\beta = \left[\left(\tfrac{5}{2} - \tfrac{3}{2}c_\alpha^2\right)c_\alpha^2 R - \alpha\right](1 + \dot{a}/U)\, r \tag{4.17}$$

is the normalized stresslet strength. Recall that $\alpha = a - A$ is the separation between the flagellar Stokeslet and the center of the swimmer's body, and $c_\alpha = R/\alpha$.

In the lab frame, particles obey $\dot{\boldsymbol{r}} = \boldsymbol{u}_{\text{stress}}(\boldsymbol{r} - Ut\,\hat{\boldsymbol{x}})$. Any time-dependence on the oscillatory positions and strengths of the original Stokeslets is absorbed by the stresslet strength $\beta$ in (4.16). The normalized stresslet strength $\beta$ has a Fourier series derived from (4.17) which we analyze in the following two subsections.

### 4.2.1 Displacement Due to Mean Flow

In the lab frame, the stresslet starts at the origin and proceeds to move in the positive $x$-direction with speed $U$. The mean flow from the swimmer is

$$\boldsymbol{u}(\boldsymbol{r}) = \tfrac{3}{4}U\beta_0\left(1 - \frac{3X^2}{\|\boldsymbol{R}\|^2}\right)\frac{\boldsymbol{R}}{\|\boldsymbol{R}\|^3}, \tag{4.18}$$

where $\beta_0 = \langle\beta\rangle \approx 5.2R^2$, $X = x - Ut$, and

$$\boldsymbol{R} = \boldsymbol{r} - Ut\,\hat{\boldsymbol{x}} = (x - Ut, y, z) \tag{4.19}$$

is the position of the particle relative to the swimmer. The mean flow above remains axially symmetric and thus we set $z = 0$ for convenience. We track a fluid particle that starts at $\boldsymbol{r}_0 = (x_0, y_0, 0)$, and its motion then takes place in the $x$–$y$ plane.

Let $\delta\boldsymbol{r}$ be the particle's displacement from $\boldsymbol{r}_0$. If the particle is moderately far from the swimmer, then $\delta\boldsymbol{r}$ remains small throughout the trajectory, and we can expand to leading order in $\delta\boldsymbol{r}$:

$$u_x\,\hat{\boldsymbol{x}} + u_y\,\hat{\boldsymbol{y}} = \beta_0 \boldsymbol{u}_0(x_0 - Ut, y_0) + O(\|\delta\boldsymbol{r}\|), \tag{4.20}$$

where

$$\boldsymbol{u}_0(x_0, y_0) = \tfrac{3}{4} U \frac{(y_0^2 - 2x_0^2)}{H^5(x_0, y_0)}\,(x_0\,\hat{\boldsymbol{x}} + y_0\,\hat{\boldsymbol{y}}).$$

Here the hypotenuse function is

$$H(x, y) \coloneqq \sqrt{x^2 + y^2}.$$

At this order the particle feels a velocity field that depends solely on its initial position. We can then solve for the particle motion by integrating $\dot{\delta x} = u_x$ and $\dot{\delta y} = u_y$:

$$\begin{aligned}
\delta x(t) &= \tfrac{3}{4}\beta_0 \frac{H^2(\sqrt{2}x_0, y_0)}{H^3(x_0, y_0)} - \tfrac{3}{4}\beta_0 \frac{H^2(\sqrt{2}(x_0 - Ut), y_0)}{H^3(x_0 - Ut, y_0)}, \\
\delta y(t) &= \tfrac{3}{4}\beta_0 \frac{x_0 y_0}{H^3(x_0, y_0)} - \tfrac{3}{4}\beta_0 \frac{(x_0 - Ut) y_0}{H^3(x_0 - Ut, y_0)},
\end{aligned}$$

valid to leading order in $\delta\boldsymbol{r} = \boldsymbol{r} - \boldsymbol{r}_0$. Both coordinates achieve extrema at $Ut = x_0 \pm \frac{1}{\sqrt{2}} y_0$, and $\delta x(t)$ has an additional extremum at $Ut = x_0$. The fact that both coordinates achieve extrema at the same time is reflected by the two 'cusps' visible in Fig. 20b. The coordinates of the two cusps are

$$\delta x_{\text{cusp}} = -\sqrt{\tfrac{2}{3}}\frac{\beta_0}{|y_0|} + \tfrac{3}{4}\beta_0 \frac{H^2(\sqrt{2}x_0, y_0)}{H^3(x_0, y_0)}, \quad \delta y_{\text{cusp}} = \pm\tfrac{1}{2\sqrt{3}}\frac{\beta_0}{|y_0|} + \tfrac{3}{4}\frac{\beta_0\, x_0\, y_0}{H^3(x_0, y_0)}.$$

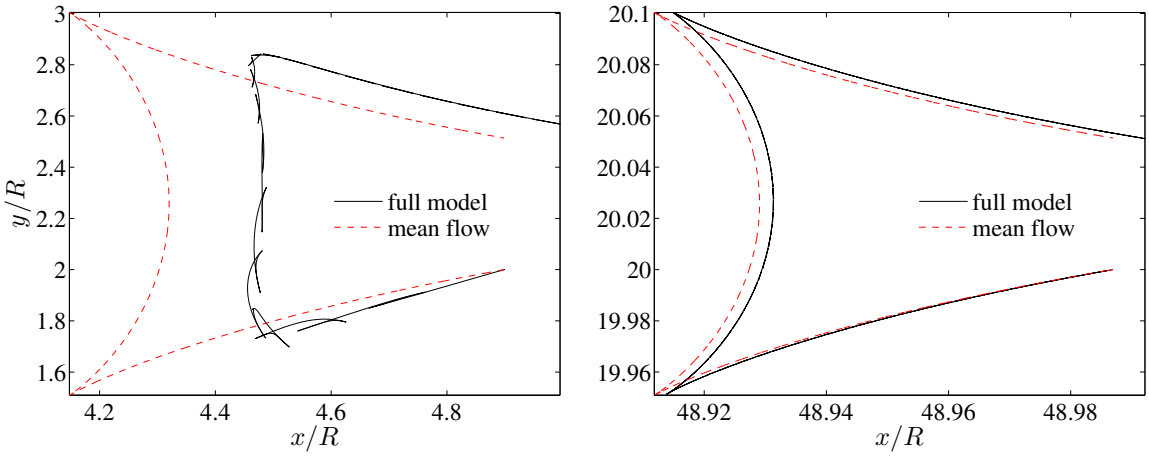


Figure 20: Particle paths (a) near the swimmer and (b) far from the swimmer. Paths caused by the full model from Section 3.1.2, and the far-field approximation of the mean flow from Section 4.2.1. Better agreement is seen for particle paths further from the swimmer.

Examining Fig. 20b and using the location of the cusps, we find that the maximum displacements are bounded as

$$|\delta x(t)| \leq \sqrt{\tfrac{2}{3}}\beta_0/|y_0|, \qquad |\delta y(t)| \leq \tfrac{1}{\sqrt{3}}\beta_0/|y_0|.$$

The total net displacement after a time $t = \lambda/U$ is

$$\overline{\Delta}_\lambda(x_0, y_0) = \sqrt{\delta x^2(\lambda/U) + \delta y^2(\lambda/U)} \leq \beta_0/|y_0|. \tag{4.22}$$

### 4.2.2 Displacement Due to Time-Dependent Flow

In Section 4.2.1 we ignored the time-dependence of $\beta$ and focused on the mean flow. For small particle displacement the expansion (4.20) holds, and the velocity field measured at the particle only depends in the initial position of the particle relative to the swimmer at leading order. This means we can consider the Fourier terms of $\beta$ separately. The

Fourier series expansion of $\beta(t)$ is

$$\beta(t) = \sum_{m=-\infty}^{\infty} \beta_m \mathrm{e}^{\mathrm{i}m\Omega t}.$$

Recall $\beta_0 = \langle\beta\rangle$ is the mean-flow portion described in Section 4.2.1. From (4.20), the contribution to the displacement for a given frequency $m\Omega$ will lead to the integral

$$\delta\boldsymbol{r}_m(t) = \beta_m \int_0^t \boldsymbol{u}_0(x_0 - Us, y_0)\, \mathrm{e}^{\mathrm{i}m\Omega s}\, \mathrm{d}s. \tag{4.23}$$

At high frequencies we expect little contribution from the oscillating part. Indeed, integrating (4.23) by parts gives

$$\int_0^t \boldsymbol{u}_0(x_0 - Us, y_0)\, \mathrm{e}^{\mathrm{i}m\Omega s}\, \mathrm{d}s = \frac{1}{(\mathrm{i}m\Omega)} \left[\boldsymbol{u}_0(x_0 - Us, y_0)\, \mathrm{e}^{\mathrm{i}m\Omega s}\right]_0^t + O(\Omega^{-2})$$

for $m \geq 1$. From (4.23), the ratio of the contribution of the $\beta_m$ term to the averaged flow is roughly

$$\frac{\|\delta\boldsymbol{r}_m(t)\|}{\|\delta\boldsymbol{r}(t)\|} \sim \frac{U}{\Omega}\frac{\beta_m}{\beta_0}\frac{1}{H(x_0 - Ut, y_0)}. \tag{4.24}$$

We see that the ratio of displacements becomes smaller not only as $\Omega$ becomes larger, but also as $H(x_0 - Ut, y_0)$ is made larger. This means that the time dependence has a smaller relative impact on faraway particles than on nearby ones. Hence, in the far-field, where the stresslet approximation is valid, the time dependence of the swimmer can be safely neglected.

# Chapter 5

# Statistics of Particle Displacements

In the following sections we combine our results and determine the importance of time-dependence on mixing and fluid transport. We find the usual ballistic regime for short swimming times and diffusive scalings for long times. Later we see that the largest and rarest displacements are slightly suppressed by the time-dependence. However, these displacements, which arise from close interaction with the swimmer's body, are still larger than that of the common squirmer model.

## 5.1 Effective Diffusivity

At low swimmer volume fractions, the effective diffusivity ($D_{\text{eff}}$) separates into a thermal diffusivity ($D_0$) and an enhanced diffusivity ($D_{\text{h}}$) [31, 51, 61, 78]. The enhanced diffusivity measures how the swimmers diffuse their environment in the absence of thermal noise (which our numerics and asymptotics also neglect), and is related to the second moment of particle displacements via

$$D_{\text{h}} = \frac{nU}{6\lambda} \int_{\mathbb{R}^3} \Delta_\lambda^2(\boldsymbol{r}) \, \mathrm{d}\boldsymbol{r},$$

where $n$ is the number density of the swimmers [46, 61, 76]. We frequently convert between the number density $n$ and the volume fraction $\phi$ of swimmers via $\phi = \frac{4}{3}\pi R^3 n$. Here the integral is over all possible initial positions of a fluid particle with respect to

the swimmer, assuming an infinite domain (and convergence of the integral — see [75]).

The axial symmetry of our swimmer simplifies the enhanced diffusivity computation via

$$D_{\mathrm{h}} = \frac{Un}{6\lambda}\int_{-\infty}^{\infty}\int_{0}^{\infty}\int_{0}^{2\pi}\Delta_\lambda^2(x_0,y_0)\cdot y_0\,\mathrm{d}\theta\,\mathrm{d}y_0\,\mathrm{d}x_0 = \frac{U\pi n}{3\lambda}\int_{-\infty}^{\infty}\int_{0}^{\infty} y_0\Delta_\lambda^2(x_0,y_0)\,\mathrm{d}y_0\,\mathrm{d}x_0$$
$$= \frac{U\pi n}{3\lambda}\int_{-\infty}^{\infty}\int_{-\infty}^{\infty} y_0^2\Delta_\lambda^2(x_0,y_0)\,\mathrm{d}\log y_0\,\mathrm{d}x_0 = \tfrac{1}{3}U\pi n\int_{\mathbb{R}^2} y_0^2\Delta_\lambda^2(x_0,y_0)\,\mathrm{d}\log(y_0/R)\,\mathrm{d}(x_0/\lambda), \tag{5.1}$$

where we use $\log(y_0/R)$ as the integration variable to emphasize small-$y_0$ values, for which the largest displacements occur. A sample integrand for $\lambda \approx 9.8R$ is plotted in Fig. 21. This is closely related to the particle displacement plot Fig. 14, with the addition of the log scaling and the axial symmetry weight $y_0$. The inset in Fig. 21 shows the far-field stresslet form, which is not valid near the swimmer. The largest displacements have been smeared by the time-dependence, and are now asymmetric with respect to the start and end of the swimming path. The largest displacements are associated with particles dragged along the swimmer's no-slip body. However, these are not the dominant contribution to the integral (5.1), because of the $y_0$ weight. The largest displacements are too rare to significantly affect the enhanced diffusivity.

Values of the integral (5.1) are plotted for varying path length in Fig. 22(a), with $t = \lambda/U$. We observe a roughly 'ballistic' scaling ($\lambda^2$) for short swimming times, and a diffusive scaling ($\lambda$) for longer times. This is consistent with the observations in [82, 78, 42, 75]: for short times particles move linearly in time, and so the squared displacement is quadratic with $\lambda$. (In some of these publications the exponent seems smaller than ballistic, which could be because the data is already turning over to the diffusive regime, or because of molecular diffusion.) For longer times particles are left behind

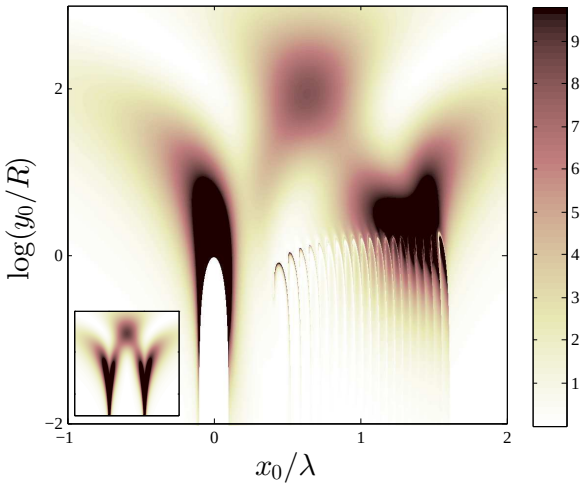


Figure 21: Non-dimensionalized integrand of final expression in (5.1) (inset uses the steady far-field approximation involving $\overline{\Delta}_\lambda$) with $\lambda \approx 9.8R$ and $\beta_0 \approx 5.2R^2$.

and undergo a finite displacement, but the number of particles displaced grows linearly with $\lambda$ [75]. In the far-field the displacements due to a stresslet singularity also leads to linear dependence on $\lambda$, as described by Pushkin and Yeomans [61] and Thiffeault [75].

In Fig. 22(b) we see that the enhanced diffusivity eventually saturates with path length $\lambda$, reaching an asymptotic value of about 70 in dimensionless units. For comparison, if we use only the far-field averaged stresslet value, we find a value of about 60. The increase in the enhanced diffusivity due to time dependence and modeling of the near-field is thus significant but not large. This is consistent with the observation that the integral in (5.1) is dominated by particles that are a few radii away from the swimmer [46], where the stresslet approximation will start to apply, and the heavy suppression of the time dependence at those distances as reflected by (4.24).

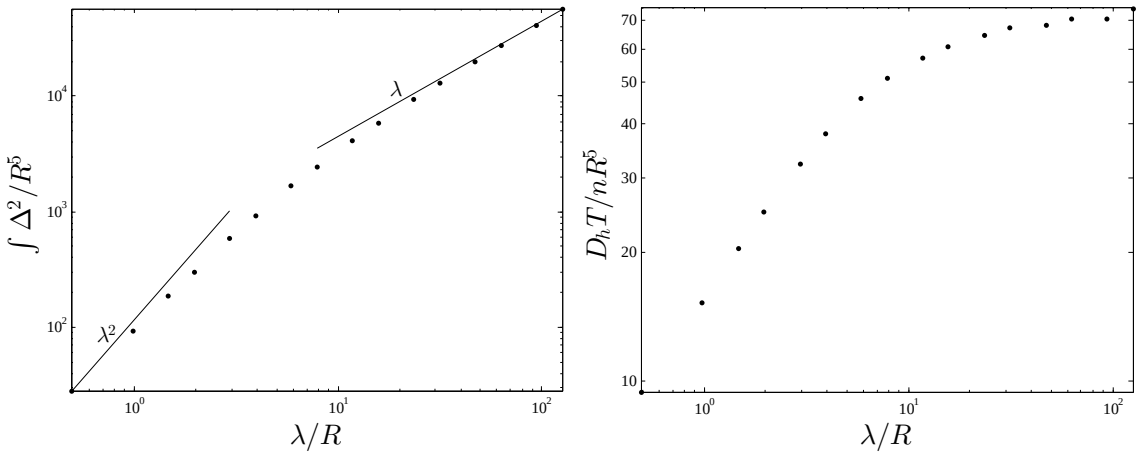


Figure 22: Dimensionless values of the second moment of particle displacements (left) and enhanced diffusivity (right) for varying path lengths of swimmers.

## 5.2 Distribution of Particle Displacements

In Thiffeault [75], the experimental results of Leptos et al. [42] were well-explained by examining the drift function due to a model organism, called a squirmer. Squirmers were introduced by Lighthill [44] and Blake [5]; they consist of a sphere in Stokes flow with an imposed tangential velocity. The force-free condition is imposed to determine the swimming velocity. The far-field form of the velocity field is thus a stresslet, as required for a neutrally-buoyant microswimmer. The imposed velocity at the surface of the squirmer leads to lessened largest particle displacements compared to the model presented here, since particles are not dragged along by the squirmer.

The experimental distributions of Leptos et al. [42] were well-fitted at different volume fractions by steady squirmers with a stresslet strength $\beta = 0.5R^2$. However, it was observed that the fit was worst in the tails of the distribution, corresponding to the largest particle displacements. The hypothesis in modeling a more realistic swimmer

with a no-slip body was that this would lead to fatter tails while leaving the center of the distribution mostly unchanged, since the center depends mostly on far-field (stresslet) effects.

The following result for the probability of a particle being displaced a distance $x$ is borrowed from [75]:

$$p_{X_\lambda}(x) = \frac{1}{2\pi}\int_{-\infty}^{\infty} \exp(-\nu_\lambda \Gamma_\lambda(k))\, \mathrm{e}^{-\mathrm{i}kx}\, \mathrm{d}k, \tag{5.2}$$

where $\nu_\lambda = n\lambda\sigma$, $\sigma = \pi R^2$ is the the cross-section of the swimmer in the direction of motion, and

$$\Gamma_\lambda(k) \coloneqq \frac{1}{\lambda\sigma}\int_V \gamma\left(k\Delta_\lambda(\boldsymbol{\eta})\right)\, \mathrm{d}V_{\boldsymbol{\eta}},$$

with $\gamma(x) \coloneqq 1 - \sin(x)/x$.

We simplify the above equation and combine it with $\nu_\lambda$ for simplicity (as they only show up in tandem in (5.2)):

$$\begin{aligned}
\nu_\lambda\, \Gamma_\lambda(k) = n\int_V \gamma\left(k\Delta_\lambda(\boldsymbol{\eta})\right)\, \mathrm{d}V_{\boldsymbol{\eta}} &= \frac{\phi}{\frac{4}{3}\pi R^3}\int_{\mathbb{R}^3} \gamma\left(k\Delta_\lambda(x,y,z)\right)\, \mathrm{d}x\, \mathrm{d}y\, \mathrm{d}z \\
&= \frac{2\pi\phi}{\frac{4}{3}\pi R^3}\int_{y_0=0}^{y_0=\infty}\int_{x_0=-\infty}^{x_0=\infty} \gamma\left(k\Delta_\lambda(x_0,y_0)\right) y_0\, \mathrm{d}x_0\, \mathrm{d}y_0 \\
&= \frac{3\phi}{2R^3}\int_{\mathbb{R}^2} \gamma\left(k\Delta_\lambda(x_0,y_0)\right) y_0^2\, \mathrm{d}x_0\, \mathrm{d}(\log y_0),
\end{aligned}$$

where we truncate our integration (and also our numerics) such that $\min[\log y_0/R] = -3$ to avoid the singularity. We also note $\Gamma_\lambda(k)$ need only be computed out to $|k| \leq k_{\max}$ such that

$$\nu_\lambda \Gamma_\lambda(k_{\max}) \sim O(1),$$

due to the exponential decay in (5.2) and since $\Gamma_\lambda$ ends up being a convex function of $k$. Lastly, for small arguments, $\gamma(\xi) \sim \frac{1}{6}\xi^2 + O(\xi^4)$.

We use the above small argument approximation in conjunction with a Legendre-Gauss quadrature to handle the $x_0 \to \pm\infty$ and $y_0 \to \infty$ limits. The Legendre transform uses a substitution of $r_0 = r(\theta)/u$ in the following derivation:

$$\begin{aligned}
&\int_0^{2\pi} \int_{r(\theta)}^{\infty} \left[\gamma \left(k\Delta_\lambda(r_0\cos\theta, r_0\sin\theta)\right)\, r_0\sin\theta\right] r_0\,\mathrm{d}r_0\,\mathrm{d}\theta \\
&\qquad\qquad \approx \int_0^{2\pi} \int_{r(\theta)}^{\infty} \left[k^2\Delta_\lambda^2(r_0\cos\theta, r_0\sin\theta)\, r_0\sin\theta\right] r_0\,\mathrm{d}r_0\,\mathrm{d}\theta \\
&\qquad = \int_0^{2\pi} \int_1^0 k^2\Delta_\lambda^2\left(\frac{r(\theta)\cos\theta}{u}, \frac{r(\theta)\sin\theta}{u}\right) \frac{r^2(\theta)\sin(\theta)}{u^2} \cdot \frac{-r(\theta)}{u^2}\,\mathrm{d}u\,\mathrm{d}\theta \\
&\qquad\qquad = \int_0^{2\pi} \int_0^1 k^2\Delta_\lambda^2\left(\frac{r(\theta)\cos\theta}{u}, \frac{r(\theta)\sin\theta}{u}\right) \frac{r^3(\theta)\sin(\theta)}{u^4}\,\mathrm{d}u\,\mathrm{d}\theta,
\end{aligned}$$

where our lower, finite bound for $r_0$ depended on $\theta$ because our high-resolution data 21 spans a rectangular region: $(x_0, y_0) \in [-4\lambda \le x_0 \le 5\lambda] \times [\mathrm{e}^{-3R} \le y_0 \le \mathrm{e}^{7\lambda/100}]$. There is no issue for the $u \to 0$ limit in the above integral due to $\Delta_\lambda^2 \sim 1/r_0^4 = u^4/r^4(\theta)$ for large $r_0$, which is why we used the above Legendre transformation.

We can now compare our dumbbell model to the squirmer from [5, 29, 44, 46]. In Fig. 23 we plot the probability distribution functions for a few volume fractions and compare to the steady squirmer with $\beta = \langle\beta\rangle = 5.2R^2$, the mean stresslet strength for our time-dependent swimmer. As expected, the tails of the distribution are somewhat fatter in our time-dependent model with a no-slip sphere. This improves the match to the data of Leptos et al. [42], though we did not directly compare to their data since their value of $\beta$ leads to somewhat unrealistic parameters in our model, such as the flagellum entering the body. This can be explained by the fact that *C. reinhardtii* has two flagella that can move to the sides of the body, whereas our model exploits axial symmetry to maintain its simplicity. Note also that in computing the distributions for the squirmer in Fig. 23 we omitted particles in the 'atmosphere' (trapped recirculation

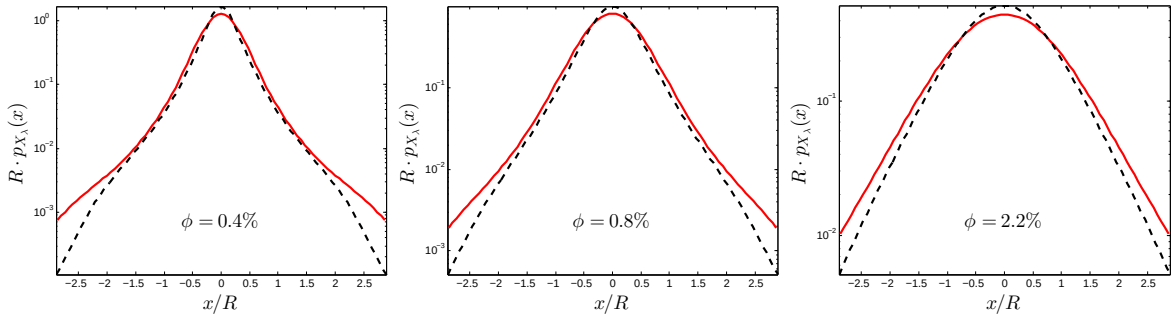


Figure 23: The probability distribution function for varying swimmer volume fractions for steady squirmers (dashed) and the time-dependent model in this paper (solid). The average stresslet strength $\beta$ is the same in both models. The swimmers move a net distance of $\lambda/R \approx 3$, which is comparable to the experiments of Leptos et al. [42].

region) present at $\beta = 5.2R^2$, as described in [46], since such an atmosphere is absent from the time-dependent model. Figure 23 also highlights the convergence to a more Gaussian form as the volume fraction is increased, though the distribution is still far from Gaussian [75].

# Chapter 6

# Optimal Heat Transfer in Microchannels

The field of fluid dynamics involving channels has a broad range of applications including: liquid cooling systems, filtration systems, heating and cooling of buildings, fuel injection systems, and many more. Heat transfer often occurs in these systems along the boundaries of the channels. In this chapter we focus on laminar, incompressible flows in microchannels. Turbulent flows can increase mixing, which assists heat transfer, but causes too much resistance to the flow. First we review velocity fields that arise in curved microchannels and attempt to use COMSOL to run simulations on channels with varying geometries. We run in to some complications and work around them by solving for flows that optimize the heat transfer, invoking a discrete formulation to handle the complex interplay of heat transfer and the steady Navier-Stokes equations.[1]

[1]This research began at an internship in the summer of 2015 at Mitsubishi Electric Research Laboratories in Cambridge, MA. Supervised by Dr. Grover.

## 6.1 Background

The main work done on 3-dimensional channels began with Jones et al. [34]. Their research was based off of the discovery by Dean [12] who found that a pair of counter-rotating vortices form in the cross-section of a curved channel, henceforth known as Dean vortices. Dean found an analytical solution to the flow in a slightly curved channel with circular cross section by perturbing the Poiseuille flow down a straight channel to first order in the curvature. While these vortices result from leading order approximations, they have been found both numerically and experimentally to exist for both moderate values of the curvature and fluid velocity.

Jones et al. [34] proposed and explored the idea of combining two sections of planar curved channels with an angular offset, referred to as a "pitch angle" by the authors. This leads to the crossing of streamlines when traveling from one planar channel to the other, due to the differently oriented Dean vortices in each section. This invention is now referred to as the blinking vortices (blinking refers to the alternating orientations of the vortex pair). Chaotic mixing is found to occur at different levels based on the pitch angle.

### 6.1.1 Planar Channels

The work done by Jones et al. [34] has inspired lots of research to try and reproduce this blinking vortex effect in planar channels (channels whose center of each cross-section lies on the same plane). Planar channels are often easier to manufacture and implement, especially for microscopic channels (referred to as microchannels in the literature). To understand how to achieve chaotic mixing, researchers have looked into the effect of

curvature and flow velocity on the location and strength of the Dean vortex pair. In doing so, a non-dimensional quantity, known as the Dean number, was created:

$$K = Re\sqrt{D_h/R},$$

where $D_h \coloneqq 4A/p$ is the hydraulic diameter (a ratio between the cross-sectional area and the perimeter), $R$ is the radius of curvature, and $Re \coloneqq \rho U D_h/\mu$ is the Reynolds number which incorporates the velocity,.

When the Dean number is increased, the location of the vortex pair begins to drift towards the outer bend. To take advantage of this, research on the so called wavy channels was explored, [1, 33, 54, 73, 84], to name some of the more recent publications. Some enhanced mixing was found for moderate Dean numbers. The slightly off-center Dean vortices would cross with the streamlines of another set of vortices when switching from one signed curvature to the next.

To achieve chaotic mixing, larger Dean numbers are needed. By increasing the Dean number even more, the vortex pair becomes unstable and begins moving around within one bend of the wavy microchannel (constant signed curvature). This instability combined with alternating signed curvature leads to chaotic mixing. Even larger Dean numbers will create a second set of vortices which will enhance mixing even further. We interchange the terms “heat transfer” and “mixing” often because the fluid is usually hotter or colder than the channel’s surroundings and thus mixing of the fluid yields more heat transfer at the wall.

### 6.1.2 Mixing Efficiency

We can easily enhance mixing by putting more energy into the system, but the goal is to optimize the mixing, limited by an energy or enstrophy constraint (where enstrophy measures gradients of the flow). Wavy channels certainly enhance mixing, but at a cost. The standard cost analyzed is the pressure drop along the channel caused by viscous friction. The no-slip condition on the surfaces of the channel as well as the bends take away from the inertia of the flow and thus require more pressure at the input to achieve the same flow rate.

To quantify mixing, papers such as Zheng et al. [84] and Sui et al. [73] look at the the averaged unit-based Nusselt number:

$$\overline{Nu} \coloneqq \frac{1}{\tau_2 - \tau_1} \int_{\tau_1}^{\tau_2} \frac{h_{\text{unit}}(\tau) D_h}{k},$$

where $h_{\text{unit}}$ is the unit-averaged heat transfer coefficient (which depends on the boundary conditions) and $k$ is the thermal conductivity of the walls. They also look at the time-averaged unit-based Fanning friction factor (pressure drop, essentially):

$$\overline{f}_{\text{unit}} \coloneqq \frac{1}{\tau_2 - \tau_1} \int_{\tau_1}^{\tau_2} \frac{2}{\rho u_m^2} \frac{D_h}{4} \frac{\Delta p_{\text{unit}}(\tau)}{s_0},$$

where $u_m$ is the mean flow velocity magnitude, $\Delta p_{\text{unit}}$ is the pressure drop across the unit, and $s_0$ is the channel axial path length in one unit. They compare each of these values to that of a straight channel, yielding the ratios $e_{Nu} = \overline{Nu}_{\text{unit}}/Nu_{\text{st}}$ and $e_f = \overline{f}_{\text{unit}}/f_{\text{st}}$. Then $e_{Nu}/e_f$ becomes a reasonable measurement to optimize the heat transfer of the system.

## 6.2 Optimization Formulation

In our research, coolant is being pushed through a microchannel and we aim to optimize the amount of heat transfer occurring at the walls (outside of the channels is a heat source we are trying to keep cool). Our original plan was to fix a pressure drop across the channel as well as a flow rate and then tweak the geometry and length of the channel so as to maximize the heat transferred along the walls of the channel. The longer or more curved the channel is, the more pressure that is required to obtain the same flow rate. This ended up being a little too ambitious and we propose the following idea instead.

We fix the energy, $\|\boldsymbol{u}\|_{L_2}$, or enstrophy, $\|\nabla \boldsymbol{u}\|_{L_2}$, the flow in the channel is allowed to have (this can be related to the pressure drop and flow rate of the channel). Next, instead of the geometry of the channel determining the fluid flow, we allow any incompressible velocity field and pick the one that locally optimizes a given heat flux norm. The heat flux norm is a way to measure the amount of heat that escapes a given cross-section. Therefore, minimizing the heat flux maximizes the heat transfer at the walls. While the above problem formulation is not entirely realistic, it gives some insight into optimal heat transfer in microchannels.

### 6.2.1 Assumptions and Constraints

We begin by assuming the flow is fully-developed. The term "fully-developed" refers to a flow that does not retain any of the velocity signature at the channel inlet. This normally applies to fluid far enough down the channel. In a channel with periodic geometries, a fully-developed flow is usually periodic in space as well. In our case, this means our flow is independent of time (any time it took to start the fluid moving down

the channel has passed and we have now reached a steady state). We take advantage of this by replacing the axial position with time from here on out; this is allowed since the axial component of the velocity is not allowed to recirculate in our case ($u_3 \geq 0$). Additionally, we assume $u_3 = u_3(x, y)$, i.e. the axial velocity does not change as we move down the channel ($\partial u_3/\partial t = 0$ in this new coordinate system). We prescribe the axial velocity field and, in doing so, fix the flow rate.

We also assume the flow is incompressible and zero on the walls of the channel (no-slip and no-penetration). The heat transfer along the walls is simplified via Dirichlet conditions on the temperature, $\theta|_{\partial\Omega} = 0$. Doing so also makes it reasonable to assume the temperature is never hotter than it is along the walls: $\theta(x, y, t) \leq 0$. We will use the above assumptions in some of the following sections.

Lastly, we need to set the constraint on the cross-sectional velocity field. The most obvious ones are a fixed enstrophy or a fixed energy. Fixing the energy is simpler, but it does not prevent very fine scales from forming in the channel, which seems nonphysical and not ideal for attempting to find a more globally optimal solution. Additionally, there is a more direct relationship between the enstrophy, flow rate, and pressure drop (derived next, culminating in (6.2)), which more accurately resembles our original research idea.

### Relating Pressure Drop and Enstrophy

The following derivation follows similar steps as a comparable result in Jia et al. [32] and is valid for a channel with constant curvature, but can be a decent approximation for channels with more complex geometry. We begin with the steady flow assumption above, we multiply both sides of the steady Navier-Stokes equation by the velocity field:

$$-\boldsymbol{u} \cdot \nabla p = \boldsymbol{u} \cdot \left[\rho(\boldsymbol{u} \cdot \nabla)\boldsymbol{u} - \mu\nabla^2\boldsymbol{u}\right].$$

This expression can be rewritten as

$$-\nabla\cdot(\boldsymbol{u}\rho)=\tfrac{1}{2}\rho\,\nabla\cdot\left[\boldsymbol{u}\|\boldsymbol{u}\|^2\right]-\mu\left\{\nabla\cdot[\boldsymbol{u}\cdot\nabla\boldsymbol{u}]-\|\nabla\boldsymbol{u}\|^2\right\}, \tag{6.1}$$

with use of the divergence-free assumption above and some chain rules, where

$$\|\nabla\boldsymbol{u}\|^2 \coloneqq \sum_i\sum_j(\partial_j u_i)^2.$$

We integrate (6.1) over a section of volume, $V$, bounded by two cross-sections of the channel, $\Omega_1$ and $\Omega_2$, with $\Omega_2$ being further down the channel.

After applying some divergence theorems and using the fact that $\boldsymbol{u}$ is no-slip and no-penetration along the walls of the channel, we obtain

$$\begin{aligned}-\int_{\Omega_1} p\,\boldsymbol{u}\cdot\hat{\boldsymbol{n}}_1\,\mathrm{d}\sigma-\int_{\Omega_2} p\,\boldsymbol{u}\cdot\hat{\boldsymbol{n}}_2\,\mathrm{d}\sigma=\frac{\rho}{2}\left\{\int_{\Omega_1}\|\boldsymbol{u}\|^2\boldsymbol{u}\cdot\hat{\boldsymbol{n}}_1\,\mathrm{d}\sigma+\int_{\Omega_2}\|\boldsymbol{u}\|^2\boldsymbol{u}\cdot\hat{\boldsymbol{n}}_2\,\mathrm{d}\sigma\right\}\\ -\mu\left\{\int_{\Omega_1}[\boldsymbol{u}\cdot(\nabla\boldsymbol{u})]\cdot\hat{\boldsymbol{n}}_1\,\mathrm{d}\sigma+\int_{\Omega_2}[\boldsymbol{u}\cdot(\nabla\boldsymbol{u})]\cdot\hat{\boldsymbol{n}}_2\,\mathrm{d}\sigma\right\}+\mu\int_V\|\nabla\boldsymbol{u}\|^2\,\mathrm{d}\boldsymbol{x},\end{aligned}$$

where $\hat{\boldsymbol{n}}_i$ is the outward pointing normal vector to $\Omega_i$. If we also use the assumption that the axial flow is fully-developed, then $\boldsymbol{u}\cdot\hat{\boldsymbol{n}}$ is independent of the axial position. In this case, the above expression simplifies to

$$\delta p\int_{\Omega_2}\boldsymbol{u}\cdot\hat{\boldsymbol{n}}_2\,\mathrm{d}\sigma=\mu\int_V\|\nabla\boldsymbol{u}\|^2\,\mathrm{d}\boldsymbol{x},$$

where $\delta p \coloneqq p_1-p_2$ is the pressure drop between the two cross-sections, which is a constant since the pressure profiles are identical at each cross-section for a fully-developed flow down a channel with constant curvature. Note that the integral on the left is equal to the flow rate, $F$.

The fully-developed assumption also tells us that the cross-sectional average of $\|\nabla\boldsymbol{u}\|^2$ is independent of the axial position of the channel. Therefore, we can rewrite the previous

equation as

$$\frac{\Delta p}{L} = \frac{\mu}{F} \int_{\Omega} \|\nabla \boldsymbol{u}\|^2 (1 + \kappa x) \, \mathrm{d}x \, \mathrm{d}y, \tag{6.2}$$

where $\Delta p$ is the pressure lost throughout the entire channel (usually defined this way, as in the literature, to be positive), $L$ is the length of the channel, and $\kappa$ is the curvature of the channel. The $(1 + \kappa x)$ is a weighting that accounts for more fluid being near the outer wall of a curved channel, with $x = 0$ being the center of a cross-section and positive values correspond to the outer half of the channel. This "weighting" term arises from the shape of a infinitesimal volume element: the standard $\mathrm{d}x \, \mathrm{d}y$ from the cross-section and a $(1/\kappa + x) \, \mathrm{d}\theta$ from the arc length down the channel. The length of the channel is related to the angular span, $\theta_s$, via $R\theta_s = L$, where $R = 1/\kappa$ is the radius of curvature. Thus the angular integral adds in a $\kappa L$.

### 6.2.2 Heat Flux Norms

Throughout our research we consider two norms to measure the heat flux, $\|u_3\theta\|_{L_1}$ and $\|u_3\theta\|_{L_2}$. These are two different ways to measure the rate at which temperature flows out of a given cross-section of the channel. Minimizing the $L_2$-norm will prevent focused peaks of extreme temperature, while the $L_1$-norm will do a better job at reducing the overall flux. Certain applications may benefit more from one norm or the other, so we derive solutions from both. Our results focus more on the $L_1$ norm.

The heat transfer process can be measured by how much the heat flux norm changes as we traverse down the channel. Recall, for simplicity, we replaced the axial coordinate ($z$) with time. Thus one way to reduce the amount of coolant that escapes a channel is to make $\frac{d}{dt}\|u_3\theta\|_{L_n}^n$ as negative as possible at each cross-section. This method of local

optimization may not recover the globally optimal solution, but it is a good starting point.

Using some of the assumptions in the previous section ($u_3 = u_3(x, y) \geq 0$ and $\theta = \theta(x, y, t) \leq 0$), we obtain the following:

$$\frac{d}{dt}\|u_3\theta\|_{L_1} \coloneqq \frac{d}{dt}\int_\Omega |u_3\theta| \, \mathrm{d}\boldsymbol{x} = -\int_\Omega u_3 \frac{\partial\theta}{\partial t} \, \mathrm{d}\boldsymbol{x} \tag{6.3}$$

and

$$\frac{d}{dt}\|u_3\theta\|_{L_2}^2 \coloneqq \frac{d}{dt}\int_\Omega (u_3\theta)^2 \, \mathrm{d}\boldsymbol{x} = 2\int_\Omega u_3^2 \, \theta \, \frac{\partial\theta}{\partial t} \, \mathrm{d}\boldsymbol{x}, \tag{6.4}$$

where $\Omega$ represents the channel's cross-section. Next, we combine these expressions with the Advection-Diffusion Equation.

### 6.2.3 Optimal Flow Derivation

With our conversion from axial position to time, the usual three-dimensional Advection-Diffusion Equation (ADE) can be approximated by the two-dimensional version:

$$\theta_t + \boldsymbol{u}^* \cdot \nabla\theta = \kappa\Delta\theta,$$

where $\boldsymbol{u}^* \coloneqq (u_1, u_2)$ is the cross-sectional velocity. Using this in conjunction with (6.3) yields

$$\frac{d}{dt}\|u_3\theta\|_{L_1} = -\kappa\int_\Omega u_3\Delta\theta \, \mathrm{d}\boldsymbol{x} + \int_\Omega u_3 \, \boldsymbol{u}^* \cdot \nabla\theta \, \mathrm{d}\boldsymbol{x}. \tag{6.5}$$

We now need to minimize this result, in order to decrease $\|u_3\theta\|_{L_1}$ as much as possible in time. This requires variational calculus.

**Variational Calculus**

We assume a fixed enstrophy constraint which we write as

$$\|\nabla \boldsymbol{u}\|_{L_2}^2 \coloneqq \|\nabla u_1\|_{L_2}^2 + \|\nabla u_2\|_{L_2}^2 + \|\nabla u_3\|_{L_2}^2 = \rho^2,$$

and define the following functional which imposes this constraint using a Lagrange multiplier $\lambda$:

$$J[\boldsymbol{u}^*] = -\kappa \int_\Omega u_3 \Delta\theta \,\mathrm{d}\boldsymbol{x} + \int_\Omega u_3 \,\boldsymbol{u}^* \cdot \nabla\theta \,\mathrm{d}\boldsymbol{x} + \lambda \left\{ \int_\Omega \nabla \boldsymbol{u}^* : \nabla \boldsymbol{u}^* \,\mathrm{d}\boldsymbol{x} - \left(\rho^2 - \|\nabla u_3\|_{L_2}^2\right) \right\},$$

where $A : B \coloneqq A_{ij} B_{ij}$, using the conventional Einstein summation notation. Then the first variational derivative is

$$\left.\frac{\partial J[\boldsymbol{u}^* + \varepsilon \boldsymbol{w}^*]}{\partial \varepsilon}\right|_{\varepsilon=0} = \int_\Omega u_3 \,\boldsymbol{w}^* \cdot \nabla\theta \,\mathrm{d}\boldsymbol{x} - 2\lambda \int_\Omega \Delta \boldsymbol{u}^* \cdot \boldsymbol{w}^* \,\mathrm{d}\boldsymbol{x},$$

after doing some integration-by-parts and extending the no-slip assumption of $\boldsymbol{u}^*$ to $\boldsymbol{w}^*$ as well.

We also impose the incompressibility on $\boldsymbol{w}^*$ by use of the Leray projection ([20]):

$$\left.\frac{\partial J[\boldsymbol{u}^* + \varepsilon \boldsymbol{w}^*]}{\partial \varepsilon}\right|_{\varepsilon=0} = \int_\Omega P(u_3 \nabla\theta) \cdot \boldsymbol{w}^* \,\mathrm{d}\boldsymbol{x} - 2\lambda \int_\Omega \Delta \boldsymbol{u}^* \cdot \boldsymbol{w}^* \,\mathrm{d}\boldsymbol{x},$$

where

$$P(\boldsymbol{v}) \coloneqq \boldsymbol{v} - \nabla \Delta^{-1} (\nabla \cdot \boldsymbol{v}).$$

Therefore, optimality is satisfied when $\boldsymbol{u}^* = \Delta^{-1} P(u_3 \nabla\theta)/(2\lambda)$. Our enstrophy constraint can be written as

$$\|\nabla \boldsymbol{u}^*\|_{L_2}^2 = \rho^2 - \|\nabla u_3\|_{L_2}^2,$$

and thus

$$4\lambda^2 = \frac{\|\nabla \Delta^{-1} P(u_3 \nabla\theta)\|_{L_2}^2}{\|\nabla \boldsymbol{u}^*\|_{L_2}^2} = \frac{\|\nabla \Delta^{-1} P(u_3 \nabla\theta)\|_{L_2}^2}{\rho^2 - \|\nabla u_3\|_{L_2}^2}.$$

The second variation ends up being

$$\left.\frac{\partial^2 J[\boldsymbol{u}^* + \varepsilon \boldsymbol{w}^*]}{\partial \varepsilon^2}\right|_{\varepsilon=0} = \lambda \int_\Omega \|\nabla \boldsymbol{w}^*\|^2 \, \mathrm{d}\boldsymbol{x},$$

and this integral is always positive so we need a positive $\lambda$ in order to minimize $\frac{d}{dt}\|u_3\theta\|_{L_1}$; i.e.

$$\boldsymbol{u}^* = \sqrt{\rho^2 - \|\nabla u_3\|_{L_2}^2}\,\frac{\Delta^{-1}P(u_3\nabla\theta)}{\|\nabla\Delta^{-1}P(u_3\nabla\theta)\|_{L_2}}. \tag{6.6}$$

Repeating the above steps, but now using (6.4), to get an optimal flow that minimizes $\frac{d}{dt}\|u_3\theta\|_{L_2}^2$ results in

$$\boldsymbol{u}^* = \sqrt{\rho^2 - \|\nabla u_3\|_{L_2}^2}\,\frac{\Delta^{-1}P(u_3^2\theta\nabla\theta)}{\|\nabla\Delta^{-1}P(u_3^2\theta\nabla\theta)\|_{L_2}}.$$

Focusing on the result in (6.6), we need to do the following to compute the optimal flow. First let

$$\hat{\boldsymbol{u}}^* \coloneqq \Delta^{-1}P(u_3\nabla\theta) \qquad \text{and} \qquad C(t) \coloneqq \frac{\sqrt{\rho^2 - \|\nabla u_3\|_{L_2}^2}}{\|\nabla\hat{\boldsymbol{u}}^*\|_{L_2}}, \tag{6.7}$$

for convenience so that $\boldsymbol{u}^* = C(t)\,\hat{\boldsymbol{u}}^*$. Then if we also let $\boldsymbol{v} = u_3\nabla\theta$, $f = \nabla\cdot\boldsymbol{v}$, and $h = \Delta^{-1}f$, we see that

$$\boldsymbol{u}^* = C(t)\,\Delta^{-1}\left[\boldsymbol{v} - \nabla h\right]. \tag{6.8}$$

Both $u_3$ and $\theta_0 = \theta(x, y, 0)$ are prescribed (and future values of $\theta$ are determined by the ADE), so we have full knowledge of $\boldsymbol{v}$ and thus also f. Determining the optimal flow, $\boldsymbol{u}^*$, is therefore a matter of solving three Poisson problems (one for each component of $\boldsymbol{u}^*$ and a third for $h$):

$$\Delta\boldsymbol{u}^* = C(t)\,P(\boldsymbol{v}), \qquad \Delta h = f = \nabla\cdot(u_3\nabla\theta).$$

To solve these we need boundary conditions on $\boldsymbol{u}^*$ and $h$, respectively. The first pair of boundary conditions (one for each component of $\boldsymbol{u}^*$) are easy since the optimal flow is set to be no-slip and no-penetration on the walls, which yields Dirichlet boundary conditions. Determining the boundary conditions of $h$ for the third Poisson problem is a little trickier, this was the main issue we had with running simulations in COMSOL.

**COMSOL Issues**

An expression like (6.8) does not hint at what boundary conditions we should impose on $h$. We tried the following steps in COMSOL: prescribe $u_3$ and $\theta_0$ following the conditions listed in Section 6.2.1, compute $f = \nabla \cdot (u_3 \nabla\theta)$, solve $\Delta h = f$ for $h$ by imposing boundary conditions on $h$, compute $P(\boldsymbol{v}) = \boldsymbol{v} - \nabla h$, solve $\Delta\hat{\boldsymbol{u}}^* = P(\boldsymbol{v})$ for $\hat{\boldsymbol{u}}^*$, calculate $C(t)$ from (6.7), and then compute $\boldsymbol{u}^* = C(t)\,\hat{\boldsymbol{u}}^*$. Solving for $\hat{\boldsymbol{u}}^*$ involves two Poisson problems, but the boundary conditions for both components are simple Dirichlet conditions to impose no-slip and no-penetration. We tried multiple different boundary condition combinations when solving the Poisson problem involving $h$, but no matter what, we ended up breaking incompressibility of $\boldsymbol{u}^*$.

To shed some light on this issue, let's temporarily replace the fixed enstrophy constraint with a fixed energy constraint: $\|\boldsymbol{u}\|_{L_2} = \rho^\dagger$. To derive the optimal flow in this case, we minimize (6.5) using variational calculus. The result ends up being:

$$(\boldsymbol{u}^*)^\dagger = C^\dagger(t)\,(\boldsymbol{v} - \nabla h),$$

where $\boldsymbol{v}$ and $h$ haven't changed, but the dagger versions of the other variables correspond to some minor tweaks from the fixed enstrophy case. Now note that since

$$(\boldsymbol{u}^*)^\dagger|_{\partial\Omega} = 0 \qquad \text{and} \qquad \boldsymbol{v}|_{\partial\Omega} = 0,$$

we obtain

$$\nabla h \cdot \hat{\boldsymbol{n}}|_{\partial\Omega} = 0 \qquad \text{and} \qquad \nabla h \cdot \hat{\boldsymbol{t}}|_{\partial\Omega} = 0.$$

The former case gives Neumann boundary conditions, whereas the latter case translates to $h$ being constant along the boundaries (Dirichlet). This yields an overdetermined Poisson problem.

It is unlikely that the fixed energy case being overdetermined and the fixed enstrophy case having uncertainty in the boundary conditions for $h$ is a mere coincidence. We attempt to resolve this issue by solving a discrete version of this problem in the following section. Our hope is that a discrete basis can shed light on these issues or avoid them entirely.

## 6.3 Discrete Version

Throughout this section, Fourier series represent quantities such as velocity fields or the temperature field. We truncate these series in order to solve the above optimization equations for the various Fourier coefficients. We proceed in chronological order with our two significant methods: an incomplete basis (which we show later to have some unwanted symmetries) chosen to match several conditions of our flow, and a complete basis (which ended up having its own issues). The following discrete derivations use a domain of $(x, y) \in [0, 1] \times [0, 1]$.

### 6.3.1 Symmetric Fourier Basis

Our first attempt naively uses the following partial Fourier series for the $x$- and $y$-components of the optimal cross-sectional flow field, corresponding to $\hat{\boldsymbol{u}}^* = (\hat{u}_1, \hat{u}_2)$

above:

$$\hat{u}_1(x,y,t) = \sum_{k,l=0}^{M} \alpha_{kl}(t)\sin(k\pi x)\sin(l\pi y), \qquad \hat{u}_2(x,y,t) = \sum_{k,l=0}^{M} \beta_{kl}(t)\sin(k\pi x)\sin(l\pi y), \tag{6.9}$$

where $M$ is the number of cross-sectional velocity modes we keep in our truncated series. This series representation automatically satisfies no-slip and no-penetration on $\partial\Omega$, where $\Omega = [0,1]\times[0,1]$. Incompressibility then requires

$$\sum_{k,l=0}^{M} \alpha_{kl}(t)\, k\pi\cos(k\pi x)\sin(l\pi y) - \beta_{kl}(t)\, l\pi\sin(k\pi x)\cos(l\pi y) = 0.$$

We felt that this condition would be too cumbersome to continue through the many optimization steps.

Additionally, we made the following incorrect assumption when choosing the partial basis in (6.9). Take, for example, another Fourier series portion that could have been added to either $\hat{u}_1$ or $\hat{u}_2$ above:

$$\sum_{k,l=0}^{M} c_{kl}(t)\cos(k\pi x)\sin(l\pi y).$$

This clearly is zero along $y = 0$ and $y = 1$, but let's examine $x = 0$ for a moment. If we wanted either component of the velocity to be zero along $x = 0$, we would need

$$\sum_{k,l=0}^{M} c_{kl}(t)\sin(l\pi y) = 0.$$

Our original oversight was assuming this would only be satisfied if all $c_{kl}(t)$ were zero, but the second summation actually saves us here. The standard next step is to integrate both sides against basis functions in order to isolate the Fourier coefficients. Doing so yields

$$\sum_{k=0}^{M} c_{kl}(t) = 0 \qquad \forall\ l,$$

which clearly has several valid solutions. This result was missed at first and we instead thought a more restrictive basis was needed (due to too many conditions needing to be met at once: no-slip, no-penetration, and incompressible).

**New Basis Derivation**

This time we begin with a more general basis formulation for the cross-sectional velocity:

$$\hat{u}_1(x,y,t) = \sum_{k,l=0}^{M} \alpha_{kl}(t) f_k(x) g_l(y), \qquad \hat{u}_2(x,y,t) = \sum_{k,l=0}^{M} \beta_{kl}(t) p_k(x) q_l(y).$$

No-penetration and no-slip conditions yield $f_k(0) = f_k(1) = 0 = q_l(0) = q_l(1)$ and $p_k(0) = p_k(1) = 0 = g_l(0) = g_l(1)$, respectively. In this case, incompressibility yields

$$\frac{-\alpha_{kl}(t)}{\beta_{kl}(t)} \frac{f_k'(x)}{p_k(x)} = \frac{q_l'(y)}{g_l(y)}$$

for all $k, l = 0, 1, ..., M$. Note that the left-hand-side is independent of $y$ and thus both sides are equal to a constant, let this constant be $\gamma_{kl,1}$. Additionally,

$$\frac{-\alpha_{kl}(t)}{\beta_{kl}(t)} = \gamma_{kl,1} \frac{p_k(x)}{f_k'(x)}$$

has its variables separated, so both sides are equal to yet another constant, let this one be denoted $\gamma_{kl,2}$. So far we have the following equations from incompressibility:

$$q_l'(y) = \gamma_{kl,1} g_l(y), \quad \alpha_{kl}(t) = -\gamma_{kl,2} \beta_{kl}(t), \quad f_k'(x) = \gamma_{kl,3} p_k(x),$$

where $\gamma_{kl,3} \coloneqq \gamma_{kl,1}/\gamma_{kl,2}$.

Imposing the boundary conditions $q_l(0) = 0$ and $q_l(1) = 0$ results in

$$q_l(y) = \gamma_{kl,1} \int_0^y g_l(y')\,\mathrm{d}y' \qquad \text{and} \qquad \int_0^1 g_l(y)\,\mathrm{d}y = 0,$$

respectively. Thus in $g$'s Fourier series, the constant value is zero and we can assume we now sum from $l = 1, 2, ..., M$ with

$$g_l(y) = G_l \sin(2l\pi y)$$

chosen to satisfy the boundary conditions $g(0) = 0 = g(1)$, where we set each $g_l$ to be one of the terms of a Fourier series representation (since if each $g_l$ had its own Fourier series, we could just combine them and have a similar result). Combining the previous two equations gives us

$$q_l(y) = \frac{\gamma_{kl,1}}{l\pi} G_l \sin^2(l\pi y),$$

In a similar fashion we obtain

$$p_k(x) = P_k \sin(2k\pi x) \qquad \text{and} \qquad f_k(x) = \frac{\gamma_{kl,3}}{k\pi} P_k \sin^2(k\pi x).$$

After combining the above equations and introducing $\xi_{kl}(t) \coloneqq \beta_{kl}(t)\gamma_{kl,1}P_kG_l$, we end up with

$$\hat{u}_1(x,y,t) = \sum_{k,l=1}^{M} \frac{\xi_{kl}(t)}{k\pi} \sin^2(k\pi x)\sin(2l\pi y), \quad \hat{u}_2(x,y,t) = \sum_{k,l=1}^{M} \frac{-\xi_{kl}(t)}{l\pi} \sin(2k\pi x)\sin^2(l\pi y). \tag{6.10}$$

Before we start with deriving the flow that maximizes heat transfer, we point out something we didn't notice until much later. Note the following symmetries of the basis functions above:

$$\hat{u}_1(1-x,y,t) = \hat{u}_1(x,y,t), \qquad \hat{u}_1(x,1-y,t) = -\hat{u}_1(x,y,t),$$

$$\hat{u}_2(x,1-y,t) = \hat{u}_2(x,y,t), \qquad \hat{u}_2(1-x,y,t) = -\hat{u}_2(x,y,t).$$

These symmetries are not a direct consequence of the no-slip, no-penetration, and incompressibility conditions, they arise from our basis functions not forming a complete

basis. We still present our findings because this symmetry may exist for actual flows in microchannels, similar to the symmetric pair of Dean vortices that exist for moderate Dean numbers.

**Optimal Flow**

Recall the main issue in Section 6.2.3 was determining $h$ in

$$\Delta \hat{\boldsymbol{u}}^* = u_3 \nabla\theta - \nabla h,$$

where $\Delta h = \nabla \cdot (u_3 \nabla\theta)$. Now if we try putting the series representation of $\hat{\boldsymbol{u}}^*$, (6.10), into the above equation we obtain

$$\begin{aligned}
2\pi \sum_{k,l=1}^{M} k\, \xi_{kl}(t) \sin(2l\pi y) = \Delta \hat{u}_1|_{x=0,1} &= -h_x|_{x=0,1} \\
0 = \Delta \hat{u}_2|_{x=0,1} &= -h_y|_{x=0,1} \\
0 = \Delta \hat{u}_1|_{y=0,1} &= -h_x|_{y=0,1} \\
-2\pi \sum_{k,l=1}^{M} l\, \xi_{kl}(t) \sin(2k\pi x) = \Delta \hat{u}_2|_{y=0,1} &= -h_y|_{y=0,1},
\end{aligned}$$

after using the fact that $u_3|_{\partial\Omega} = 0$. The second and third conditions imply $h$ is constant along $\partial\Omega$. The arbitrary constant of Poisson's solution can be chosen so that

$$h|_{\partial\Omega} = 0,$$

for simplicity. This suggests the following Fourier series for $h$:

$$h = \sum_{i,j\in\mathbb{N}} \gamma_{ij}(t) \sin(i\pi x) \sin(j\pi y),$$

where $\mathbb{N} = \{1, 2, 3, ...\}$. We prescribe the following Fourier series for the axial flow and temperature field:

$$u_3 = \sum_{i,j=1}^{N_0} \mu_{ij} \sin(i\pi x) \sin(j\pi y) \quad \text{and} \quad \theta = \sum_{i,j=1}^{N} \nu_{ij}(t) \sin(i\pi x) \sin(j\pi y),$$

respectively, where $N_0$ and $M$ will be varied throughout the numerical results.

We obtain the Fourier coefficients for $\hat{\boldsymbol{u}}^*$ in a similar manner to the COMSOL approach. We prescribe $u_3$ and an initial temperature profile $\theta_0 = \theta(x, y, 0)$, compute $h$ via $\Delta h = \nabla \cdot (u_3 \nabla \theta)$, solve $\Delta \hat{\boldsymbol{u}}^* = P(u_3 \nabla \theta)$, find $C(t)$ which ensures the fixed enstrophy constraint, and lastly obtain $\boldsymbol{u}^* = C(t)\, \hat{\boldsymbol{u}}^*$. Any future temperature profiles are assumed to be known by using the previous temperature profile and advancing the ADE with the derived optimal flow from the previous time step. Determining $\boldsymbol{u}^*$ from $u_3$ and $\theta$ on the discrete side uses the following steps.

The Poisson equation used for determining $h$ first becomes

$$\begin{aligned}
&-\pi^2 \sum_{i,j} \gamma_{ij}(t)[i^2 + j^2] \sin(i\pi x) \sin(j\pi y) \\
&\qquad = \sum_{i,j} \sum_{k,l} \mu_{ij} \nu_{kl}(t) \cdot \frac{\pi^2}{4} \{k \left[\cos((j-l)\pi y) - \cos((j+l)\pi y)\right] \\
&\cdot (i \left[\cos((i+k)\pi x) + \cos((i-k)\pi x)\right] - k \left[\cos((i-k)\pi x) - \cos((i+k)\pi x)\right]) \\
&\qquad + l \left[\cos((i-k)\pi x) - \cos((i+k)\pi x)\right] \\
&\cdot (j \left[\cos((j+l)\pi y) + \cos((j-l)\pi y)\right] - l \left[\cos((j-l)\pi y) - \cos((j+l)\pi y)\right])\} ,
\end{aligned}$$

after plugging in the proper series representations. Integrating against $\sin(m\pi x) \sin(n\pi y)$

isolates the Fourier coefficients for $h$:

$$\begin{aligned}\gamma_{mn}(t) = \frac{-1}{m^2+n^2}\sum_{i,j}\sum_{k,l}\mu_{ij}\nu_{kl}(t)\cdot\{&k\left[F(j-l,n)-F(j+l,n)\right]\\ &\cdot\left(i\left[F(i+k,m)+F(i-k,m)\right]-k\left[F(i-k,m)-F(i+k,m)\right]\right)\\ &+l\left[F(i-k,m)-F(i+k,m)\right]\\ &\cdot\left(j\left[F(j+l,n)+F(j-l,n)\right]-l\left[F(j-l,n)-F(j+l,n)\right]\right)\},\end{aligned} \quad (6.11)$$

where

$$F(i,m) = \int_0^1 \cos(i\pi s)\sin(m\pi s)\,\mathrm{d}s = \frac{2m[(i+m)\bmod 2]}{(m^2-i^2+\delta_{i^2,m^2})\pi},$$

where the Kronecker delta is there to ensure the fraction is zero when $m = \pm i$ (otherwise we get a $0/0$).

The first component of the two-dimensional Poisson equation involving $\hat{\boldsymbol{u}}^*$ can be expressed as

$$\begin{aligned}&-2\pi\sum_{k,l}\xi_{kl}(t)\sin(2l\pi y)\left[\frac{l^2}{k}-\left(\frac{l^2}{k}+k\right)\cos(2k\pi x)\right]\\ &=\frac{\pi}{4}\sum_{i,j}\sum_{k,l}k\,\mu_{ij}\nu_{kl}(t)\cdot[\sin((i+k)\pi x)+\sin((i-k)\pi x)]\cdot[\cos((j-l)\pi y)-\cos((j+l)\pi y)]\\ &\qquad-\pi\sum_{i,j}i\,\gamma_{ij}(t)\cos(i\pi x)\sin(j\pi y).\end{aligned}$$

Using (6.11), integrating against $\cos(2m\pi x)\sin(2n\pi y)$, and simplifying, ultimately grants us the Fourier coefficients for $\hat{\boldsymbol{u}}^*$:

$$\xi_{mn}(t) = \frac{32mn}{m^2+n^2}\sum_{i,j}\sum_{k,l}\frac{\mu_{ij}\nu_{kl}(t)\,ijkl\left[m^2(j^2-l^2)-n^2(i^2-k^2)\right]}{\left[(4n^2-j^2-l^2)^2-4j^2l^2\right]\left[(4m^2-i^2-k^2)^2-4i^2k^2\right]}. \quad (6.12)$$

This was verified to match the results obtained by starting with $\Delta\hat{u}_2 = u_3\theta_x - h_y$, instead of the first component.

Lastly, recall

$$C(t) = \frac{\rho_0}{\|\nabla \hat{\boldsymbol{u}}^*\|_{L_2}} := \frac{\sqrt{\rho^2 - \|\nabla u_3\|_{L_2}^2}}{\sqrt{\|\nabla \hat{u}_1\|_{L_2}^2 + \|\nabla \hat{u}_2\|_{L_2}^2}},$$

where we introduce $\rho_0$ since we are allowed to pick $u_3$ and thus it may be more convenient to impose fixed enstrophy via a two-dimensional constraint, $\rho_0$, in place of the three-dimensional constraint. In the event that we do want to relate $\rho_0$ and $\rho$, we need

$$\|\nabla u_3\|_{L_2}^2 = \int_\Omega \nabla u_3 \cdot \nabla u_3 \, \mathrm{d}\boldsymbol{x} = \frac{\pi^2}{4} \sum_{i,j}^{N_0} (i^2 + j^2) \mu_{ij}^2.$$

After deriving $\|\nabla \hat{u}_1\|_{L_2}^2$ and $\|\nabla \hat{u}_2\|_{L_2}^2$ in a similar fashion, we obtain

$$C(t) = 2\rho_0 \left[ \sum_{i,j=1}^{M} \xi_{ij}(t) \left\{ \left( 2 + \frac{j^2}{i^2} + \frac{i^2}{j^2} \right) \xi_{ij}(t) + \sum_{k=1}^{M} \left[ \frac{2j^2}{ik} \xi_{kj}(t) + \frac{2i^2}{jk} \xi_{ik}(t) \right] \right\} \right]^{-1/2}.$$

**Advection-Diffusion Equation**

Following similar steps as above, but now for the ADE rewritten as

$$\theta_t = -\boldsymbol{u}^* \cdot \nabla \theta + \kappa \Delta \theta, \tag{6.13}$$

yields a discrete version of the ADE:

$$\frac{d\nu_{mn}(t)}{dt} = -4C(t) \left[ \sum_{i,j} \left( \sum_{k,l} \xi_{kl}(t) \, A_{ijkl}^{mn} \right) \nu_{ij}(t) \right] - \kappa \pi^2 (m^2 + n^2) \nu_{mn}(t),$$

where

$$A_{ijkl}^{mn} = \frac{32ijklmn}{\pi^2} \left\{ \frac{m^2 + 3i^2 - 4k^2}{m^2 - i^2} - \frac{n^2 + 3j^2 - 4l^2}{n^2 - j^2} \right\} \times \frac{1}{(n^2 - j^2)^2 + 8l^2(2l^2 - j^2 - n^2)} \frac{1}{(m^2 - i^2)^2 + 8k^2(2k^2 - i^2 - m^2)}$$

is, actually, fairly simplified.

### 6.3.2 Complex Fourier Series

After realizing that the cross-sectional velocity components can be zero on the boundaries while having more than just the sine-sine portion of the standard two-dimensional Fourier series, we attempted a new discrete solution using a full basis. In this section we express quantities such as the axial velocity and temperature in a complex basis:

$$u_3(x,y) = \sum_{k,l=-\infty}^{\infty} \mu_{kl}\, \mathrm{e}^{2\pi \mathrm{i} kx} \mathrm{e}^{2\pi \mathrm{i} ly}, \qquad \theta(x,y,t) = \sum_{k,l=-\infty}^{\infty} \nu_{kl}(t)\, \mathrm{e}^{2\pi \mathrm{i} kx} \mathrm{e}^{2\pi \mathrm{i} ly}. \tag{6.14}$$

The derivation of the optimal flow and the discrete form of the ADE follows in a similar manner as before, which we outline in the following sections.

#### Optimal Flow

Recall the (non-enstrophy-constrained) optimal cross-sectional flow:

$$\hat{\boldsymbol{u}}^* = \Delta^{-1} P(u_3 \nabla\theta) = \Delta^{-1} \left[ u_3 \nabla\theta - \nabla \Delta^{-1} \left( \nabla \cdot [u_3 \nabla\theta] \right) \right]. \tag{6.15}$$

We use a streamfunction to impose incompressibility on $\hat{\boldsymbol{u}}^*$ (and thus also $\boldsymbol{u}^*$), with Fourier series

$$\psi(x,y,t) = \sum_{k,l=-\infty}^{\infty} \xi_{kl}(t)\, \mathrm{e}^{2\pi \mathrm{i} kx} \mathrm{e}^{2\pi \mathrm{i} ly}, \tag{6.16}$$

and if we use the following Fourier series for the cross-sectional velocities:

$$u_1 = \sum_{k,l=-\infty}^{\infty} \alpha_{kl}(t)\, \mathrm{e}^{2\pi \mathrm{i} kx} \mathrm{e}^{2\pi \mathrm{i} ly}, \qquad u_2 = \sum_{k,l=-\infty}^{\infty} \beta_{kl}(t)\, \mathrm{e}^{2\pi \mathrm{i} kx} \mathrm{e}^{2\pi \mathrm{i} ly},$$

then

$$\alpha_{kl}(t) = 2\pi \mathrm{i} l\, \xi_{kl}(t) \quad \text{for} \quad l \neq 0, \qquad \text{and} \qquad \beta_{kl}(t) = -2\pi \mathrm{i} k\, \xi_{kl}(t) \quad \text{for} \quad k \neq 0.$$

The list of Fourier coefficients above that are not yet defined ($\alpha_{k,0}$ and $\beta_{0,l}$) are consistent with the need to prescribe boundary conditions on the Poisson problems for the

components of $\hat{\boldsymbol{u}}^*$. The no-penetration conditions on $u_1$ and $u_2$ end up being

$$\sum_{k=-\infty}^{\infty} \alpha_{kl}(t) = 0, \quad \forall\ l, \qquad \text{and} \qquad \sum_{l=-\infty}^{\infty} \beta_{kl}(t) = 0, \quad \forall\ k,$$

respectively. The no-slip conditions on $u_1$ and $u_2$ are

$$\sum_{l=-\infty}^{\infty} \alpha_{kl}(t) = 0, \quad \forall\ k, \qquad \text{and} \qquad \sum_{k=-\infty}^{\infty} \beta_{kl}(t) = 0, \quad \forall\ l,$$

respectively. The no-slip conditions allow us to determine the unknown Fourier coefficients:

$$\alpha_{k,0}(t) = -\sum_{l\neq 0} \alpha_{kl}(t), \quad \forall\ k, \qquad \text{and} \qquad \beta_{0,l}(t) = -\sum_{k\neq 0} \beta_{kl}(t), \quad \forall\ l. \tag{6.17}$$

We resume the original derivation by inputting (6.14) and (6.16) into (6.15) to obtain:

$$\xi_{mn}(t) = \frac{1}{4\pi^2(m^2+n^2)^2} \sum_{k,l=-\infty}^{\infty} [kn - lm]\, \mu_{kl}\, \nu_{m-k,n-l}(t). \tag{6.18}$$

Note that $\xi_{0,0}(t)$ is not well defined above, this corresponds to the arbitrary streamfunction constant. We recover the Fourier coefficients for $\hat{\boldsymbol{u}}^*$ as detailed above. And lastly we compute $C(t)$ in order to constrain the enstrophy; the derivation of which results in

$$C(t) = \rho_0 \left\{ 4\pi^2 \sum_{kl} (k^2+l^2) \left[ |\alpha_{kl}(t)|^2 + |\beta_{kl}(t)|^2 \right] \right\}^{-1/2},$$

where $|\cdot|$ is the complex modulus.

The complex modulus falls out of the derivation due to the following reasons. We begin with $u_3$ and $\theta$ being real, so their Fourier coefficients satisfy $\mu_{-k,-l} = \overline{\mu_{kl}}$ and similarly for $\nu_{kl}(t)$. Therefore, one can show $\xi_{kl}(t)$ has the same property, and it follows that $\alpha_{kl}(t)$ and $\beta_{kl}(t)$ do as well. Lastly, the expression for $C(t)$ above originally involved an $\alpha_{kl}(t) \cdot \alpha_{-k,-l}(t)$, and similarly for $\beta$. This is a nice verification that shows $C(t)$, and thus also $\boldsymbol{u}^*$, is real.

**Advection-Diffusion Equation**

The derivation of the discrete ADE for our new basis is not nearly as bad as our old incomplete basis with unusual symmetries, and so we choose to omit the details. Plugging in our Fourier series into (6.13) yields an ODE for the Fourier coefficients of the temperature field.

$$\frac{d\nu_{mn}(t)}{dt} = -4\pi^2\kappa(m^2+n^2)\nu_{mn}(t) \\ - 2\pi \mathrm{i} C(t) \sum_{k,l=-\infty}^{\infty} \left[(m-k)\alpha_{kl}(t) + (n-l)\beta_{kl}(t)\right] \nu_{m-k,n-l}(t).$$

### 6.3.3 Discrete Solver and Results

With all of the equations derived for the two discrete versions, the following is an outline of how we solve for the velocity and temperature of the fluid throughout the channel. We begin by choosing an axial velocity, $u_3(x.y)$, an initial temperature profile, $\theta(x,y,t)$ (usually $t=0$), and an enstrophy allowance, $\rho_0$ or $\rho$. Next we compute the Fourier coefficients of these functions via

$$\mu_{kl} = 4\int_\Omega u_3(x,y)\ \sin(k\pi x)\sin(l\pi y)\,\mathrm{d}x\,\mathrm{d}y$$

for the symmetric basis, and

$$\mu_{kl} = \int_\Omega u_3(x,y)\,\mathrm{e}^{-2\pi \mathrm{i} kx}\mathrm{e}^{-2\pi \mathrm{i} ly}\,\mathrm{d}x\,\mathrm{d}y$$

for the complex basis. We do the same for the Fourier coefficients of $\theta$. Then we compute the Fourier coefficients of $\hat{\boldsymbol{u}}^*$ using (6.12) or (6.18) in conjunction with the enstrophy allowance, to compute $C(t)$. This gives us all the tools necessary to advance the discrete ADE, and we do so to obtain new Fourier coefficients for $\theta(x,y,t+\delta t)$. With the new

Fourier coefficients, we can repeat the above steps with $\theta(x, y, t + \delta t)$ in place of the previous $\theta(x, y, t)$. We pre-compute some matrices to represent $A_{ijkl}^{mn}$ as well as some portions of (6.12) and other equations for speed.

**Symmetric Fourier Basis**

We begin by showing sample cross-sections from the same channel (at different axial positions). The temperature field and resultant optimal flow to mix it is plotted in Fig. 24. Note the flow field is symmetric even though the temperature is not. Additionally, the flow seems to waste some of its enstrophy allowance in regions of nearly constant temperature. This is a demonstration of the unnatural symmetries for the first basis we worked with.

In order to present the evolution of the temperature field down the channel in a concise way, we compute the heat flux at each cross-section (this was also the quantity we optimized via reducing it locally in time). The heat flux can be computed using the Fourier coefficients:

$$\|u_3\theta\|_{L_1} = -\int_\Omega \sum_{k,l,m,n} \mu_{kl}\nu_{mn}(t)\sin(k\pi x)\sin(l\pi y)\sin(m\pi x)\sin(n\pi y) = \tfrac{-1}{4}\sum_{k,l}\mu_{kl}\nu_{kl}(t),$$

which saves some computational time. Otherwise we would need to compute $u_3$ and $\theta$ from their respective Fourier coefficients, and then also integrate $|u_3\theta|$ over a cross-section.

In Fig. 25 we show the evolution of the heat flux as we move through the channel with $N = 16$ (the number of temperature modes in each direction). Recall $M$ is the number of cross-sectional velocity modes in each direction and note that larger $M$ does

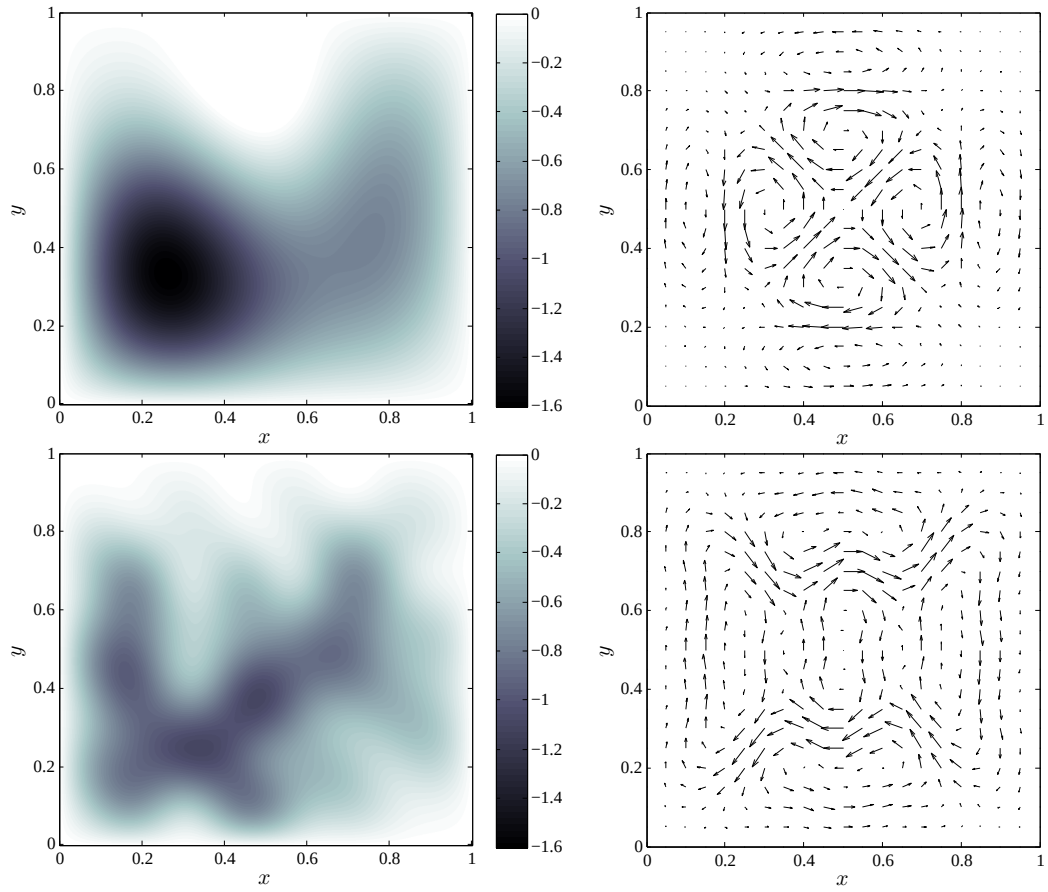


Figure 24: Temperature profile (left column) and resultant optimal flow (right column) of a given cross-section of the channel. Top: Initial cross-section with prescribed temperature. Bottom: Cross-section further down the channel (temperature has evolved according to optimal flow at each cross-section).

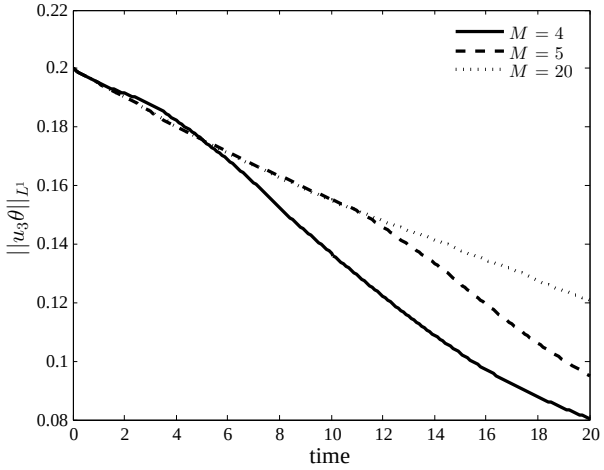


Figure 25: Cross-sectional heat flux as a function of axial position. Each curve represents a different number of Fourier modes ($M$) for the cross-sectional velocity fields.

not necessarily lead to a globally optimal solution. This is due to fewer modes corresponding to less fine scales which is better in our situation. This case might actually be more representative of physical flows, such as the Dean vortices which operate on larger scales.

We verify that our solution converges as we increase the number of terms in each component of the temperature ($N$) and cross-sectional velocity ($M$) series, see Fig. 26. Larger $N$ represents more valid solutions, while larger $M$ just expands the space of available optimal flows. However we still find convergence in $M$ since higher modes correspond to larger enstrophies.

### Complex Fourier Series

After running a few simulations with the new complex basis, things appeared to be working. However, gathering some more results with varied initial temperature profiles, we observed our optimal velocity field did not satisfy our conditions and the temperature

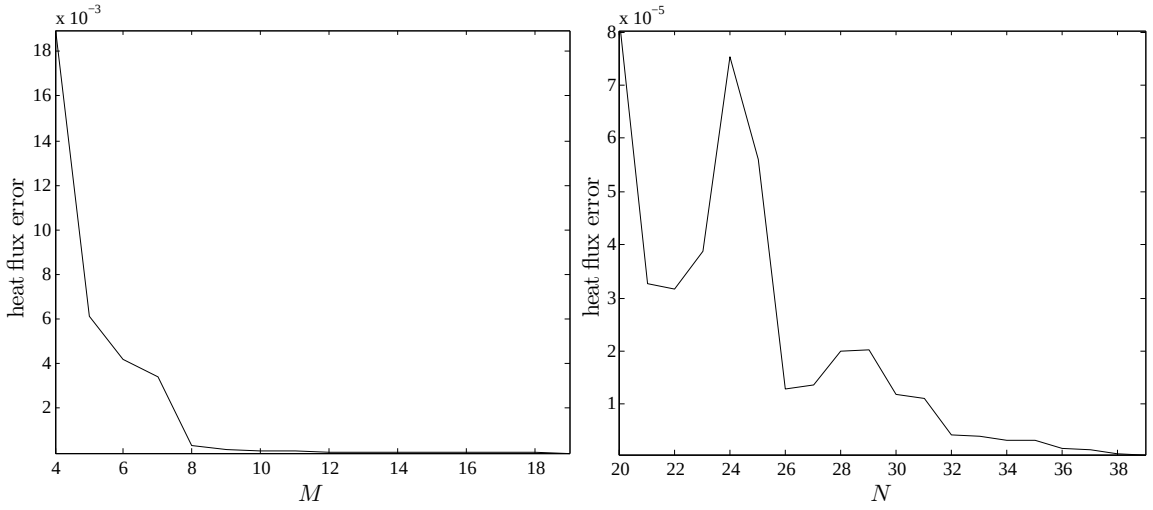


Figure 26: Absolute error in cross-sectional heat flux, averaged over the length of the channel. Left: Discrete series truncated after 16 temperature modes and $M$ cross-sectional velocity modes. Right: 16 cross-sectional velocity modes and $N$ temperature modes. Convergence is slower in $N$.

field did not retain its Dirichlet conditions. We address some of these issues here instead of presenting findings; we use the following chapter to suggest alternative methods that may overcome these problems.

Recall the constraints on the Fourier coefficients of the optimal flow that impose no-slip on $\partial\Omega$, (6.17). Similar equations can be derived to satisfy no-penetration on the walls of the channel. We originally thought no-penetration was automatically satisfied by use of the Leray projection, [20], but simulations suggested otherwise. Imposing no-penetration on the Fourier coefficients caused our system to be overdetermined and our cross-sectional flow was no longer incompressible. Further investigation actually proved that the no-slip condition on its own was enough to break incompressibility. On the bright side, this suggests the original issues we had with COMSOL were more valid than we thought.

Our simulations also revealed that our temperature field did not retain its Dirichlet boundary conditions as we evolved our Advection-Diffusion equation. We ensured this was not just a consequence of an invalid optimal flow as mentioned above by running a simulation without the advective term (pure diffusion). Obviously we needed some conditions on the Fourier coefficients of $\theta$ in order to impose Dirichlet boundary conditions since our new basis is not automatically zero on the boundaries.

Trying to prescribed an initial temperature profile, computing the Fourier coefficients, and then imposing the resultant Dirichlet boundary conditions on the Fourier coefficients, causes an error when reformulating the temperature field. This error is caused by truncating our Fourier series and often turns the temperature field positive in portions of the interior, and our earlier derivations required $\theta \leq 0$. It is unclear how negative of an effect this would have, but we would additionally need to figure out how to alter the discrete form of the ADE to keep $\theta$ fixed at zero along the boundaries without invalidating the ADE. Regardless, the issue with the optimal flow not satisfying incompressibility, no-slip, and no-penetration, is a bigger issue.

# Chapter 7

# Discussion

Here we collect our thoughts, analyze our findings a little more, and propose some possible solutions to our issues as well as ideas for future works.

## 7.1 Dumbbell Model

In our biomixing research we modeled a microswimmer as a no-slip sphere for the swimmer's body and a time-dependent point force (Stokeslet) for its flagella. The model is closer in its dynamical appearance to realistic organisms, such as *C. reinhardtii*. We then compute the time-dependent drift of particles advected by the swimmer. Near the swimmer, we see the stretching and folding action typical of chaotic systems (Fig. 15). We did not investigate this fully, though it would be interesting to examine the small-scale mixing due to microswimmers using the tools from transient chaos in open flows [74, 59].

The drift function, which describes the displacements of fluid particles as the swimmer moves a finite distance, is an interesting object of study in its own right. However, for a time-dependent swimmer we must rely mostly on numerical simulations, as we have done here. The asymptotics of the drift function for the largest displacements (near the swimmer) and the smallest (far away from the swimmer) are also important to understand when examining particle statistics, since these depend on integrals of the drift

function over all space. We found that for the largest displacements the drift function exhibits the $1/y_0$ singularity typical of a no-slip sphere, which corresponds to particles hugging the swimmer's body. However, the drift distance is reduced when compared to an isolated sphere, since the flagellar Stokeslet pushes particles along the body. We were able to obtain a rough estimate for the drift near the body by a suitable averaging over the fast swimming stroke period.

Far from the swimmer, we expect the time dependence to be damped. We showed this explicitly by using the standard method of repeated integration by parts for developing an asymptotic expansion in a fast variable. An important outcome is that the time dependence is damped in two ways: it is damped because it is fast, but also it decreases inversely with distance. Thus, the time dependence is unimportant in many applications that only depend on particle displacements a few radii away from the swimmer.

One application in which the large time-dependent displacements are important is to the statistics of particle displacements. In previous work [75] the experimental distributions of particle displacements of Leptos et al. [42] were well-matched by a steady squirmer model. However, the non-Gaussian tails, which are associated with large displacements, were found to be somewhat below the experiments, indicating that the steady model underestimated the probability of large displacements. We find here that the combination of time dependence and the presence of a no-slip boundary raise these tails while leaving the center of the distribution relatively unchanged. We were not able to match to the experimental distributions themselves: even though our model used parameters close to *C. reinhardtii*, the axial symmetry we used makes matching the mean stresslet strength of that organism very difficult (it would require the flagellar singularity to enter the body, which is unrealistic). Obviously, a better model would be to use

two flagella such as in [21], but breaking axial symmetry makes the necessary volume integrals much harder to evaluate. Alternatively, a ring of Stokeslets could be implemented to preserve axial symmetry. Regardless, there are enough additional parameters that simply matching the experimental distribution with this new model would not be very convincing. (The fit in [75] required the adjustment of only one parameter, the mean stresslet strength.) It may be possible in future experiments to measure the drift function directly, which would help discriminate between models.

Another topic of interest involves recent work done by Kasyap et al. [35] and Patteson et al. [58]. Here they study the effect of tracer/particle size in transport and mixing. This clearly affects the resonance time of particles as particles with more inertia do not change streamlines as easily. Another possible consequence of larger particles is that they would experience gradients in the velocity field differently. Even more complex dynamics may evolve and could give some interesting insight into the "optimal" particle size and how it relates to actual nutrients within the fluid.

## 7.2 Heat Transfer in Microchannels

Recall our two key results: our first basis that was incomplete and gave us some "valid" solutions (in the sense that they were valid for an incomplete basis), and a full basis that had issues satisfying conditions. We have since explored a new avenue and the ongoing work seems promising. The process is as follows: first solve

$$\Delta h = \nabla \cdot \boldsymbol{v} \qquad \text{with} \qquad \nabla h \cdot \hat{\boldsymbol{n}}|_{\partial\Omega} = 0$$

for $h$, where $\boldsymbol{v} = u_3 \nabla\theta$ is given (recall our issue with determining the boundary conditions for $h$). Since $\boldsymbol{v}$ is prescribed to be zero on the boundaries, the above choice of

Neumann conditions for $h$ ensures that

$$\boldsymbol{w} \coloneqq P(\boldsymbol{v}) = \boldsymbol{v} - \nabla h$$

has no-penetration conditions on $\partial\Omega$. Next we need to solve $\Delta\hat{\boldsymbol{u}}^* = \boldsymbol{w}$ for $\hat{\boldsymbol{u}}^*$. Using a streamfunction, $\psi$, we instead want to solve the BiLaplacian equation,

$$\Delta^2\psi = -\nabla \times \boldsymbol{w},$$

for $\psi$. This higher order equation seems to have enough freedoms to satisfy all three of our constraints: incompressibility automatically (since we are using a streamfunction), no-slip becomes $\nabla\psi \cdot \hat{\boldsymbol{n}}|_{\partial\Omega} = 0$, and no-penetration requires that $\psi$ is constant along $\partial\Omega$ (which we can set to zero due to the arbitrary streamfunction constant).

# Bibliography

[1] W. M. Abed, R. D. Whalley, D. J.C. Dennis, and R. J. Poole. Numerical and experimental investigation of heat transfer and fluid flow characteristics in a micro-scale serpentine channel. *Int. J. Heat Mass Transfer*, 88:790–802, 2015. doi: 10.1016/j.ijheatmasstransfer.2015.04.062.

[2] H. Aref. Stirring by chaotic advection. *J. Fluid Mech.*, 143:1–21, 1984.

[3] G. K. Batchelor. *An Introduction to Fluid Dynamics*. Cambridge University Press, Cambridge, U.K., 1967.

[4] A. P. Berke, L. Turner, H. C. Berg, and E. Lauga. Hydrodynamic attraction of swimming microorganisms by surfaces. *Phys. Rev. Lett.*, 101:038102, 2008.

[5] J. R. Blake. A spherical envelope approach to ciliary propulsion. *J. Fluid Mech.*, 46:199–208, 1971.

[6] L. H. Cisneros, J. O. Kessler, S. Ganguly, and R. E. Goldstein. Dynamics of swimming bacteria: transition to directional order at high concentration. *Phys. Rev. E*, 83:061907, 2011. doi: 10.1103/PhysRevE.83.061907.

[7] R. Cortez. The method of regularized stokeslets. *SIAM J. Sci. Comp.*, 23(4): 1204–1225, 2001.

[8] R. Cortez, L. Fauci, and A. Medovikov. The method of regularized stokeslets in three dimensions: Analysis, validation, and application to helical swimming. *Phys. Fluids*, 17:031504, 2005. doi: 10.1063/1.830486.

[9] J. Cosson, P. Huitorel, and C. Gagnon. How spermatozoa come to be confined to surfaces. *Cell Motil. Cytoskel.*, 54(1):56–63, January 2003. doi: 10.1002/cm.10085.

[10] J. O. Dabiri. Role of vertical migration in biogenic ocean mixing. *Geophys. Res. Lett.*, 37:L11602, 2010. doi: 10.1029/2010GL043556.

[11] C. G. Darwin. Note on hydrodynamics. *Proc. Camb. Phil. Soc.*, 49(2):342–354, 1953. doi: 10.1017/S0305004100028449.

[12] W. R. Dean. Note on the motion of fluid in a curved pipe. *Phil. Mag.*, 4(20): 208–223, 1927. doi: 10.1080/14786440708564324.

[13] W. K. Dewar, R. J. Bingham, R. L. Iverson, D. P. Nowacek, L. C. St. Laurent, and P. H. Wiebe. Does the marine biosphere mix the ocean? *J. Mar. Res.*, 64:541–561, 2006.

[14] C. Dombrowski, L. Cisneros, S. Chatkaew, R. E. Goldstein, and J. O. Kessler. Self-concentration and large-scale coherence in bacterial dynamics. *Phys. Rev. Lett.*, 93 (9):098103, August 2004.

[15] K. Drescher, K. C. Leptos, I. Tuval, T. Ishikawa, T. J. Pedley, and R. E. Goldstein. Dancing *volvox*: hydrodynamic bound states of swimming algae. *Phys. Rev. Lett.*, 102:168101, 2009. doi: 10.1103/PhysRevLett.102.168101.

[16] K. D. Drescher, R. E. Goldstein, N. Michel, M. Polin, and I. Tuval. Direct measurement of the flow field around swimming microorganisms. *Phys. Rev. Lett.*, 105: 168101, October 2010.

[17] J. Dunkel, V. B. Putz, I. M. Zaid, and J. M. Yeomans. Swimmer-tracer scattering at low Reynolds number. *Soft Matter*, 6:4268–4276, 2010. doi: 10.1039/c0sm00164c.

[18] I. Eames, D. Gobby, and S. B. Dalziel. Fluid displacement by Stokes flow past a spherical droplet. *J. Fluid Mech.*, 485:67–85, 2003. doi: 10.1017/S0022112003004361.

[19] H. Faxén. Der widerstand gegen die bewegung einer starren kugel in einer zähen flssigkeit, die zwischen zwei parallelen ebenen wänden eingeschlossen ist. *Ann. Phys.*, 373(10):89–119, 1922. doi: 10.1002/andp.19223731003.

[20] C. Foias, O. Manley, R. Rosa, and R. Temam. *Navier–Stokes Equations and Turbulence*. Cambridge University Press, Cambridge, U.K., 2001.

[21] B. M. Friedrich and F. Jülicher. Flagellar synchronization independent of hydrodynamic interactions. *Phys. Rev. Lett.*, 109:138102, September 2012.

[22] Y. O. Fuentes, S. Kim, and D. J. Jeffrey. Mobility functions for two unequal viscous drops in stokes flow. i. axisymmetric motions. *Phys. Fluids*, 31(9):2445–2455, 1988. doi: 10.1063/1.866597.

[23] M. C. Gregg and J. K. Horne. Turbulence, acoustic backscatter, and pelagic nekton in Monterey bay. *J. Phys. Ocean.*, 39:1097–1114, May 2009.

[24] J. S. Guasto, K. A. Johnson, and J. P. Gollub. Oscillatory flows induced by microorganisms swimming in two-dimensions. *Phys. Rev. Lett.*, 105:168102, October 2010.

[25] E. Guazzelli and J. F. Morris. *A physical introduction to suspension dynamics.* Cambridge University Press, Cambridge, UK, 2011.

[26] J. P. Hernandez-Ortiz, C. G. Stoltz, and M. D. Graham. Transport and collective dynamics in suspensions of confined swimming particles. *Phys. Rev. Lett.*, 95: 204501, 2005.

[27] J. P. Hernandez-Ortiz, J. J. de Pablo, and M. D. Graham. Fast computation of many-particle hydrodynamic and electrostatic interactions in a confined geometry. *Phys. Rev. Lett.*, 98:140602, 2007.

[28] M. E. Huntley and M. Zhou. Influence of animals on turbulence in the sea. *Mar. Ecol. Prog. Ser.*, 273:65–79, June 2004.

[29] T. Ishikawa, M. P. Simmonds, and T. J. Pedley. Hydrodynamic interaction of two swimming model micro-organisms. *J. Fluid Mech.*, 568:119–160, 2006.

[30] T. Ishikawa, J. T. Locsei, and T. J. Pedley. Fluid particle diffusion in a semidilute suspension of model micro-organisms. *Phys. Rev. E*, 82:021408, August 2010. doi: 10.1103/PhysRevE.82.021408.

[31] A. Jepson, V. A. Martinez, J. Schwarz-Linek, A. Morozov, and W. C. K. Poon. Enhanced diffusion of nonswimmers in a three-dimensional bath of motile bacteria. *Phys. Rev. E*, 88:041002, 2013. doi: 10.1103/PhysRevE.88.041002.

[32] H. Jia, Z.C. Liu, W. Liu, and A. Nakayama. Convective heat transfer optimization based on minimum entransy dissipation in the circular tube. *Int. J. Heat Mass Transfer*, 73:124–129, 2014. doi: 10.1016/j.ijheatmasstransfer.2014.02.005.

[33] F. Jiang, K. S. Drese, S. Hardt, M. Küpper, and F. Schönfeld. Helical flows and chaotic mixing in curved micro channels. *AIChE J.*, 50(9):2297–2305, 2014. doi: 10.1002/aic.10188.

[34] S. W. Jones, O. M. Thomas, and H. Aref. Chaotic advection by laminar flow in a twisted pipe. *J. Fluid Mech.*, 209:335–357, 1989. doi: 10.1017/S0022112089003137.

[35] T. V. Kasyap, D. L. Koch, and M. Wu. Hydrodynamic tracer diffusion in suspensions of swimming bacteria. *Phys. Fluids*, 26:081901, 2014. doi: dx.doi.org/10.1063/1.4891570.

[36] K. Katija. Biogenic inputs to ocean mixing. *J. Exp. Biol.*, 215:1040–1049, 2012. doi: 10.1242/jeb.059279.

[37] K. Katija and J. O. Dabiri. A viscosity-enhanced mechanism for biogenic ocean mixing. *Nature*, 460:624–627, July 2009. doi: 10.1038/nature08207.

[38] E. Kunze. Fluid mixing by swimming organisms in the low-reynolds-number limit. *J. Mar. Res.*, 69(4-6):591–601, 2011. doi: 10.1357/002224011799849435.

[39] E. Kunze, J. F. Dower, I. Beveridge, R. Dewey, and K. P. Bartlett. Observations of biologically generated turbulence in a coastal inlet. *Science*, 313:1768–1770, September 2006.

[40] H. Kurtuldu, J. S. Guasto, K. A. Johnson, and J. P. Gollub. Enhancement of biomixing by swimming algal cells in two-dimensional films. *Proc. Natl. Acad. Sci. USA*, 108(26):10391–10395, June 2011.

[41] E. Lauga, W. R. DiLuzio, G. M. Whitesides, and H. A. Stone. Swimming in circles: motion of bacteria near solid boundaries. *Biophys. J.*, 90:400–412, January 2006.

[42] K. C. Leptos, J. S. Guasto, J. P. Gollub, A. I. Pesci, and R. E. Goldstein. Dynamics of enhanced tracer diffusion in suspensions of swimming eukaryotic microorganisms. *Phys. Rev. Lett.*, 103:198103, November 2009.

[43] A. M. Leshansky and L. M. Pismen. Do small swimmers mix the ocean? *Phys. Rev. E*, 82:025301, 2010.

[44] M. J. Lighthill. On the squirming motion of nearly spherical deformable bodies through liquids at very small Reynolds numbers. *Comm. Pure Appl. Math.*, 5: 109–118, 1952.

[45] M. J. Lighthill. Drift. *J. Fluid Mech.*, 1:31–54, 1956. Corrigendum **2**, 311–312.

[46] Z. Lin, J.-L. Thiffeault, and S. Childress. Stirring by squirmers. *J. Fluid Mech.*, 669:167–177, February 2011. doi: 10.1017/S002211201000563X.

[47] A. Lorke and W. N. Probst. In situ measurements of turbulence in fish shoals. *Limnol. Oceanogr.*, 55(1):354–364, 2010.

[48] C. Maul and S. Kim. Image of a point force in a spherical container and its connection to the lorentz reflection formula. *J. Eng. Math.*, 30(1):119–130, March 1996. doi: 10.1007/BF00118826.

[49] J. C. Maxwell. On the displacement in a case of fluid motion. *Proc. London Math. Soc.*, s1-3(1):82–87, 1869. doi: 10.1112/plms/s1-3.1.82.

[50] N. H. Mendelson, A. Bourque, K. Wilkening, K. R. Anderson, and J. C. Watkins. Organized cell swimming motions in *Bacillus subtilis* colonies: patterns of short-lived whirls and jets. *J. Bacteriol*, 181(2):600–609, January 1999.

[51] G. L. Miño, T. E. Mallouk, T. Darnige, M. Hoyos, J. Dauchet, J. Dunstan, R. Soto, Y. Wang, A. Rousselet, and E. Clément. Enhanced diffusion due to active swimmers at a solid surface. *Phys. Rev. Lett.*, 106:048102, January 2011. doi: 10.1103/PhysRevLett.106.048102.

[52] G. L. Miño, J. Dunstan, A. Rousselet, E. Clément, and R. Soto. Induced diffusion of tracers in a bacterial suspension: theory and experiments. *J. Fluid Mech.*, 729: 423–444, 2013. doi: 10.1017/jfm.2013.304.

[53] A. Morozov and D. Marenduzzo. Enhanced diffusion of tracer particles in dilute bacterial suspensions. *Soft Matter*, 10:2748–2758, 2014. doi: 10.1039/c3sm52201f.

[54] M. Norouzi and N. Biglari. An analytical solution for dean flow in curved ducts with rectangular cross section. *Phys. Fluids*, 25(5), 2013. doi: 10.1063/1.4803556.

[55] C. Noss and A. Lorke. Direct observation of biomixing by vertically migrating zooplankton. *Limnol. Oceanogr.*, 59(3):724–732, 10.4319/lo.2014.59.3.0724 2014.

[56] C. W. Oseen. *Hydrodynamik*. Mathematik und ihre anwendungen in monographien und lehrbüchern. Akad. Verl.-Ges., Akademische, Leipzig, 1927.

[57] J. M. Ottino. Mixing, chaotic advection, and turbulence. *Annu. Rev. Fluid Mech.*, 22:207–253, 1990.

[58] A. E. Patteson, A. Gopinath, P. K. Purohit, and P. E. Arratia. Particle diffusion in active fluids is non-monotonic in size. *Soft Matter*, 12(8):2365–2372, January 2016. doi: 10.1039/C5SM02800K.

[59] A. Péntek, G. Károlyi, I. Scheuring, T. Tél, Z. Toroczkai, J. Kadtke, and C. Grebogi. Fractality, chaos and reactions in imperfectly mixed open hydrodynamical flows. *Physica A*, 274:120, 1999.

[60] E. M. Purcell. Life at low reynolds number. *Am. J. Phys.*, 45:3–11, January 1977. doi: 10.1119/1.10903. URL `http://www.hunter.cuny.edu/catalyst/repository/files/Life_at_Low_Reynolds_Number.pdf/view?searchterm=`.

[61] D. O. Pushkin and J. M. Yeomans. Fluid mixing by curved trajectories of microswimmers. *Phys. Rev. Lett.*, 111:188101, November 2013. doi: 10.1103/PhysRevLett.111.188101.

[62] D. O. Pushkin and J. M. Yeomans. Stirring by swimmers in confined microenvironments. *J. Stat. Mech.: Theory Exp.*, 2014:P04030, 2014. doi: 0.1088/1742-5468/2014/04/P04030.

[63] D. O. Pushkin, H. Shum, and J. M. Yeomans. Fluid transport by individual microswimmers. *J. Fluid Mech.*, 726:5–25, 2013.

[64] J. Roenby and H. Aref. On the atmosphere of a moving body. *Phys. Fluids*, 22(5):057103, 2010. doi: 10.1063/1.3406960.

[65] A. J. Rothschild. Non-random distribution of bull spermatozoa in a drop of sperm suspension. *Nature*, 198:1221–1222, June 1963. doi: 10.1038/1981221a0.

[66] S. Rousseau, E. Kunze, R. Dewey, K. Bartlett, and J. Dower. On turbulence production by swimming marine organisms in the open ocean and coastal waters. *J. Phys. Ocean.*, 40(9):2107–2121, September 2010. doi: 10.1175/2010JPO4415.1.

[67] I. Rushkin, V. Kantsler, and R. E. Goldstein. Fluid velocity fluctuations in a suspension of swimming protists. *Phys. Rev. Lett.*, 105:188101, 2010. doi: 10.1103/PhysRevLett.105.188101.

[68] D. Saintillan and M. J. Shelley. Orientational order and instabilities in suspensions of self-locomoting rods. *Phys. Rev. Lett.*, 99:058102, 2007.

[69] D. Saintillan and M. J. Shelley. Emergence of coherent structures and large-scale flows in motile suspensions. *J. Roy. Soc. Interface*, 9:571–585, 2012. doi: 10.1098/rsif.2011.0355.

[70] A. Sokolov, I. S. Aranson, J. O. Kessler, and R. E. Goldstein. Concentration dependence of the collective dynamics of swimming bacteria. *Phys. Rev. Lett.*, 98:158102, 2007. doi: 10.1103/PhysRevLett.98.158102.

[71] A. Sokolov, R. E. Goldstein, F. I. Feldchtein, and I. S. Aranson. Enhanced mixing and spatial instability in concentrated bacterial suspensions. *Phys. Rev. E*, 80: 031903, September 2009. doi: 10.1103/PhysRevE.80.031903.

[72] G. Subramanian. Viscosity-enhanced bio-mixing of the oceans. *Current Science*, 98 (8):1103–1108, April 2010.

[73] Y. Sui, C. J. Teo, P. S. Lee, Y. T. Chew, and C. Shu. Fluid flow and heat transfer in

wavy microchannels. *Int. J. Heat Mass Transfer*, 53(13-14):2760–2772, 2010. doi: 10.1016/j.ijheatmasstransfer.2010.02.022.

[74] T. Tél, J. Vollmer, and W. Breymann. Transient chaos: the origin of transport in driven systems. *Europhys. Lett.*, 35:659–664, 1996.

[75] J.-L. Thiffeault. Distribution of particle displacements due to swimming microorganisms. *Phys. Rev. E*, 92:023023, August 2015. doi: 10.1103/PhysRevE.92.023023.

[76] J.-L. Thiffeault and S. Childress. Stirring by swimming bodies. *Phys. Lett. A*, 374: 3487–3490, 2010. doi: 10.1016/j.physleta.2010.06.043.

[77] P. T. Underhill and M. D. Graham. Correlations and fluctuations of stress and velocity in suspensions of swimming microorganisms. *Phys. Fluids*, 23:121902, 2011. doi: 10.1063/1.3670420.

[78] P. T. Underhill, J. P. Hernandez-Ortiz, and M. D. Graham. Diffusion and spatial correlations in suspensions of swimming particles. *Phys. Rev. Lett.*, 100:248101, June 2008.

[79] A. W. Visser. Biomixing of the oceans? *Science*, 316(5826):838–839, 2007. doi: 10.1126/science.1141272.

[80] Stephen Wiggins. *Chaotic Transport in Dynamical Systems*. Springer-Verlag, New York, 1992.

[81] H. Winet, G. S. Bernstein, and J. Head. Observations on the response of human spermatozoa to gravity, boundaries and fluid shear. *J. Reprod. Fert.*, 70:511–523, 1984. doi: 10.1530/jrf.0.0700511.

[82] X.-L. Wu and A. Libchaber. Particle diffusion in a quasi-two-dimensional bacterial bath. *Phys. Rev. Lett.*, 84:3017–3020, 2000. doi: 10.1103/PhysRevLett.84.3017.

[83] I. M. Zaid, J. Dunkel, and J. M. Yeomans. Lévy fluctuations and mixing in dilute suspensions of algae and bacteria. *J. Roy. Soc. Interface*, 8:1314–1331, 2011. doi: 10.1098/rsif.2010.0545.

[84] Z. Zheng, D. F. Fletcher, and B. S. Haynes. Transient laminar heat transfer simulations in periodic zigzag channels. *Int. J. Heat Mass Transfer*, 71:758–768, 2014. doi: 10.1016/j.ijheatmasstransfer.2013.12.056.